Stochastic modeling of snow transport and hydrologic response in alpine terrain

THÈSE N^{O} 7532 (2017)

PRÉSENTÉE LE 20 FÉVRIER 2017

À LA FACULTÉ DE L'ENVIRONNEMENT NATUREL, ARCHITECTURAL ET CONSTRUIT
LABORATOIRE DES SCIENCES CRYOSPHÉRIQUES
PROGRAMME DOCTORAL EN GÉNIE CIVIL ET ENVIRONNEMENT

ÉCOLE POLYTECHNIQUE FÉDÉRALE DE LAUSANNE

POUR L'OBTENTION DU GRADE DE DOCTEUR ÈS SCIENCES

PAR

Francesco COMOLA

acceptée sur proposition du jury:

Prof. A. Rinaldo, président du jury
Prof. M. Lehning, Prof. B. Schaefli, directeurs de thèse
Prof. M. Parlange, rapporteur
Prof. J. Kok, rapporteur
Prof. A. Berne, rapporteur

ÉCOLE POLYTECHNIQUE
FÉDÉRALE DE LAUSANNE

Suisse
2017

Felix qui potuit rerum cognoscere causas.
— Vergilius, Georgica, II, 489

Alla mia famiglia

Acknowledgements

First and foremost, I wish to express my gratitude to my thesis directors, Professors Michael Lehning and Bettina Schaefli. Michi always guided me towards innovative and challenging research perspectives, encouraged to pursue my own scientific interests, and granted unique opportunities to travel abroad and establish collaborations. Bettina provided me with constant support during my studies. Her guidance and advice were an exceptional help in advancing the research and writing this thesis. Their dedication to work and family was a great inspiration and contributed to my personal and academic development.

Besides my advisors, I wish to sincerely thank Prof. Andrea Rinaldo for introducing me to the world of scientific research. The keen passion for science that Andrea passed down to me during my studies at the University of Padova pushed me to pursue a doctoral degree. I will always value his enlightening teachings.

Heartfelt thanks also goes to Prof. Jasper Kok, for hosting me in his research group at UCLA. Jasper sets an example of a well organized and proficient scientist. His kindness and outstanding critical thinking led to a very enjoyable and efficient collaboration.

I would like to acknowledge the rest of my thesis committee, Prof. Marc Parlange and Prof. Alexis Berne. Their insightful comments motivated me to widen my research from various perspectives. I am also grateful to Marc for the profitable interactions at the time he was head of the EFLUM laboratory at EPFL. His exceptional capability of managing and motivating a large research group set for me a great example.

Sincere thanks also goes to all my collaborators, Pierfrancesco da Ronco, Gianluca Botter, Mathias Bavay, Johan Gaume, and Enrico Paterna, whose contributions were fundamental to the scientific publications and to this thesis.

I wish to thank my past and current office mates for making my everyday life special in many ways. Raphaël Hösli, for all the great time spent together in the office, home, by the lake, and in the mountains. Aurélien Gallice, for his kindness and for teaching me how to take care of office plants. Marco Giometto, great colleague, friend, and unmatchable connoisseur of cigars. Ernesto Trujillo, who fueled my interests for cinema, photography, and good wines. Igor Ayrton, for the fun moments shared inside and outside the office. Margaux Couttet, irreplaceable promoter of social life, for bearing with me the last stressful days of my Ph.D.

I am also grateful to all my colleagues and friends in Lausanne. In particular, I wish to thank Raphaël Mutzner, Tristan Brauchli and Flavio Finger, for teaching me the Swiss approach to life and for all the fun we had in the last four years. Thanks Varun Sharma, Benôit Gherardi and Nataliya Kryvych for the stimulating discussions on disparate topics. Special thanks also

goes to Annelen Kahl, our amazing running coach, for her support in the proof-reading of the thesis, Jérôme Dujardin, for raising my sensitivity to environmental issues, and Hendrik Huwald, for his scientific advices, generosity and sense of humor. I am grateful to Marie-Jo Pellaud and Jessica Ritzi, for taking care of the administrative side of my doctoral studies. Many thanks go to Giulia Ruggeri, for the hearty laughs and for courageously bringing me ski touring, Alessandro Cavinato, great friend and flatmate, Lorenzo Gorla and Amin Niayifar, for keeping me trained in table tennis, Paolo Benettin, Luca Carraro, and Damiano Pasetto, for the insightful political discussions and the board game sessions.

My sincere thanks also goes to the fantastic friends and colleagues at UCLA, Raleigh Martin, Francis Turney, and Yue Huang, for the fruitful scientific interactions and leisure activities. They made my days in Los Angeles a terrific experience.

Un grazie di cuore ai miei amici in Italia, e a quelli in giro per il mondo, per farmi sentire come se il tempo non fosse mai passato. Il ricordo di esperienze indimenticabili mi spinge continuamente a ritrovarvi per viverne di nuove.

Desidero ringraziare di cuore i miei genitori e la mia famiglia, inesauribili fonti di affetto e incoraggiamento. Dedico a loro questo importante traguardo, per esprimere la mia gratitudine piú di quanto le parole mi consentano.

最后, 我希望与我亲爱的青侠分享收获博士学位的激动与喜悦! 你对我一点一滴的爱是我获得成功的无尽源泉和不竭动力. 幸你我相知, 盼余生共济. 感谢你, 我的爱人!

Lausanne, 20th February 2017 F. C.

Abstract

The scientific community has developed a keen interest in the processes driving the hydrologic cycle in alpine regions. The concern mainly stems from the vulnerability of snow-covered environments to the warming temperatures, such that entire ecological and social systems are at stake. Snow and ice storages in alpine regions are, in fact, fundamental water resources for large and dry lowland areas of western Americas, central Asia, northern India, and southern Europe. Snowmelt is also the principal control on the hydrologic and thermal regimes of alpine streams, which act as ecological corridors for a wide range of aquatic species. Despite the growing body of literature on the subject, the dynamics of some relevant processes are still unclear. Here, we aim at providing a deeper insight into the preferential deposition of snowfall, the wind-driven erosion and redistribution of snow, the fragmentation of drifting snow crystals, the stream temperature dynamics, and the effects of the solar radiation pattern on the hydrologic response of alpine catchments. We address our scientific questions with theoretical and numerical models that cast the complex transport phenomena in stochastic frameworks.

The first part of this thesis focuses on snow transport. We combine a Lagrangian-stochastic model of particle dynamics, large-eddy simulations, and an immersed boundary method to investigate the processes driving the heterogeneous snow distribution in alpine terrain. Our results suggest that near-surface flow-particle interactions reduce snowfall deposition on the wind- and leeward slopes of the mountains, while a larger amount of snow accumulates on the hilltop and the surrounding flat terrains. Moreover, drifting and blowing snow can significantly change the snow depth distribution by eroding the hilltop and replenishing the leeward side of the ridge. We then propose a snow crystal fragmentation theory, whose assumptions are tested with discrete element simulations, to understand the transition from the size distribution of snowflakes to that of blowing snow particles. Our findings suggest that a range of scale-invariance in the blowing-snow size distribution emerges from the fractal geometry of snow crystals. Moreover, we show that the fundamental laws of energy and momentum conservation allow us to predict the number of particles ejected upon collision of drifting grains with a snow surface, characterized by arbitrary particle size distribution and cohesion.

The second part of the thesis focuses on hydrological processes in alpine catchments. We first derive a theoretical framework, based on a residence time distribution approach that describes the coupled water and energy transport processes at hillslope scale. We then account for the proposed theory in a spatially explicit hydrological model to simulate stream flow and stream temperature dynamics in alpine catchments having arbitrary degrees of geomorphological complexity. Our model results highlight that highly heterogeneous advective and non-advective energy fluxes in the stream network yield water temperatures of remarkable spatial and temporal variability. Finally, we show that the effects of different solar radiation patterns on the snow-dominated hydrologic response are scale-dependent, i.e., significant at small scales where slopes present a predominant orientation, and almost negligible for catchment sizes larger than the aspect correlation scale.

Key words: Snowfall, Fragmentation, Saltation, Stream flow, Stream temperature, Large eddy simulation, Lagrangian stochastic model, Immersed boundary method, Travel time distribution, Temperature-index model

Sommario

I processi fisici alla base del ciclo idrologico in ambienti alpini sono oggetto di attiva ricerca scientifica. Tale interesse scaturisce principalmente dalla vulnerabilitá degli ambienti nivali all'aumento di temperatura, al punto di mettere a rischio interi sistemi sociali ed ecologici. Gli accumuli di ghiaccio e neve in regioni alpine, infatti, costituiscono un'essenziale risorsa d'acqua per vaste regioni aride in America occidentale, Asia centrale, India settentrionale ed Europa meridionale. Lo scioglimento nivale esercita, inoltre, un controllo fondamentale sul ciclo termo-idrologico dei torrenti alpini, con impatti rilevanti per le le dinamiche ecologiche di numerose specie acquatiche. Nonostante la crescente letteratura scientifica sull'argomento, alcuni importanti processi fisici risultano ancora poco chiari. Lo scopo di questa tesi é di fornire una migliore comprensione della deposizione preferenziale di neve, del trasporto e della frammentazione di cristalli di neve ad opera del vento, dei processi termici nei torrenti e degli effetti della radiazione solare sulla risposta idrologica di bacini alpini. A tal scopo, proponiamo e applichiamo modelli stocastici, sia teorici che numerici, in grado di descrivere i complessi fenomeni di trasporto.

La prima parte della tesi tratta del trasporto di neve. Tramite accoppiamento di un modello Lagrangiano stocastico a un modello large-eddy simulation, vengono inizialmente studiati i processi atmosferici responsabili della disomogenea distribuzione di neve in terreni alpini. L'effetto della topografia sul campo di moto circostante é tenuta in considerazione tramite un metodo immersed boundary. I risultati del modello indicano che le interazioni tra il campo di moto turbolento e i fiocchi di neve in vicinanza della superficie provocano una riduzione della deposizione sui versanti di monte e di valle. Un incremento della deposizione é invece osservato sulle cime e sui terreni pianeggianti. L'erosione ad opera del vento é successivamente in grado di trasportare una significativa quantitá di neve dalle cime verso i versanti di valle. Viene in seguito descritto un modello teorico di frammentazione dei cristalli di neve, le cui ipotesi trovano verifica nei risultati di un modello a elementi discreti. La teoria proposta é in grado di spiegare la transizione dalla granulometria tipica dei fiocchi di neve a quella tipica delle particelle di ghiaccio trasportate dal vento. I nostri risultati suggeriscono che l'invarianza di scala osservata nella granulometria delle particelle di neve emerge dalla geometria frattale dei cristalli. Dimostriamo infine come le leggi di conservazione di energia e quantitá di moto ci permettano di simulare con accuratezza le dinamiche superficiali di impatto-espulsione di particelle di neve, caratterizzate da arbitrarie granulometria e coesione.

La seconda parte della tesi tratta dei processi idrologici in bacini alpini. Proponiamo inizialmente un inquadramento teorico, basato sulla distribuzione dei tempi di residenza, per la descrizione simultanea del trasporto di massa e di energia a scala di versante. A partire da tale teoria, deriviamo successivamente un modello idrologico spazialmente esplicito per la modellizzazione della portata e della temperatura dell'acqua in bacini alpini. La formulazione del modello tiene esplicitamente in considerazione la complessitá geomorfologica del bacino. I risultati indicano che l'eterogeneitá dei processi di scambio termico induce una significativa variabilitá spaziale nel regime termico della rete fluviale. Dimostriamo infine che gli effetti idrologici di differenti distribuzioni spaziali di radiazione solare dipendono dalla scala di osservazione. Gli effetti sulla risposta idrologica sono infatti visibili a piccole scale spaziali, in cui i versanti presentano un'esposizione preferenziale, e quasi trascurabili quando la dimensione del bacino é dell'ordine della scala di correlazione spaziale dell'esposizione dei versanti.

Parole chiave: Precipitazione nevosa, Frammentazione di cristalli di neve, Saltazione di sedimenti, Portata dei corsi d'acqua, Temperatura dei corsi d'acqua, Large eddy simulation, Modello Lagrangiano stochastico, Metodo Immersed boundary, Distribuzione dei tempi di residenza, Modello di scioglimento nivale

Contents

Acknowledgements **i**

Abstract (English/Italiano) **iii**

List of figures **xi**

List of tables **xvii**

Introduction **1**

The hydrologic cycle in alpine terrains . . . 1
State of research . . . 2
Preferential deposition . . . 2
Snow fragmentation . . . 2
Drifting and blowing snow . . . 3
Hydrological and thermal response of alpine catchments . . . 3
Objectives and organization of the thesis . . . 4

1 Large eddy simulations of snowfall deposition in mountain terrain **7**

1.1 Abstract . . . 7
1.2 Introduction . . . 8
1.3 Methods . . . 9
1.3.1 Large eddy simulations . . . 9
1.3.2 Immersed boundary method . . . 10
1.3.3 Lagrangian stochastic model . . . 10
1.4 Model validation . . . 12
1.5 Simulation of snowfall deposition . . . 14
1.6 Discussion and conclusions . . . 16
1.7 Acknowledgments . . . 18

2 Fragmentation of wind-blown snow crystals **19**

2.1 abstract . . . 19
2.2 Introduction . . . 19
2.3 Snow crystal fragmentation . . . 20
2.4 Blowing-snow fragmentation . . . 23
2.5 Modeling blowing-snow fragmentation . . . 24

2.6 Model results . . . 25
2.7 Discussion and conclusions . . . 27
2.8 Acknowledgments . . . 28

3 Energy- and momentum-conserving model of splash entrainment in sand and snow saltation 29
3.1 abstract . . . 29
3.2 Introduction . . . 29
3.3 Ejection model . . . 30
3.4 Sand ejection . . . 33
3.5 Snow ejection . . . 35
3.6 Conclusions . . . 37
3.7 Acknowledgements . . . 38

4 Large eddy simulations of drifting and blowing snow in mountain terrain 39
4.1 Abstract . . . 39
4.2 Introduction . . . 40
4.3 Methods . . . 41
  4.3.1 Modeling technique . . . 41
  4.3.2 Parameterization of surface processes . . . 42
4.4 Results . . . 44
4.5 Discussion and conclusions . . . 47
4.6 Acknowledgements . . . 49

5 Thermodynamics in the hydrologic response: Travel time formulation and application to Alpine catchments 51
5.1 abstract . . . 51
5.2 Introduction . . . 52
5.3 Theoretical framework . . . 53
  5.3.1 Mass transport . . . 54
  5.3.2 Energy transport . . . 56
5.4 Implementation for Alpine catchments . . . 59
  5.4.1 Streamflow simulation . . . 60
  5.4.2 Stream temperature simulation . . . 61
5.5 Case study and simulation set-up . . . 64
5.6 Results and discussion . . . 65
  5.6.1 Sensitivity, calibration and validation . . . 65
  5.6.2 Temperature cycles of subsurface flow . . . 68
  5.6.3 Hydrologic and thermal variability in the stream network . . . 69
5.7 Conclusions . . . 69
5.8 Acknowledgments . . . 70

6 Scale-dependent effects of solar radiation patterns on the snow-dominated hydrologic response 71
6.1 abstract 71
6.2 Introduction 71
6.3 Methods 72
  6.3.1 Modeling Approach 72
  6.3.2 Virtual Experiments 73
6.4 Case Study and Simulation Setup 74
6.5 Results and Discussion 74
6.6 Conclusions 78
6.7 Acknowledgements 78

Conclusions and perspectives 79

A Appendix A 83
A.1 introduction 83
A.2 Residence time distribution model 83
A.3 Discrete element model 85
A.4 Datasets of blowing-snow size-distributions 86
A.5 Snowfall and surface particle size-distributions 87

B Appendix B 89
B.1 Introduction 89
B.2 Derivation of the model equations 89
B.3 Model setup for sand and snow 91
B.4 Sensitivity analysis 92
B.5 Monte Carlo simulations 92

C Appendix C 95
C.1 Introduction 95
C.2 Aspect Variograms in Alpine Environments 95
C.3 SWE Variations Induced by Different Solar Radiation Patterns 95

Bibliography 113

Curriculum Vitae 115

List of Figures

1.1 Time-averaged velocity field over the ranges of six hills. The hills are modeled according to the experimental set-up described in Goossens [1996]. 13

1.2 Time-averaged concentration field over the ranges of six hills. The hills are modeled according to the experimental set-up described in Goossens [1996]. 13

1.3 Normalized deposition profile obtained from the simulation (black line) and from the wind tunnel experiments (red line). The normalization is performed as indicated in equation 1.9. The profile is obtained by averaging $\tilde{D}$ in the $y-$direction. 14

1.4 (Left) Time-averaged velocity field around the Gaussian ridge. (Right) Velocity profiles upstream (S1), above (S2), and downstream (S3) of the ridge. 15

1.5 Snapshot of the snowfall simulation at time $t = 25$ s. 16

1.6 Normalized deposition profile obtained from the simulation. The normalization is performed as indicated in equation 1.9. Regions where the deposition profile lies above (below) the grey line receive an amount of snowfall larger (smaller) than the mean. The profile is obtained by averaging $\tilde{D}$ in the $y-$direction. 16

1.7 Trajectories of 100 snowflake particles from the moment they cross the vertical section upstream of the hill (outlined in black) to the moment they impact the surface or cross the lateral boundaries. 17

2.1 (a) Illustration of the DEM simulations: i) real snowflake (credit: Satoshi Yanagi, http://www1.odn.ne.jp/snow-crystals/page1_E.html), ii) simplified DEM description, iii) ratio between tensile stress σ in bonds and at the moment of the impact and tensile strength of ice σ_r, iv) fragmented snowflake (each level of grey represents a fragment). In the snow crystal model, the radius of the largest elements is 50 μm, while the radius of the smallest ones is 12.5 μm. (b) Cumulative size distribution (CD) of the dimensionless fragment size λ and corresponding frequency distribution (FD). (c) Influence of impact velocity and (d) impact angle on the average dimensionless fragment size $\langle\lambda\rangle$ and number of fragments N. The grey bands identify the ranges of impact velocity and impact angle typical of snow saltation, i.e., $0.5 < v_i < 1.5$ m/s and $5^\circ < \theta_i < 15^\circ$ [Araoka and Maeno, 1981]. . . 22

2.2 Schematic representation of the fragmentation process during saltation. Each crystal impact leads to formation of fragments having size equal to Λ times the original size. The number of children crystals follows from the scale-invariance property. Small fragments, formed after repeated impacts, are likely to be caught by turbulent eddies and transported to the suspension layer. 23

2.3 (a) Size-distribution of saltating snow crystals, modeled with the proposed fragmentation theory (dashed grey line), reported in published datasets [Gordon and Taylor, 2009, Nishimura et al., 2014, Nishimura and Nemoto, 2005, Schmidt, 1982b], and measured in the SLF wind tunnel in Davos, Switzerland (colored dots). Because the normalized distributions are sensitive to the specific range of sizes measured by the instruments, we rescaled the distributions such that all of them are tangent to a unique power-law (black dashed line) in the range where they show a scale-invariant behavior (200 ~ 500 μm). (b) Sensitivity analysis of the modeled blowing-snow size distribution to the fractal dimension γ. (c) Sensitivity analysis of the modeled blowing-snow size distribution to the dimensionless fragment size Λ. 26

3.1 Schematic representation of the impact-ejection dynamics. The impacting particle (blue circle) has mass m_i and velocity v_i. Upon impact, the particle can rebound (green circle) with velocity v_r and eject other particles (red circle) of mass m_n and velocity v_n. The reference system is such that the vertical plane (x, z) contains the impact velocity vector $\vec{v}_i$, which forms an angle α_i with the horizontal plane $\left(x, y\right)$. The rebound velocity vector $\vec{v}_r$ forms an angle α_r with the horizontal plane $\left(x, y\right)$, and an angle β_r with the vertical plane (x, z). Similarly, the ejection velocity vector $\vec{v}_n$ forms an angle α_n with the horizontal plane $\left(x, y\right)$, and an angle β_n with the vertical plane (x, z). 31

3.2 Mean number of ejections as predicted by equations 3.9 (blue line) and 3.10 (red line) for uniform sand with $\langle d \rangle = 1$ mm, $\sigma_d = 0$ mm and $\phi = 0$ J. The shadowed bands represent the errors introduced with respect to the exact energy and momentum balance equations 3.3 and 3.4. 35

3.3 (a) Predicted number of ejections (magenta line) for uniform sand with $\langle d \rangle = 1$ mm, $\sigma_d = 0$ mm. Black squares refer to wind-tunnel tests performed with uniform sand of size 800 μm [Werner, 1987]. Black circles refer to numerical simulations of uniform sand of size 1 mm [Anderson and Haff, 1988]. Vertical bars indicate standard deviations. The dashed black line is the ejection function of the COMSALT model [Kok and Renno, 2009]. (b) Predicted number of ejections for heterogeneous sand with $\langle d \rangle = 250$ μm, $\sigma_d = 50$ μm, including (solid magenta line) and neglecting (dashed magenta line) the negative correlation between ejecta's mass and velocity. The black markers refer to wind-tunnel studies carried out with a mixture of fine (150 – 250 μm), medium (250 – 355 μm) and coarse (355 – 600 μm) sand fractions [Willetts and Rice, 1985, Rice et al., 1996, 1995]. Vertical bars indicate standard deviations. Results of the COMSALT model (dashed black line) are shown as reference simulation of uniform sand ejection. Experiments [Oger et al., 2005, Beladjine et al., 2007, Ammi et al., 2009, Mitha et al., 1986] and models [Crassous et al., 2007] from sediments other than sand are omitted because different sphericity, elasticity and friction coefficients are likely to produce different ejection regimes. 36

3.4 (a) Number of snow ejections predicted by the momentum balance equation 3.10 (red line) and by the energy balance equation 3.9, for different values of cohesion ϕ (blue lines). Snow size distribution parameters are $\langle d \rangle = 200$ µm, $\sigma_d = 100$ µm. (b) Predicted number of snow ejections (magenta lines) resulting from the lower envelopes of the red and blue lines in Figure 3.4a. Black triangles refer to wind-tunnel studies on ejection of both fresh and compact snow [Sugiura and Maeno, 2000]. Black circles refer to ejection experiments carried out with densely packed ice particles and for impact angles between 5° and 15°, typical of saltation [Kosugi et al., 1995]. Vertical bars indicate standard deviations. The dashed black line refers to the empirical ejection function obtained by fitting a power-law to the compact snow data [Sugiura and Maeno, 2000]. 37

4.1 Time-averaged horizontal velocity field around the Gaussian ridge. 44

4.2 Longitudinal profile of the surface shear stress (averaged in time and along y). The red dashed line indicates the fluid threshold t_f. 45

4.3 Instantaneous distribution of surface shear stress. The black lines are iso-elevation curves of the Gaussian hill. The red mark on the colorbar indicates the value of fluid threshold, calculated with equation 4.1. 45

4.4 Snapshot of the snow transport process. White dots indicate the position of the snow parcels. 46

4.5 Time evolution of the ratio between splash entrainment and aerodynamic entrainment. 46

4.6 Time-averaged snow concentration field around the Gaussian ridge. 47

4.7 Longitudinal profiles of snow depth at the beginning (red dashed line) and at the end (black solid line) of the snow transport simulation. The longitudinal profiles are obtained by space averaging in the $y-$direction. 47

4.8 Particle size distributions of blowing snow (red line) and drifting snow (blue line). . . . 48

4.9 Time-averaged horizontal mass flux around the Gaussian ridge. Negative values indicate mass fluxes that are in the opposite direction to x. 48

5.1 (a) Subdivision of the catchment into source areas (sub-catchments) assumed to be independent hydrological control volumes. Each sub-catchment drains water into a single stream, which can be of order 1 or higher. (b) Trajectory of generic transport volumes, infiltrating at injection time t_i and leaving the control volume through evapotranspiration, after a travel time t_E, or through subsurface flow, after a travel time t_Q. . 54

5.2 Sample solutions of Eq. 5.18 for two different values of K_s. The solutions are obtained considering a constant storage $S(t) = 5$ m and the shown sinusoidal evolutions for $T_s(t)$ and $T_I(t)$. 59

5.3 Schematic representation of the mass and energy fluxes associated to the two modeled soil compartments. The upper compartment has a groundwater storage $S^u(t)$ with energy $H^u(t)$, while the lower one has a groundwater storage $S^l(t)$ with energy $H^l(t)$ (for an explanation of the variables see section 5.4). 60

5.4 (a) Sub-catchments and stream network delineation obtained applying the Taudem routines on a 25 m resolution digital elevation map [SwissTopo, 2005] and (b) 100 m resolution land use map of the Dischma catchment [Swiss Federal Office for Statistic, 2001]. 64

5.5 Distribution of the Nash-Sutcliffe indices (a) for streamflow simulations and (b) for stream temperature simulations. Black lines refer to the distributions of all Monte Carlo simulations, the filled bars refer to the distribution of the subset of 100 best temperature simulations ($NS_T > 0.69$) sampled among the 5% best streamflow simulations ($NS_Q >$ 91). It is observed that the NS_T distribution of the subset samples among the best temperature simulations of the Monte Carlo sets. 66

5.6 Distribution of the parameters of the hydro-thermal model, i.e. (a) R_{max}, (b) $\overline{\tau}^u$, (c) $\overline{\tau}^l$ and (d) K_s. Black lines show the distribution of the best 5% streamflow simulations, i.e. $NS_Q > 0.91$, while filled bars show the distribution of the subset of 100 best temperature simulations, i.e. $NS_Q > 0.91$ and $NS_T > 0.69$. The results suggest that a simultaneous calibration of streamflow and temperature reduces the uncertainty in the estimation of hydrological parameters. 66

5.7 Comparison between measured and modeled (a) streamflow and (b) stream temperature at the outlet, during the calibration period (October 2011 - October 2012). The solid lines represent the modeled results corresponding to the best NS indices (0.92 for streamflow and 0.73 for temperature), the dashed lines represent the measured data. The filled bands correspond to the interquartile range of the Monte Carlo simulations. Signals are averaged over 24 h. 67

5.8 Comparison between measured and modeled (a) streamflow and (b) stream temperature at the outlet during the validation period (October 2012 - October 2013). The corresponding indices are $NS_Q = 0.83$ and $NS_T = 0.81$. Signals are averaged over 24 h. 67

5.9 Comparison of the temperature evolution of subsurface flow as opposed to stream temperature at the outlet of the catchment for (a) the calibration period (October 2011 - October 2012) and (b) the validation period (October 2012 - October 2013). Signals are averaged over 24 h. 68

5.10 Spatial distribution of (a) specific streamflow (per unit drained area) and (b) stream temperature during the snowmelt event in May 2012. The streamflow pattern strongly reflects the patchy infiltration distribution during snowmelt. The stream temperature pattern reflects the heterogeneous distribution of soil temperature and meteorological forcings. 69

6.1 (a) Digital maps of aspects in the original orientation of the catchment and after applying rotations of 90°, 180° and 270°. In the text, we refer to these orientations as configuration A, B, C and D. (b) Series of nested catchment portions, for which the effect of solar radiation patterns is analyzed, and corresponding characteristic size d (see text for details on its computation). (c) Numerical and analytical variograms of aspect spatial field, normalized with respect to the total variance of the aspect field. 75

6.2 Hydrologic response in the four different configurations and for progressively larger - from (a) to (e) - catchment portions. The results are given in terms of specific streamflow per unit catchment area during the melting season of the year 2005. Signals are averaged over 24 h. 76

6.3 Coefficient of variation, across the four tested configurations, of (a) the incoming solar radiation field, (b) the snowmelt field and (c) the specific streamflow along the network. The values refer to the time averaged values of the first snowmelt peak 25th May - 1st June. 77

6.4 (a) Coefficient of variation of specific streamflow, as provided by Alpine3D at all nodes of the network, and (b) degree-day factors of the spatially-explicit hydrological model SEHR-ECHO [Schaefli et al., 2014], calibrated to match the streamflow computed by Alpine3D, versus the catchment size at the corresponding nodes. The catchment size is given both in terms of drainage area A and characteristic size d for comparison with the aspect correlation scale. Only the points corresponding to a Nash-Sutcliffe efficiency higher than 0.5 are shown (94% of the total). 78

A.1 Representation of the snow crystal model used in our DEM simulations of fragmentation. 86

A.2 Cumulative probability size distribution $P(D)$ of snowfall crystals, as measured for precipitation intensities of ~ 0.3 mm/h [Gunn and Marshall, 1958] (black dashed line), of a post snowfall surface crystals modeled by fragmentation of exponentially-distributed snowflakes (grey dashed line), and of a post blowing-snow surface after settlement of saltating crystals (grey solid line). The red dots refer to a surface particle size distribution measured by sieving analysis [Granberg, 1985]. 87

B.1 Sensitivity analysis of the model response to variations of the parameters by +20% and −20%. (a) Model responses to different values of μ_r, (b) μ_f, (c) ϵ_r, (d), r_E, and (e) r_M. . 93

C.1 Numerical variograms and fitted exponential models computed for (a) the Rein de Sumvitg, (b) the Ova da Cluozza and (c) the Lonza catchment. The catchment locations are shown in the inset. For details on catchments (a) and (b), see [Schaefli et al., 2013], for catchment (c) see [Schaefli et al., 2005]. 96

C.2 Patterns of (a) standard deviation and (b) coefficient of variation computed for SWE across the four tested catchment configurations. 97

List of Tables

3.1 Model parameters. (*) Estimates of the correlation coefficients are only available for sand (values $r_E = r_M = 0$ are assumed for snow). (**) Estimates of cohesion apply only to snow (a value $\phi = 0$ J is used for loose sand). Equations B.11 and B.12 are given in the supplemental materials. NA means not applicable. 34

5.1 List and meaning of symbols used in chapter 5. 53
5.2 A priori parameter ranges used for uniform parameter sampling during Monte Carlo simulations and sample set providing the best match with measured streamflow and temperature. Stream temperature simulation is affected by all the listed parameters, while stream flow is affected only by the first three. 63

A.1 Datasets of blowing-snow particle size distributions used to validate the model results. SPC indicates snow particle counter, while DC indicates digital camera. 87

Introduction

The hydrologic cycle in alpine terrain

The hydrologic cycle in alpine terrain is the result of meteorological, surficial, and underground processes driving the continuous transport of water on, above and below the surface [Brutsaert, 2005]. Water is here understood in a broad sense, which includes its solid, liquid, and gaseous phases. A large fraction of water is in fact provided in form of snowfall during winter time, stored on the surface until the start of the melting season, and subjected to evaporation and transpiration processes while transported toward the catchment outlet.

One of the main factors affecting the hydrologic response of alpine catchments is the spatial variability of snow depth and snow melt processes. The snow depth distribution in alpine terrain is highly heterogeneous [Trujillo et al., 2009], with flat areas usually presenting a larger amount of snow deposition with respect to slopes [Grünewald et al., 2010]. Such variability is largely due to atmospheric processes that alter the snowfall distribution before snow flakes deposit on the surface [Lehning et al., 2008, Mott et al., 2010]. On one hand, the complex topography may induce spatial heterogeneity in the cloud formation processes. On the other hand, near-surface interactions between turbulent flows and falling snow crystals may further alter the spatial distribution of snowfall. Wind-driven snow transport contributes to enhance the spatial variability of snow depth by redistributing snow from wind-ward to lee-ward mountain slopes [Lehning et al., 2008]. Snow transport presents two main regimes, namely drifting snow and blowing snow [Pomeroy and Gray, 1990]. Drifting snow is controlled by saltation dynamics and occurs near the surface [Pomeroy and Gray, 1990], while blowing snow is controlled by suspension dynamics and occurs at a higher elevation [Schmidt, 1982a]. Because airborne snow particles are relatively heavy, drifting snow accounts for the largest fraction of mass flux. Nevertheless, some of the smaller snow particles may gain enough momentum to reach a considerable elevation from the ground, where they become suspended in the turbulent flow. Snow transport is also responsible for other important processes, such as mechanical fragmentation of snow crystals [Sato et al., 2008] and mass loss through sublimation [MacDonald et al., 2010].

As for the snow melt, the largest cause of spatial variability lies in the heterogeneity of the two main energy sources, i.e., air temperature and solar radiation [Grünewald et al., 2010]. Air temperature, in particular, presents a large gradient in the vertical direction, the so-called lapse rate [Rolland, 2003]. Solar radiation, on the contrary, varies in space mostly depending on the slope aspect [Kumar et al., 1997]. The spatial distribution of snow melt provides the boundary conditions for the water transport dynamics at the hillslope scale [Botter et al., 2010]. From the hillslopes, water flows into the stream network and, eventually, to the catchment outlet [DeWalle and Rango, 2008]. In-stream transport includes advection and dispersion, of both kinetic and geomorphologic nature [Botter and Rinaldo, 2003]. Besides influencing timing and magnitude of the stream flow, these hillslope and in-stream processes also drive transport of solutes [Botter et al., 2005], such as chemicals and pollutants [Bertuzzo et al., 2013, Benettin et al., 2013b], and scalar quantities, such as temperature [Comola et al., 2015]. The latter, in particular, exerts a relevant control on the population dynamics of several aquatic species, which migrate within the river network of alpine catchments according to their temperature preferences [Coutant, 1977].

State of research

Most of the processes involved in the hydrologic cycle of alpine terrains are subject of active research. This thesis addresses some of the relevant open questions in the field of snow transport and hydrologic response, which are briefly introduced hereafter.

Preferential deposition

The snow deposition pattern in alpine terrain is significantly influenced by atmospheric boundary layer processes, which already alter the snowfall distribution before snow grains first touch the ground. Lehning et al. [2008] and Mott et al. [2010] investigated flow variations close to the ground and their impact on local deposition rates, describing the concept of preferential deposition. The influence of near-surface processes on snow deposition in alpine terrains was demonstrated by Scipión et al. [2013], who performed the first comparison of precipitation distribution, measured by radar, to snow depth distribution on the ground, measured by airborne laser scans. Further research is however necessary for a thorough understanding of preferential deposition. It is still unclear to what extent the process of preferential deposition is caused by flow-particle interactions close to the ground or by orography-induced precipitation formation in the clouds. Furthermore, in-depth investigations are necessary to assess the bias that preferential deposition may produce on estimations of snow depth distribution based on extrapolation of local snow depth measurements, which are often carried out in flat terrains [Wirz et al., 2011, Sommer et al., 2015, Grünewald and Lehning, 2015].

Snow fragmentation

Wind tunnel measurements [Sato et al., 2008] indicate that snowfall crystals experience fragmentation processes when they first touch the surface. Due to their smaller inertia, snow fragments are then easily entrained by the wind and transported in saltation [Clifton et al., 2006], where they further impact with the surface producing even smaller particles. Snow fragmentation dynamics may thus be the main reason for the significantly smaller size of blowing snow particles [Nishimura et al., 2014] with respect to large snowfall crystals [Gunn and Marshall, 1958]. Even though snow fragmentation dynamics are still largely unknown, they could potentially affect several snowpack properties. The size of the surface particles has a relevant influence on the snow albedo [Wiscombe and Warren, 1980] and on the vulnerability of the alpine slopes to wind erosion [Lehning et al., 2008] and avalanche release [Gaume et al., 2013]. Frequency and intensity of drifting-snow events could therefore exert a significant control on the surface mass and energy balance of alpine snow covers.

Drifting and blowing snow

The aerodynamic entrainment of snow occurs when the shear stress at the surface overcomes a value commonly known as ”fluid threshold”, representing the inertia and the cohesion of surface particles [Clifton et al., 2006]. The particles lifted from the surface follow ballistic trajectories close to the ground and eject other particles upon impact with the surface [Pomeroy and Gray, 1990]. During this process, known as saltation, particles progressively gain momentum at the expense of the flow field, which progressively slows down close to the surface until an equilibrium condition is reached. At steady-state, the surface shear stress attains a value called ”impact threshold”, which, according to the classic interpretation of Owen [1964], is just sufficient to keep the process going. Recent wind tunnel studies, however, suggest that the bed shear stress decreases with increasing shear stress outside the saltation layer [Walter et al., 2014]. Contrary to Owen’s initial assumption, splash entrainment is more efficient than aerodynamic entrainment in lifting particles from the surface [Kok et al., 2012, Paterna et al., in review]. As a result, snow transport decouples from the turbulent flow and develops its own length scales in fully developed saltation [Paterna et al., 2016]. Due to the large number of unknown variables in play, a comprehensive theory of splash entrainment has not yet been proposed. In state-of-the-art numerical models of drifting snow [Nemoto and Nishimura, 2004], splash entrainment is accounted for through empirical parameterizations, which are not able to capture the specific conditions of the snowpack, such as grain size distribution and cohesion. A better insight into impact-ejection dynamics may thus lead to significant improvements in quantifications of snow erosion in alpine terrains.

Hydrological and thermal response of alpine catchments

An appropriate description of near-surface snow accumulation and melting is required to correctly predict the hydrologic response in alpine terrain [D’Odorico and Rigon, 2003]. On one hand, physically based and spatially distributed models are capable of providing good quality simulations without the need of calibration [Rigon et al., 2006]. On the other hand, simpler models of snow accumulation and melting, such as temperature-index approaches, proved capable of providing results of comparable quality, provided that a careful calibration is carried out [Kumar et al., 2013]. The importance of detailed knowledge of small scale melt processes for predicting the hydrologic response at catchment scale is therefore still matter of scientific debate. Because temperature-index models require much less computational resources and meteorological information, they present an attractive choice for eco-hydrological applications. The drawback, however, is that the high level of parametrization impairs their spatial transferability to ungauged catchments, for which no calibration is possible. In particular, one of the most critical parameterizations is that concerning solar radiation [Ohmura, 2001]. A better understanding of how solar radiation influences the hydrologic response at different spatial scales in thus important to assess under which conditions temperature-index models are likely to be spatially transferable.

The thermal response of alpine catchments results from the interplay of advective energy fluxes, i.e., fluxes associated with water infiltration at the river bed, and of non-advective energy fluxes, such as radiative transfer and heat exchange at the interface between water and atmosphere. Studies have shown that when the length of the stream network becomes relevant with respect to the average size of the hillslopes, advective energy fluxes play a minor role and stream temperature approaches air temperature [Mohseni and Stefan, 1999]. In alpine terrain, however, the typical network length is not sufficient to reach such equilibrium and the relative importance of advective and non-advective fluxes is still subject of scientific research. The development of appropriate models that account for the complex energy and mass transport dynamics, both at hillsope scale and within the streams, is thus necessary to provide accurate stream temperature simulations in mountain catchments. Such modeling advances may also help addressing questions of broad relevance for stream ecology, such as the impact of climate change on the population dynamics of endangered aquatic species [Matulla et al., 2007].

Objectives and organization of the thesis

The objective of this thesis is to combine theoretical and numerical models to provide a better understanding of the transport processes driving the hydrologic cycle in alpine terrain. The most important requirement that these models must meet is the correct physical representation of the complex transport phenomena. The development of comprehensive physical models of the hydrologic cycle is however impaired by the large scale separation between the processes that drive snow transport and those that drive the hydrologic response at catchment scale. Accordingly, a "divide and rule" strategy is often applied to effectively decouple atmospheric and hydrologic transport models. This approach allows us, on one hand, to study snow transport processes in larger detail and, on the other hand, to account for their effect in hydrologic models through sub-grid parameterizations. A second relevant obstacle is represented by the complexity of the processes involved. For snow transport this complexity stems from the inherently chaotic nature of turbulence and the extremely diverse properties of snow particles, while for hydrologic transport it is due to the remarkable heterogeneity of surficial and underground formations.

Under these circumstances, deterministic models are often too simplistic a tool to describe the dynamics of the processes. Stochastic models, on the other hand, present the advantage of effectively embedding the uncertainties of the systems in the formulation of transport. As such, they offer a more appropriate tool for simulations of processes whose scale-separation extends beyond the spatial resolution allowed by computational resources, such as turbulence-particle interactions, or whose spatial heterogeneity cannot be properly represented in numerical models, such as hydrologic transport at catchment scale. We therefore propose and apply stochastic modeling frameworks to provide a deeper insight into snow transport and hydrologic response in alpine terrain.

The thesis is organized as follows:

- **Chapter 1**: We investigate the dynamics that drive preferential deposition of snowfall around hills. This study is carried out using large eddy simulation (LES) of turbulent flows and Lagrangian stochastic modeling (LSM) of snowflake trajectories. We account for the effect of topography on the surrounding flow through an immersed boundary method (IBM). We test the model set-up by comparing the simulation results to wind tunnel measurements of dust deposition over ranges of hills. We then apply the model to study the detailed flow-particle interactions that drive the heterogeneous snowfall deposition around a Gaussian ridge.
- **Chapter 2**: We propose a fragmentation theory for fractal snow crystals in saltation. The theory relies on the geometrical description of snow crystals provided by the Koch's snowflake. The assumptions of the theory are evaluated for more realistic snow crystal geometries through discrete element modeling of snow crystal breaking. We account for the theory in a statistical mechanics model of saltation to explain the transition from the size distribution of snowfall to that of blowing snow and the emergence of the scale-invariant range observed in blowing snow size distributions.
- **Chapter 3**: We derive a stochastic model of splash entrainment based on energy and momentum conservation laws. The model explicitly accounts for particle size distribution and cohesion, such that it can be employed to investigate the ejection process for a wide range of granular materials. We use the model to investigate the effect of cohesion and of heterogeneity in particle sizes on the ejection regime of sand and snow surfaces.
- **Chapter 4**: We apply our combined LSM-LES-IBM model to investigate wind-driven erosion and redistribution of snow in complex terrains. The model accounts for the complex series of processes involved in snow transport, namely aerodynamic entrainment, extraction of flow momentum, and splash entrainment. We use the model to study how the wind flow erodes and redistributes the snow around the Gaussian ridge considered in chapter 1, modifying the initial snow depth distribution resulting from preferential deposition of snowfall.
- **Chapter 5**: We propose a stochastic description of water and temperature dynamics in the hydrologic response of alpine catchments, based on the formulation of transport

by residence time distribution. The model relies on the surface boundary conditions provided by the physical and fully distributed snow model Alpine3D [Lehning et al., 2006]. The modeling framework is spatially explicit, which allows us to account for arbitrary degrees of geomorphological complexity. We apply the model to the Alpine Dischma catchment, Switzerland, to study the relative importance of subsurface versus in-stream processes on the yearly discharge and water temperature signals at the catchment outlet.

- **Chapter 6**: We apply our spatially-explicit hydrological model to investigate the scale-dependent effects of solar radiation patterns on the hydrologic response of snow-covered catchment. We expose the Dischma catchment to different solar radiation patterns via virtual rotations of the digital elevation model. The study indicates under which conditions a calibrated temperature-index model is likely to be spatially transferable for eco-hydrological applications.

1 Large eddy simulations of snowfall deposition in mountain terrain

An edited version of this chapter will be submitted for publication.

Comola, F., M. G. Giometto, M. B. Parlange, and M. Lehning (2016), Large eddy simulations of snowfall deposition in mountain terrain. In preparation.

F. C. implemented the Lagrangian stochastic model in the large eddy simulation model, took part in the research design, performed the research, analyzed the data, and wrote the chapter.

1.1 Abstract

Preferential snowfall deposition is one of the main controls on the spatial variability of snow depth in complex terrains. As such, it plays a key role in avalanche formation and hydrologic response of alpine regions. Here, we investigate the role of near-surface flow-particle interactions, as opposed to larger scale orographic processes, in driving preferential deposition at hillslope scale. We perform large eddy simulations (LES) of turbulent flows around ridges, accounting for the effect of the complex topography with an immersed boundary method (IBM). We compute the trajectories of falling snow flakes in the turbulent flow with a Lagrangian stochastic model (LSM) driven by LES fields. We first test our model results against wind tunnel experiments of dust deposition over ranges of hills. The comparison of numerical and experimental results indicates that the model can provide reliable predictions of the deposition pattern over complex surfaces. We then apply the model to simulate snowflake settling around a Gaussian hill, assigning a uniform precipitation rate at the upper boundary of the domain. Our model results highlight a significant heterogeneity in the deposition pattern. In particular, we observe a reduced deposition on the windward slope of the ridge, where the wind updrafts are effective in keeping snowflakes aloft, and on the sheltered leeward slope of the ridge. On the contrary, we observe an increased deposition on the hilltop and on the surrounding flat terrains. Overall, our results suggest that near-surface flow-particle interactions can explain large part of the snow depth heterogeneity at hillslope scale, even in absence of larger scale processes such as orographic precipitation or seeder-feeder mechanisms.

1.2 Introduction

Snowfall deposition in alpine terrains is one of the main controls on the spatial and temporal variability of the winter-time snow cover. A better understanding of processes and interactions leading to heterogeneous snowfall deposition may thus help improving avalanche forecasting, hydrological modeling, and water resources management.

Previous studies indicated that inhomogeneous snowfall distribution is the result of physical processes acting at different spatial scales [Mott et al., 2014]. At large scales, orographic precipitation is likely to be larger on the windward side of large mountains, where cloud formation is enhanced by updrafts of moist air [Houze, 2012]. At intermediate scales, an increase of precipitation around the hilltops may occur due to seeder-feeder mechanism, consisting of accretion of precipitation particles formed in an upper-level cloud that fall through a lower-level cloud capping the mountain top [Choularton and Perry, 1986]. At smaller scales, near-surface flow-particle interactions can lead to a larger deposition on the leeward slopes with respect to the windward slope [Zängl, 2008, Orlandini and Lamberti, 2000]. The importance of these small scale processes was confirmed by Scipión et al. [2013] through radar measurements, which indicated that the spatial variability of snowfall far above the surface is not sufficient to explain the much larger variability in snow deposition.

The concept of small-scale preferential deposition was first introduced by Lehning et al. [2008], who defined it as "the spatially varying deposition of precipitation due to the topography induced flow field modification close to the surface". Therein, the authors argued that on the windward side of a mountain the strong updrafts reduce the settling velocity of the snow particles, yielding a reduced deposition. This, in turn, leads to an increase of snow concentration in the air that flows uphill towards the hilltop. Once on the leeward side, the reduced velocity and the large concentration of snow induce a local increase of deposition.

To date, several uncertainties still impair our understanding of preferential deposition. Most numerical simulations performed thus far adopted a simplified description of the transport process, based on a stationary form of the advection-diffusion equation that does not include the effect of particle inertia. Although recent modeling studies sought a solution of the advection-diffusion dynamics of inertial particles with large eddy simulations [Salesky et al., in review], uncertainties in the subgrid-scale eddy diffusivity and in the boundary conditions for the deposition rate may impair the representativeness of Eulerian approaches in the near-surface region. Here, we propose a novel and comprehensive modeling framework for the study of preferential deposition, based on large eddy simulations (LES) of the flow field and Lagrangian stochastic modeling (LSM) of snow particle trajectories. We account for the form drag exerted by the surface topography on the surrounding flow through an immersed boundary method (IBM). We perform simulations of snowfall deposition around an idealized hill, modeled with a Gaussian function, to provide a deeper insight into the basic physical processes leading to inhomogeneous snow depth. This study may help assessing the contribution of near-surface processes, as opposed to cloud processes, in driving preferential deposition in alpine terrain.

In section 1.3, we provide the details of the LES-LSM model developed for this study. In section 1.4, we perform a model validation against wind tunnel measurements of dust deposition over ranges of hills. In section 1.5, we present the model results on snowfall deposition around an isolated Gaussian hill. Discussion and conclusions close the chapter.

1.3 Methods

1.3.1 Large eddy simulations

The LES approach aims at solving the energy-containing scales of the turbulent flow while providing an appropriate model for the small-scale motions [Pope, 2001]. These small scales ideally belong to the inertial subrange, whose dynamics present well known characteristics and thus allow us to develop effective parameterizations. We adopt an LES model that solves the isothermal filtered Navier-Stokes equations [Orszag and Pao, 1975]

$$\frac{\partial \tilde{u}_i}{\partial t} + \tilde{u}_j \left(\frac{\partial \tilde{u}_i}{\partial x_j} - \frac{\partial \tilde{u}_j}{\partial x_i} \right) = -\frac{\partial \tilde{\pi}}{\partial x_i} - \frac{\partial \tau_{ij}^{SGS}}{\partial x_j} - \Pi_1 + \tilde{f}_i^{\Gamma_s} + \tilde{f}_i^{p} \qquad \text{in } \Omega \times [0,T], \tag{1.1a}$$

$$\frac{\partial \tilde{u}_i}{\partial x_i} = 0 \qquad \text{in } \Omega \times [0,T], \tag{1.1b}$$

$$\frac{\partial \tilde{u}_1}{\partial x_3} = \frac{\partial \tilde{u}_2}{\partial x_3} = \tilde{u}_3 = 0 \qquad \text{in } \Gamma_t \times [0,T], \tag{1.1c}$$

$$(\tilde{\mathbf{u}} \cdot \tilde{\mathbf{n}})\, \tilde{\mathbf{n}} = \tilde{\mathbf{u}}_n = 0 \qquad \text{in } \Gamma_s \times [0,T], \tag{1.1d}$$

$$\tilde{\mathbf{t}} = -\left[\frac{k\,(\tilde{\mathbf{u}} - \tilde{\mathbf{u}}_n)}{\ln\left(1 + \frac{\Delta}{z_0}\right)} \right]^2 \qquad \text{in } \Gamma_s \times [0,T]. \tag{1.1e}$$

In equations 1.1, the tilde indicates filtered quantities. $\tilde{u}_i$ are the velocity components in the three cartesian directions ($i = 1,2,3$), $\tilde{\pi} = \tilde{p}/\rho + 1/3\,\tau_{ii}^{SGS} + 1/2\,\tilde{u}_i\,\tilde{u}_i$ is a modified filtered pressure field, ρ is the air density, Π_1 is a pressure gradient introduced to drive the flow, and τ_{ij}^{SGS} is the sub-grid scale stress tensor. Further, $\tilde{f}_i^{\Gamma_s}$ is the forcing term arising from the immersed boundary method, while $\tilde{f}_i^{p}$ is a forcing term that includes the effect of inertial particles on the filtered flow. $\tilde{\mathbf{n}}$ is the normal direction to the surface. $\tilde{\mathbf{u}}_n$ and $\tilde{\mathbf{t}}$ are the normal-to-surface velocity vector and the surface stress vector, respectively. Equation 1.1e expresses the law of the wall in the normal direction to the surface, where $\Delta = \left(\Delta_x \times \Delta_y \times \Delta_z\right)^{1/3}$ is the filter width and z_0 is the aerodynamic roughness.

This LES model has been previously used to investigate land-atmosphere interactions [Albertson and Parlange, 1999], wind-farm effects on the atmospheric boundary layer [Sharma et al., 2016], turbulent flows over realistic urban surfaces [Giometto et al., 2016], and to test linear and non-linear SGS models [Meneveau et al., 1996, Porté-Agel et al., 2000, Bou-Zeid et al., 2005].

We solve the equations on a regular domain Ω using a pseudo spectral collocation approach [Maday and Quarteroni, 1982] in the horizontal directions and a second-order accurate centered finite differences scheme in the vertical direction. We perform the time integration in the interval $[0,T]$ adopting a fully explicit second-order accurate Adams-Bashforth scheme and employ a fractional step method to compute the pressure field. We apply different conditions at the partitions of the computational boundary $\partial\Omega = \Gamma_s \cup \Gamma_t \cup \Gamma_l$, that is, a free-lid boundary conditions at the upper boundary Γ_t (equation 1.1c), a no-slip boundary condition at the surface Γ_s (equation 1.1d), and periodic conditions at the lateral boundaries Γ_l due to the Fourier expansions used in the pseudo spectral approach.

Previous model applications with the immersed boundary method [Giometto et al., 2016] highlighted that, when form drag accounts for a large fraction of the surface drag, model results are not significantly sensitive to the choice of sub-grid closure model. We therefore rely on the simple static Smagorinsky closure model to evaluate τ_{ij}^{SGS} in combination with a wall dumping function [Mason and Thomson, 1992]. This model evaluates the SGS terms as functions of the LES-resolved strain rate tensor

$$\tau_{ij}^{SGS} = -2\nu_t \tilde{S}_{ij} = -2\left(c_s\Delta\right)^2 |\tilde{S}|\tilde{S}_{ij}, \tag{1.2}$$

where ν_t is the eddy viscosity, $\tilde{S}_{ij}$ is the filtered shear rate tensor, and c_s is the Smagorinsky coefficient. Although c_s is a function of the local properties of the flow, a constant value $c_s = 0.16$ can be theoretically derived in case of homogeneous turbulence. However, because c_s should approach 0 in the near wall region, we adopt a wall dumping function to avoid over-dissipation of kinetic energy.

1.3.2 Immersed boundary method

We represent the complex topography $\Gamma_s\left(x,y\right)$ adopting a signed distance function $\tilde{\phi}\left(x,y,z\right)$, such that the computational domain is partitioned in two regions, i.e., the below-surface region Ω_s where $\tilde{\phi}\left(x,y,z\right) < 0$, and the above-surface region Ω_f where $\tilde{\phi}\left(x,y,z\right) > 0$. The surface topography is then identified by the zero level-set $\tilde{\phi}\left(x,y,z\right) = 0$. Our implementation of the immersed boundary method is similar to the one proposed in [Chester et al., 2007], and has been recently used to investigate the characteristics of urban canopy layers [Giometto et al., 2016].

We fix the velocity field to zero in the inside region Ω_s and enforce the law-of-the-wall (Equation 1.1e) in all the grid nodes that fall in the region $-1.1\Delta < \tilde{\phi}\left(x,y,z\right) < 1.1\Delta$. Because the solution of Equations 1.1 is of class C^0, i.e., with discontinuous first derivatives, in any horizontal plane intersecting the lower boundary Γ_s, the spectral representation of the flow field results in strong Gibb's oscillations at the interface between the flow and the surface. To mitigate this drawback, we perform a Laplacian smoothing of the velocity field in Ω_s before the spectral differentiation step [Tseng et al., 2006].

1.3.3 Lagrangian stochastic model

The LSM provides us with an evolution equation for the SGS velocity of fluid parcels in turbulent flows. Used in combination with the LES, it allows us to account for the full turbulence spectrum and thus to perform accurate simulations of particle dispersion. We implement a modified version of the LSM proposed by Thomson [1987]. Therein, the author derived a stochastic evolution equation for the velocity fluctuations of a fluid parcel based on the local ensemble-mean velocity and velocity variances of the flow. Here, we substitute the ensemble-mean velocity with the LES-resolved velocity, and calculate the velocity variances based on the SGS closure model. A similar LSM approach was previously used to simulate the dispersion of passive tracers in a convective boundary layer [Weil et al., 2004] and the aeolian transport of snow particles [Zwaaftink et al., 2014].

If the SGS velocity component is isotropic, as commonly assumed in LES closure models, we can express the stochastic evolution of a fluid parcel's SGS velocity as

$$\mathrm{d}u_i^{SGS} = -\frac{f u_i^{SGS}}{T_f}\mathrm{d}t + \frac{1}{2}\left(\frac{1}{\sigma^2}\frac{\mathrm{d}\sigma^2}{\mathrm{d}t}u_i^{SGS} + \frac{\partial\sigma^2}{\partial x_i}\right)\mathrm{d}t + \left(\frac{f 2\sigma^2}{T_f}\right)^{1/2}\mathrm{d}\xi_i \tag{1.3}$$

where $\sigma^2 = 2e/3$ is the SGS velocity variance in isotropic turbulence, which is directly proportional to the SGS turbulence kinetic energy e. We indicate with f the SGS fraction of the total turbulence kinetic energy, and with $\mathrm{d}\xi_i \sim \mathcal{N}(0, \mathrm{d}t)$ a random number sampled from a normal distribution of zero mean and variance $\mathrm{d}t$. $T_f = 2\sigma^2/C_0\epsilon$ is the velocity autocorrelation timescale.

The first two terms on the right-hand-side of Equation 1.3 are deterministic and form the so-called drift term. The last term, instead, is the dispersion term, which embeds the stochasticity of the process. Thomson [1987] derived the drift term from first turbulence principles, i.e., the expression of the second-order structure function in high-Reynolds-number flows. The dispersion term, instead, follows from the so-called well-mixed condition, which means that if the particles of a passive tracer are initially well-mixed in a certain region, they remain so.

It is worth noting that heavy particle do not follow the same trajectories as the fluid parcels. Therefore, equation 1.3 cannot be employed as-is to predict the turbulence fluctuations felt by the heavy particles. The effective solution proposed by Wilson [2000] consists in reducing the velocity autocorrelation timescale T_f, such that a modified version equation 1.3 can be used to predict the turbulence fluctuation in the positions of the heavy particles. We therefore replace T_f with T_p [Wilson, 2000]

$$T_p = \frac{T_f}{\sqrt{1 + \left(\frac{\beta u_{p,3}}{\sigma}\right)^2}}, \tag{1.4}$$

where $u_{p,3}$ is the vertical component of the particle velocity, $C_0 = 4 \pm 2$ is a dimensionless constant and ϵ is the turbulence dissipation rate. $\beta \approx 2$ is a calibration coefficient suggested by Wilson [2000].

In equation 1.3, $e = \epsilon\Delta/c_\epsilon$, where Δ is the filter size and $c_\epsilon = 0.93$ in neutral and unstable stratification [Pope, 2001]. We compute the turbulence dissipation ϵ assuming that, over sufficiently large time intervals, the mean energy production equals the mean energy dissipation [Kolmogorov, 1941b]. We thus perform a time average of the energy production term P over sufficiently long time intervals and then compute the energy dissipation in each grid node as

$$\epsilon \approx \langle P \rangle = \langle -\tau_{ij}\tilde{S}_{ij} \rangle. \tag{1.5}$$

We then compute the Lagrangian trajectories of the snow particles based on drag and gravity forces.

Assuming spherical particles for simplicity, we obtain

$$\mathrm{d}u_{p,i} = \left[\frac{3}{4}\frac{C_d}{d_p}\frac{\rho}{\rho_p}|\mathbf{u}_r|\left(\tilde{u}_i + u_i^{SGS} - u_{p,i}\right) - \delta_{i,3}g\right]\mathrm{d}t, \tag{1.6}$$

where $u_{p,i}$ indicates the particle velocity in direction i, d_p the particle diameter, and ρ_p the snow density, g the acceleration of gravity. We indicate with $\mathbf{u}_r = \tilde{\mathbf{u}} + \mathbf{u}^{SGS} - \mathbf{u}_p$ the relative velocity vector between the flow and the particle. Further, C_d is drag coefficient, which we express as [Doorschot and Lehning, 2002]

$$C_d = \frac{24}{\mathrm{Re}_p} + \frac{6}{1 + \mathrm{Re}_p^{1/2}} + 0.4, \tag{1.7}$$

where $\mathrm{Re}_p = |\mathbf{u}_r|d_p/\nu$ is the particle's Reynolds number and ν is the kinematic viscosity of the air.

We perform a time integration of Equation 1.6 with a second-order accurate Verlet scheme [Verlet, 1967]. After updating particle position and velocity, we compute the forcing term $\tilde{f}_i^p$ in Equation 1.1a as

$$\tilde{f}_i^p = -\frac{1}{\rho\Delta^3}\sum_{k=1}^{N} f_{d,k}, \tag{1.8}$$

where N is the local number of particles per node and $f_{d,k}$ are the drag forces that the flow exerts on the inertial particles.

1.4 Model validation

Here, we test the model accuracy in predicting the settling of inertial particles in turbulent flows over complex topographies. We simulate a wind tunnel study of dust deposition over ranges of hills, described in Goossens [1996]. Therein, the author provides measured dust deposition profiles over hills with different length/height ratios l/h. We consider here the deposition profile over a range of six hills, with height of 4 cm and $l/h = 7$. The domain size is $L_x = 6l = 168$ cm, $L_y = 84$ cm , and $L_z = 50$ cm, discretized with a Cartesian grid having $N_x \times N_y \times N_z$ nodes, where $N_x = 128$, $N_y = 64$, and $N_z = 99$. The computational time step is $\Delta t = 2 \times 10^{-4}$ s.

Following the experimental procedure described in Goossens [1996], we first carry out an LES simulation to reach the design flow conditions in the wind tunnel, that is, a free stream velocity $U_\infty \approx 2$ m/s. Afterwards, we simulate a particle release from the rooftop of the wind tunnel, such as to match the mean dust concentration $\langle C\rangle \approx 1.5$ g/m^3 measured in the experiments. We sample the particle diameter from a lognormal distribution $d_p \sim \log\mathcal{N}\left(\langle d_p\rangle, \sigma_d\right)$, with a mean diameter $\langle d_p\rangle = 30$ μm and arithmetic standard deviation $\sigma_d = 7$ μm, as indicated in Goossens [1996]. We assign the dust density $\rho_p = 2600$ kg/m^3 [see, e.g., Hess et al., 1998]. If particles cross the lateral boundaries, they are re-located in the opposite side of the domain at the same elevation, to be consistent with the periodic boundary conditions of the flow field.

Figure 1.1 shows the time-averaged flow field, characterized by stagnation regions in the topographic depressions. The distance between the hills is in fact not sufficient for a partial recovery of the flow after the obstacles. Moreover, we observe that the flow recovers horizontal homogeneity at an elevation of approximately 20 cm above the hilltops, that is, five times the height of the hills.

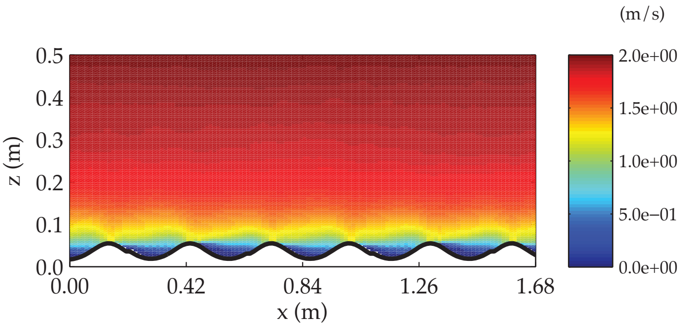

Figure 1.1 – Time-averaged velocity field over the ranges of six hills. The hills are modeled according to the experimental set-up described in Goossens [1996].

In Figure 1.2, we show concentration profile around the hills. We observe that the topographic depressions do not significantly profit from a longitudinal dust supply, due to sheltering effect provided by the upstream hills. On the contrary, dust is supplied primarily from above by the descending plume, as also observed in the experimental study [Goossens, 1996].

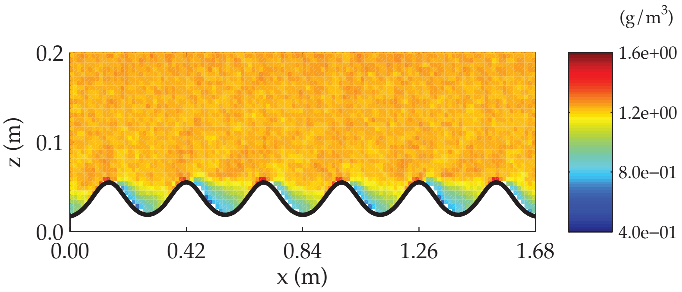

Figure 1.2 – Time-averaged concentration field over the ranges of six hills. The hills are modeled according to the experimental set-up described in Goossens [1996].

Every time a dust particle settles on the surface, we identify the closest surface node and update the corresponding deposition $\tilde{D}$ $\left(\mathrm{kg/m^2}\right)$. The amount of dust deposited on each surface node increases with the duration of the simulation. Because an LES of the same duration of the wind-tunnel experiment by Goossens [1996] (15 minutes) would require several millions time steps, a comparison in terms of $\tilde{D}$ is computationally prohibitive. We therefore decide to preform the comparison in terms of normalized deposition

$$\tilde{\delta} = \frac{\tilde{D} - \langle \tilde{D} \rangle}{\sigma_D}, \tag{1.9}$$

where $\langle \tilde{D} \rangle$ and σ_D are the spatial mean and standard deviation of $\tilde{D}$. We observe, in fact, that the spatial pattern of normalized deposition does not show significant variations in time after about 60 s from the start of the simulation. This allows us to run a relatively short simulation (200 s) for the purpose of comparing measured and modeled results.

We show the normalized deposition profile obtained from the model in Figure 1.3 (black line), together with the deposition profile measured by Goossens [1996] (red line). The comparison shows a good match between numerical results and measured data, although the model tends to underestimate the deposition minima in correspondence of the central hills. This may be due to a larger sheltering effect in the model, possibly caused by a overestimation of the real wind velocity in our simulations. We also notice that the measured profile shows larger differences from hill to hill compared to the model, in part because the periodic boundary conditions do not allow us to distinguish among upwind and downwind hills. Nevertheless, the coupling between LES-IBM and LSM seems capable of describing with sufficient accuracy location and value of deposition maxima and minima.

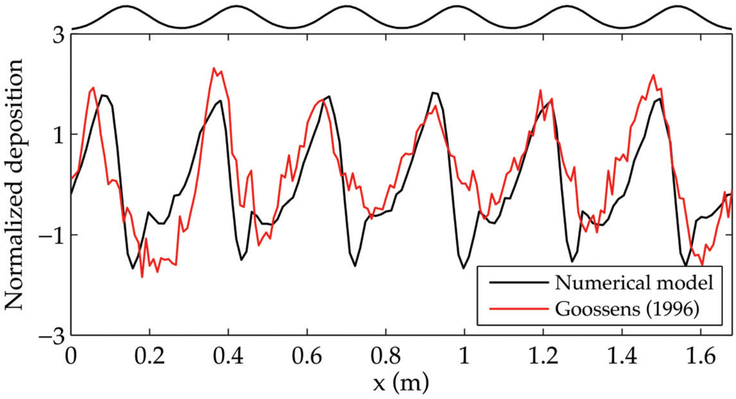

Figure 1.3 – Normalized deposition profile obtained from the simulation (black line) and from the wind tunnel experiments (red line). The normalization is performed as indicated in equation 1.9. The profile is obtained by averaging $\tilde{D}$ in the $y-$direction.

1.5 Simulation of snowfall deposition

We employ the model set-up to simulate a snowfall event around a bi-dimensional ridge, in neutrally stable atmospheric conditions. The ridge, perpendicular to the mean flow, has a Gaussian shape with height of 10 m and base of 40 m. We locate the ridge in a computational domain with side lengths $L_x = 200$ m, $L_y = 50$ m, and $L_z = 50$ m. We solve the LES equations in a cartesian grid with $N_x = 256$, $N_y = 64$, and $N_z = 99$ nodes in the $x-$, $y-$, and $z-$ directions, resulting in spatial resolutions $\Delta x = \Delta y = 0.78$ m and $\Delta z = 0.51$ m. The simulation time-step is $\Delta t = 5 \times 10^{-3}$ s. This simulation set-up results from a compromise between the spatial resolution and the domain size. On one side, in fact, we aim at resolving the flow field and the deposition pattern around the ridge at high spatial resolution. On the other side, the flow approaching the ridge should not be significantly affected by the periodicity of the boundary conditions, which requires a long domain.

Because we focus on snow deposition in absence of wind erosion, we simulate relatively light wind conditions such that the shear stress at the surface is far below the threshold of snow saltation. The mean flow field, shown in the left panel of Figure 1.4, presents a separation point at the hilltop, and a recirculation region beyond the ridge. In the right panel of Figure 1.4, we show the velocity profiles in the cross sections S1, S2, S3, located upstream, above, and downstream of the ridge.

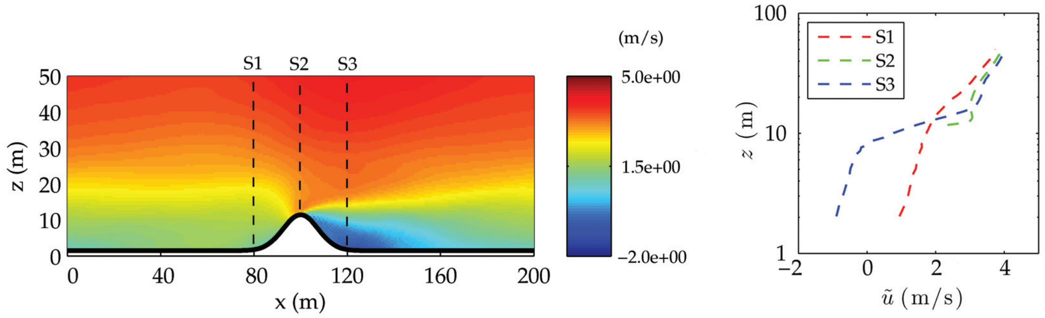

Figure 1.4 – (Left) Time-averaged velocity field around the Gaussian ridge. (Right) Velocity profiles upstream (S1), above (S2), and downstream (S3) of the ridge.

We release snowfall particles from an horizontal plane at 40 m elevation. The precipitation has intensity of 10 mm/h, is constant in time and uniform over the horizontal plane. The particle size distribution is log-normal, with $\langle d \rangle = 2$ mm and $\sigma_d = 0.1$ mm. If snow particles cross the lateral boundaries, they are re-located in the opposite side of the domain at the same elevation.

Numerical studies by [Huang et al., 2011] suggest that the complex shape of some snow crystals may significantly affect the flow-particle interactions. Therein, the authors adopt a modified versions of equation 1.7, initially proposed by List and Schemenauer [1971] and Loth [2008], to account for the effect of complex particle geometries. Snowflakes may present extremely variable shapes, such as needles, columns, plates, dendrites, irregular rimed flakes, and even aggregates. Because the sensitivity of snowfall deposition to all these different shapes is beyond the scope of this study, and for the sake of generality, we only partially account for the aspherical properties of snowflakes by reducing the effective particle density ρ_p. Magono [1965] and Passarelli and Srivastava [1979], in fact, collected a large number of natural snowflakes and observed that their effective density approximately decays with the square of their diameter. According to their studies, for the particle size considered here, the equivalent snowflake density ρ_p is of the order of 500 kg/m^3.

Figure 1.5 shows a snapshot of the snowfall simulation at time $t = 25$ s, when the first snowflakes reach the surface. We observe that the initially horizontal precipitation front is significantly distorted by the near surface flow. The updrafts surging from the windward side of the ridge, in fact, are very efficient in keeping particles aloft around the obstacle. Conversely, upwind and downwind of the obstacle, particles face a significantly smaller vertical drag and reach the surface earlier.

Figure 1.6 shows the normalized deposition pattern, calculated with equation 1.9. The results indicate an overall reduced deposition on both the windward and leeward side of the ridge. We notice, however,

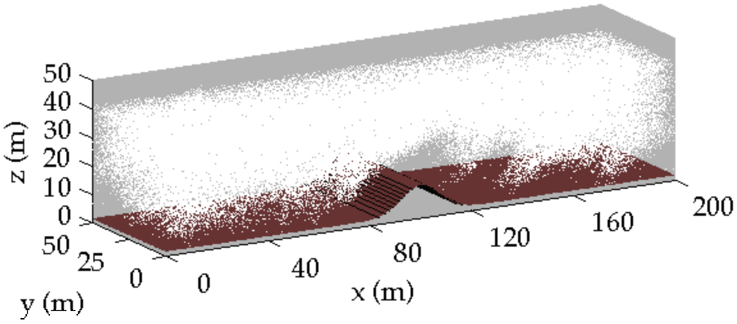

Figure 1.5 – Snapshot of the snowfall simulation at time $t = 25$ s.

a visible local maximum on the windward side of the hilltop, which is consistent with experimental observations of dust deposition over isolated hills [Goossens, 2006]. Deposition is overall increased over the flat surfaces around the obstacle.

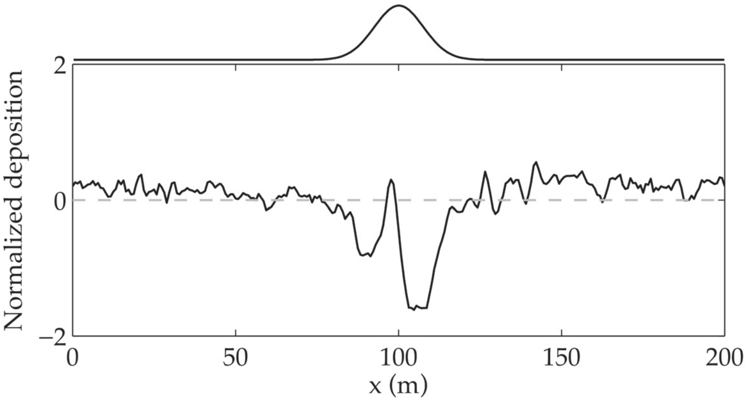

Figure 1.6 – Normalized deposition profile obtained from the simulation. The normalization is performed as indicated in equation 1.9. Regions where the deposition profile lies above (below) the grey line receive an amount of snowfall larger (smaller) than the mean. The profile is obtained by averaging $\tilde{D}$ in the $y-$direction.

To better understand the dynamics leading to such deposition pattern around the obstacle, we draw a sample of 100 snowflake particles crossing a vertical section upstream of the ridge (black line in Figure 1.7) and track their trajectories. The results, shown in Figure 1.7, indicate that the updrafts on the windward side of the ridge deflect the trajectories upwards, preventing several snowflakes from impacting the windward slope. Some of these snowflakes eventually settle on the hilltop or enter the recirculation region behind the ridge, where their trajectories are diverted downwards.

1.6 Discussion and conclusions

We proposed a comprehensive modeling approach to simulate snowfall deposition over complex topographies. We used large eddy simulations combined with a Lagrangian stochastic model to simulate snow particle dynamics. An immersed-boundary method is used to account for the relevant drag exerted by the topography on the surrounding flow. We tested the performance of the model

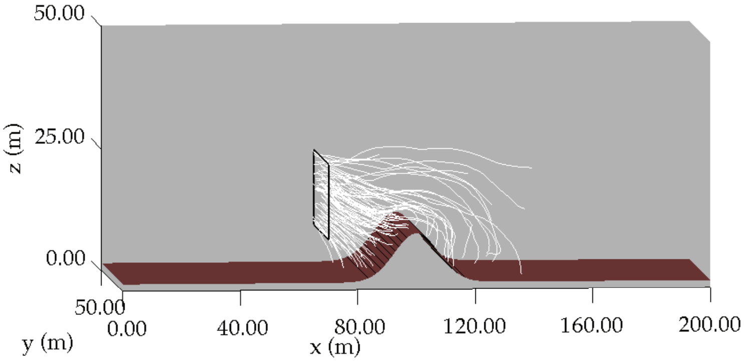

Figure 1.7 – Trajectories of 100 snowflake particles from the moment they cross the vertical section upstream of the hill (outlined in black) to the moment they impact the surface or cross the lateral boundaries.

by comparing numerical and experimental results of dust deposition over ranges of hills. The results indicated that the model predicts location and value of deposition maxima and minima with sufficient precision.

We then applied the model to simulate snowflake deposition around a Gaussian ridge, with axis perpendicular to the stream-wise direction, under light wind conditions. We prescribed a spatially homogeneous snowfall far above the surface, in order to single out the effects of near-surface flow-particle interactions on the deposition pattern. The model results indicated that preferential deposition occurs, in particular over the flat terrain in the wake of the ridge. Conversely, we observed an overall reduced deposition on the windward and leeward sides of the hill. On the windward side, in fact, the strong wind updrafts are efficient in keeping particles aloft and reducing the deposition rate. The leeward slope, instead, is subjected to a significant sheltering effect and thus receives a limited supply of snowflakes. Nevertheless, the results indicate a local deposition maximum at the hilltop. To better understand the dynamics leading to this deposition pattern, we visualized the trajectories of snowflakes around the obstacle. We observed that the trajectories of snowflakes approaching the windward side of the hill are often deflected upwards by the wind updrafts, such that several particles concentrate and eventually settle over the hilltop. The snowflakes that surpass the ridge are likely to be caught in the recirculation region and to settle behind the obstacle. The reduced deposition on the leeward side is mainly due to the sheltering that limits the horizontal supply of snowflakes.

These observations mostly support what was initially argued by Lehning et al. [2008] regarding the causes for preferential deposition. Furthermore, our results suggest that near-surface flow-particle interactions are a major control on the deposition process at hillslope scale and that a significant preferential deposition can occur in absence of large scale effects, such as orographic precipitation and seeder-feeder mechanism.

Further investigations are however necessary to provide a more complete understanding of the process. In particular, the influence of several key factors has to be clarified. As the ridge becomes steeper, for instance, an additional deposition maximum at the toe of the windward slope may appear as soon as the blocking effect on the flow becomes relevant. Moreover, the deposition profile may change depending on the hill size, given that turbulent flow and particle dynamics obey different similarity scalings. A deeper insight into the different factors affecting snow deposition may lead to more precise assessments of the snow height distribution over real alpine topographies, and thus to relevant improvements in avalanche forecasting, hydrological modeling, and water resources management.

1.7 Acknowledgments

I wish to thank Dirk Goossens for sharing his experimental data on dust deposition over ranges of hills and Marco Giometto for his support in the implementation and application of the LES code.

2 Fragmentation of wind-blown snow crystals

An edited version of this chapter was submitted for publication to the journal *Geophysical Research Letters*.

Comola, F., J. F. Kok, J. Gaume, E. Paterna, and M. Lehning (2016), Fragmentation of wind-blown snow crystals, Geophys. Res. Lett., In review.

F. C. took part in development of the theoretical and modeling frameworks, took part in the research design, performed the research, collected literature data, analyzed the data, and contributed to the writing of the paper.

2.1 abstract

Understanding the dynamics driving the transformation of snowfall crystals into blowing-snow particles is critical to correctly account for the energy and mass balances in polar and alpine regions. Here, we propose a fragmentation theory of fractal snow crystals that explicitly links the size distribution of blowing snow particles to that of falling snow crystals. We use discrete element modeling of the fragmentation process to support the assumptions made in our theory. By combining this fragmentation model with a statistical-mechanics model of blowing-snow, we are able to reproduce the characteristic features of blowing-snow size distributions measured in the field and in a wind tunnel. In particular, both model and measurements show the emergence of a self-similar scaling for large particle sizes and a systematic deviation from this scaling for small particle sizes.

2.2 Introduction

The size of snow surface particles plays an outsize role in determining the radiative balance [Flanner and Zender, 2006] in polar and alpine regions. A key factor that determines the size distribution of snow particles is the transformation of snowflakes once they impact the surface. In particular, measurements [Sato et al., 2008] show that, even in light winds, many snowflakes break upon collision with the surface, and that the number of fragments increases with impact velocity. Fragmentation of snow crystals blown by wind might explain the remarkable differences in size between snowflakes and blowing snow particles [Gunn and Marshall, 1958, Schmidt, 1982b]. Snowfall crystals are relatively large, up to a maximum of 2 ~ 5 mm depending on precipitation intensity, and generally follow an exponential size distribution [Woods et al., 2008, Garrett and Yuter, 2014]. In contrast, blowing-snow particles span the size range 50 ~ 500 μm with a frequency distribution well described by a gamma function [Nishimura and Nemoto, 2005, Nishimura et al., 2014].

Measurements [Legagneux et al., 2002] suggest that, when wind shatters large dendritic crystals into small fragments, the specific surface area of a fresh snow cover significantly decreases. Because specific surface area has been identified as one of the main controls on the optical properties of snow surfaces [Domine et al., 2006], blowing-snow fragmentation may significantly reduce snow surface albedo in alpine and polar regions, and thus play a key role in the energy budget. Furthermore, the size-distribution of deposited snow partially determines the mechanical properties of alpine snow covers and thus their vulnerability to wind erosion [Gallée et al., 2001] and avalanche danger [Gaume et al., 2017]. Moreover, fragmentation processes intensify snow sublimation, which is not only responsible for a significant loss of snow mass in snow-covered regions [Lenaerts et al., 2012, MacDonald et al., 2010], but also for bromine aerosols release and seasonal ozone depletion in Antarctica [Yang et al., 2008, Lieb-Lappen and Obbard, 2015].

Here, we propose that fragmentation of snow particles while they are blown by wind is the missing link that connects the size distribution of precipitating snowflakes to that of deposited snow crystals. Specifically, we propose a physical and mathematical description of snow fragmentation, based on the fractal geometry of dendritic snow crystals. We evaluate the assumptions of the theory through discrete element simulations of snow crystal breaking. We finally derive and apply a statistical-mechanics model of saltation, which incorporates the proposed fragmentation processes, to establish the missing connection between snowfall and blowing-snow size-distributions.

2.3 Snow crystal fragmentation

When wind blows over a fresh snow cover, snow crystals are lifted through aerodynamic or splash entrainment [Clifton and Lehning, 2008, Comola and Lehning, 2017], follow ballistic trajectories in the saltation layer and eventually impact the surface, thereby producing smaller fragments [Sato et al., 2008]. Large fragments follow the same dynamics, break further and progressively gain momentum until they are small enough to be transported in suspension by turbulent eddies [Pomeroy and Gray, 1990]. These fragmentation processes are controlled by the kinetic energy and mechanical properties of the wind-blown sediment [Kok, 2011]. When subjected to impulsive forces, ice behaves as a brittle material [Kirchner et al., 2001, Weiss, 2001], presenting a linearly elastic response up to a failure stress at which fracture occurs. In brittle objects, such as ice solids, crack propagation dynamics depend on the impact energy. Low energies generate the so-called damage regime, yielding a few fragments having size of the same order of the original object, while high energies produce the so-called shattering regime, yielding a full scale-invariant spectrum of fragment sizes [Kun and Herrmann, 1999].

The fragmentation dynamics of snow crystals are likely to be different from those of ice solids, in large part because of the uncertain role played by their geometry. When a snow crystal impacts the surface with sufficient energy, crack formation is likely to take place at the connections between different branches, where sharp corners yield local stress peaks. Accordingly, a fundamental role is played by the size distribution of surface irregularities. It is known that snow crystals present extremely variable shapes, such as needles, columns, plates, and dendrites, depending on temperature and humidity at the time of formation [Nakaya, 1954]. Because of such fascinating diversity, the development of a fragmentation theory that applies to any crystal type seems prohibitive. Nevertheless, there exists a family of snow crystals that present a common feature, that is, a fractal structure. A typical example are the dendritic crystals, which are commonly observed in nature. It should not surprise, in fact, that one of earliest fractal shapes to have been described is the so-called "Koch's snowflake" [Sugihara and May, 1990]. Numerical and experimental studies were able to identify the fractal dimension γ of dendritic snow crystals, which spans the range 1.9 ~ 2.5 depending on their specific structure [Nittmann and Stanley, 1987, Heymsfield et al., 2010, Chukin et al., 2012, Leinonen and Moisseev, 2015]. We hereafter exploit the fractal properties of dendritic snow crystals to derive a fragmentation theory that links the size distribution of snowflakes to that of blowing-snow particles.

Let us define the box-counting measure $M(\epsilon)$ as the number of boxes of side-length ϵ needed to cover the fractal curve. A relevant property of fractals is the scale invariance of the box-counting measure, i.e. $M(\lambda\epsilon) = \lambda^{-\gamma} M(\epsilon)$ [Weiss, 2001]. Let us then call D the size of the parent crystals and λD the distance between adjacent cracks, with $\lambda \in [0;1]$. Assuming that cracks develop from sharp corners, where small curvatures yield local stress peaks, crystal breaking acts by chipping surface irregularities off the fractal contour. Because the distance between adjacent cracks defines the characteristic size of the fragment, λ is hereafter referred to as the dimensionless fragment size. The fragment size distribution resulting from the complete shattering of the fractal crystal would be perfectly scale-invariant, such that the number $N(\lambda D)$ of fragments with size λD is $\lambda^{-\gamma} N(D)$. Given that we are considering only one parent crystal, we would have $N(D) = 1$ and $N(\lambda D) = \lambda^{-\gamma}$. However, it is sensible to assume that impact energies are generally not large enough to yield a complete shattering, but rather a damage regime characterized by crack formation at a few critical corners. Let us then call $p(\lambda)$ the probability density function describing the likelihood of crack formations at distance λD one from another. The total number of children crystals formed upon impact is therefore

$$N = \int_0^1 N(\lambda D)\,\mathrm{d}\lambda = \int_0^1 \lambda^{-\gamma} p(\lambda)\,\mathrm{d}\lambda. \tag{2.1}$$

Equation 2.1 can be employed to estimate the number of fragments produced upon impact of a dendritic snow crystal, provided some reasonable assumptions on the probability distribution $p(\lambda)$ are made. Even though $p(\lambda)$ is not precisely known, it seems reasonable to assume that cracks develop from the sides of larger branches, which are more protruding and thus more subjected to large bending forces and local stress peaks. If we indicate with Λ the size of the larger branches, this assumption yields $p(\lambda) = \delta(\lambda - \Lambda)$, i.e., a Dirac delta function centered in Λ, such that

$$N = \Lambda^{-\gamma}. \tag{2.2}$$

We perform numerical simulations of snow crystal fragmentation based on the discrete element method (DEM) to evaluate whether equation 2.2 holds for a dendritic snow crystal. Figure 2.1a (ii) shows the simplified snow crystal model, whose geometry mimics that of a real dendritic snowflake (Figure 2.1a (i)), formed of ice elements in contact through cohesive bonds (see also Figure A.1 of appendix A). The mechanical properties of ice are used for the contact model [Gaume et al., 2015], yielding realistic deformations and stress distribution (details about the DEM are provided in appendix A.3). We perform

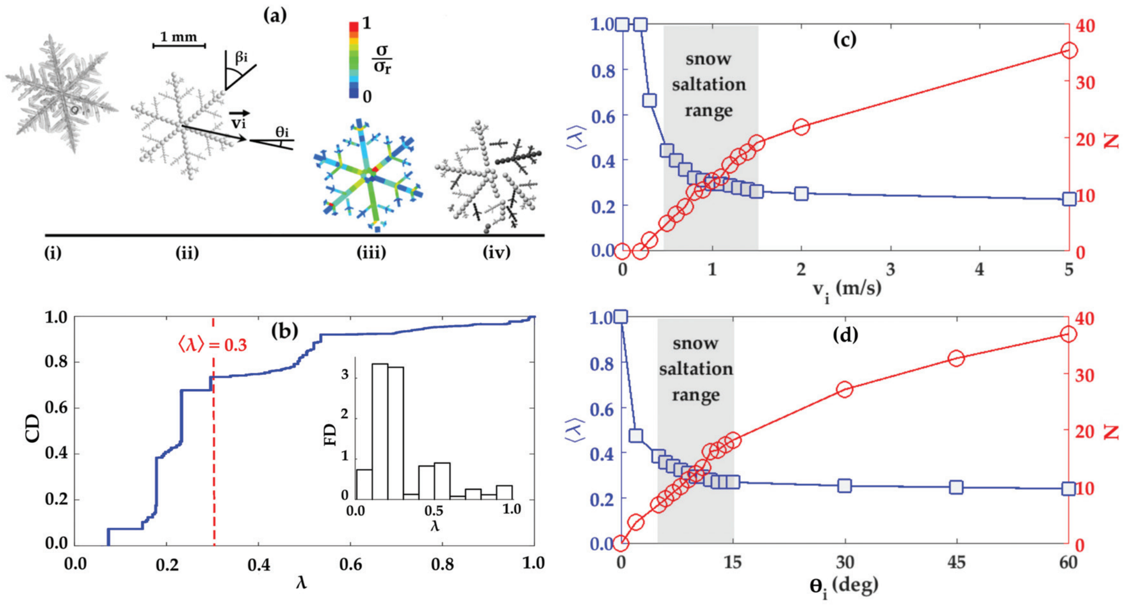

Figure 2.1 – (a) Illustration of the DEM simulations: i) real snowflake (credit: Satoshi Yanagi, http://www1.odn.ne.jp/snow-crystals/page1_E.html), ii) simplified DEM description, iii) ratio between tensile stress σ in bonds and at the moment of the impact and tensile strength of ice σ_r, iv) fragmented snowflake (each level of grey represents a fragment). In the snow crystal model, the radius of the largest elements is 50 µm, while the radius of the smallest ones is 12.5 µm. (b) Cumulative size distribution (CD) of the dimensionless fragment size λ and corresponding frequency distribution (FD). (c) Influence of impact velocity and (d) impact angle on the average dimensionless fragment size $\langle\lambda\rangle$ and number of fragments N. The grey bands identify the ranges of impact velocity and impact angle typical of snow saltation, i.e., $0.5 < v_i < 1.5$ m/s and $5° < \theta_i < 15°$ [Araoka and Maeno, 1981].

impact simulations with a flat surface for different values of impact speed v_i and impact angle θ_i, computing the stress distribution (Figure 2.1a (iii)) and the fragment release (Figure 2.1a (iv)).

Figure 2.1b shows the cumulative distribution (CD) and the frequency distribution (FD, in the inset) of the fragment sizes. We obtain the distributions from averaging the results of 1000 impact simulations, presenting all possible combinations of 10 values of crystal orientation $\beta_i \in [0°, 60°]$ (see Figure 2.1a (ii)), 10 values of impact velocity $v_i \in [0.5, 1.5]$, and 10 values of impact angle $\theta_i \in [5°, 15°]$. The variability ranges of v_i and θ_i are typical of snow saltation [Araoka and Maeno, 1981]. The frequency distribution highlights that the majority of fragments presents $\lambda = 0.2 \sim 0.3$, with a mean value $\langle\lambda\rangle = 0.3$. If we assign $\Lambda = 0.3$ in equation 2.2 it follows that, for a fractal dimension $\gamma = 2.1$ repersentative of dendritic shapes, the number of fragments N is approximately 10.

Figures 2.1c and 2.1d show how $\langle\lambda\rangle$ and N vary with respect to impact velocity v_i and impact angle θ_i. Each value of $\langle\lambda\rangle$ and N is obtained by averaging the results of 10 impact simulations with different crystal orientations β_i. These results suggest that $\langle\lambda\rangle \approx 0.3$ and $N \approx 10$ are reasonable approximations in the range of impact velocities and impact angles typical of snow saltation [Araoka and Maeno, 1981] (we study the sensitivity of our results to these values in section 2.6).

The DEM simulations thus suggest that equation 2.2 provides an effective prediction on the number of fragments produced upon breaking of a dendritic crystal. The results also indicate that crystal rebound does not take place under the tested impact conditions and that deposition only occurs for very low impact velocities ($\langle\lambda\rangle = 1$ and $N = 0$ for $v_i < 0.2$ ms^{-1}, Figure 2.1c), which is consistent with experimental observations [Sato et al., 2008].

2.4 Blowing-snow fragmentation

In light of the observations of section 2.3, we propose a physical description of blowing-snow fragmentation as schematically represented in Figure 2.2. A large dendritic snowflake of size D_0, lifted from the surface through aerodynamic or splash entrainment, follows a ballistic trajectory and eventually impacts the surface producing a number $N = \Lambda^{-\gamma}$ of smaller fragments with size $D_1 = \Lambda D_0$. A fraction $\alpha(D_1)$ of these children crystals moves to the suspension layer transported by turbulent eddies, while the remaining part remains in saltation and eventually impacts the surface generating fragments of size $D_2 = \Lambda D_1$. Given that crystals of size D_2 have a smaller inertia than crystals of size D_1, turbulent motions are more efficient in carrying them in suspension and thus $\alpha(D_2) > \alpha(D_1)$. Following this fragmentation pattern, the number of crystals of size $D_n = \Lambda D_{n-1}$ generated at the n^{th} impact is

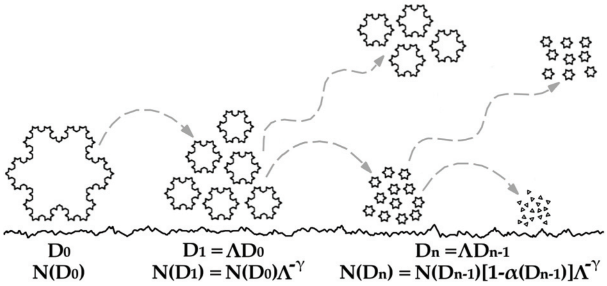
D_0
$N(D_0)$
$D_1 = \Lambda D_0$
$N(D_1) = N(D_0)\Lambda^{-\gamma}$
$D_n = \Lambda D_{n-1}$
$N(D_n) = N(D_{n-1})[1-\alpha(D_{n-1})]\Lambda^{-\gamma}$

Figure 2.2 – Schematic representation of the fragmentation process during saltation. Each crystal impact leads to formation of fragments having size equal to Λ times the original size. The number of children crystals follows from the scale-invariance property. Small fragments, formed after repeated impacts, are likely to be caught by turbulent eddies and transported to the suspension layer.

$$N(D_n) = N(D_{n-1})\,[1 - \alpha(D_{n-1})]\,\Lambda^{-\gamma}. \tag{2.3}$$

An assumption underlying the proposed theory is the scale-invariance of the fragmentation process, that is, children crystals of any size present the same fractal geometry and thus experience the same fragmentation dynamics of their larger parent crystals. The experimental studies by Sato et al. [2008] and our DEM simulations (Figure 2.1) suggest that large crystals are too brittle to rebound without breaking and that deposition occurs in very light wind conditions, i.e., for surface shear stresses significantly below the limit required to initiate snow transport. Accordingly, we assume that crystals of any size experience fragmentation upon impact, neglecting deposition and rebound. In reality, crystal fragments with size of the order of the smallest branches (around 50 μm) present a spheroidal shape rather than a fractal one [Gordon and Taylor, 2009]. Small-scale deviations from the fractal theory are, in fact, typical of all geometries of nature [Brown et al., 2002]. The saltation dynamics of small ice fragments become then similar to those of sand grains, which experience deposition and rebound rather than fragmentation [Kok et al., 2012, Kobayashi, 1972]. Bearing this limitation in mind, we can still regard the assumption of scale-invariance as adequate for the purpose of studying how fragmentation processes transform the snowfall size-distribution, given the significant separation between the size of large snowflakes and the length scale at which the fractal theory is expected to fail.

2.5 Modeling blowing-snow fragmentation

We incorporate the proposed fragmentation process in a statistical-mechanics model of saltation. We cast the particle dynamics in a residence time distribution framework, which has been widely employed in stochastic formulations of water [Botter et al., 2011], contaminant [Benettin et al., 2013b], and heat transport [Comola et al., 2015] in underground formations. Let us define the residence time of a crystal as the time elapsed between the start and the end of its motion in the saltation layer. Crystal motion can start when the crystal is entrained from the surface, through aerodynamic forces or splash, or when the crystal is formed upon fragmentation of a larger crystal. Conversely, the end of motion occurs when the crystal moves to the suspension layer carried by turbulence or when it impacts the surface, producing smaller fragments.

The number $N(D,t)$ $\left(\mathrm{m}^{-2}\right)$ of crystals of size D in saltation at time t can be expressed as the number of crystals whose motion starts at time t' and whose residence time is larger than $t-t'$, for all $t'<t$, i.e.

$$N(D,t)=\int_0^t \left[E(D,t)+F(D,t)\right] P\left(t-t' \mid D\right) \mathrm{d}t'. \tag{2.4}$$

$E(D,t)$ and $F(D,t)$ $\left(\mathrm{m}^{-2}\mathrm{s}^{-1}\right)$ are surface entrainment and fragment production, i.e. the fluxes responsible for initiating crystal motion. $P\left(t-t' \mid D\right)$ is the probability that the residence time of crystals of size D is larger than $t-t'$. We can differentiate equation 2.4 using Leibniz's rule to express the size-resolved mass balance equation (see section A.2 of appendix A for more details)

$$\frac{\mathrm{d}N(D,t)}{\mathrm{d}t}=E(D,t)+F(D,t)-S(D,t)-I(D,t). \tag{2.5}$$

On the right-hand side of equation 2.5, the two sink terms $S(D,t)$ and $I(D,t)$ $\left(\mathrm{m}^{-2}\mathrm{s}^{-1}\right)$ are the suspension flux and the impact rate of crystals of size D at time t. These two terms read

$$S(D,t)=\alpha(D)\int_0^t \left[E\left(D,t'\right)+F\left(D,t'\right)\right] p_S\left(t-t'\right)\mathrm{d}t', \tag{2.6}$$

$$I(D,t)=\left[1-\alpha(D)\right]\int_0^t \left[E\left(D,t'\right)+F\left(D,t'\right)\right] p_I\left(t-t'\right)\mathrm{d}t'. \tag{2.7}$$

$\alpha(D)\in[0;1]$ is the probability that a crystal of size D becomes suspended. Conversely, $1-\alpha(D)$ is the probability that a crystal of size D impacts the surface. Here, we assign to $\alpha(D)$ the expression of the eddy-diffusivity correction for inertial particles with respect to passive tracers [Csanady, 1963], given that the two quantities obey the same limits and are governed by similar physics. In fact, the probability of becoming suspended is equal to 1 in the limit of $D \to 0$, that is, for passive tracers, decreases as the settling velocity becomes relevant compared to turbulent fluctuations, and reaches the lower value 0 in the limit of $D \to \infty$. We therefore write

$$\alpha(D) = \left[1 + \frac{w_s^2(D)}{\sigma^2}\right]^{-\frac{1}{2}}, \tag{2.8}$$

where $w_s(D)$ is the settling velocity of crystals of size D and σ^2 is the turbulence velocity variance (see section A.2 of appendix A for their analytical expressions). Furthermore, $p_S(t-t')$ and $p_I(t-t')$ are the residence-time probability density functions of crystals moving to suspension and impacting the surface, respectively. If we assume that particles move independently from one another, it follows that the dynamics are well described by a Poisson process, yielding for $p_S(t-t')$ and $p_I(t-t')$ exponential residence time distributions.

We assume that the surface entrainment $E(D,t)$, the first source term on the right-hand side of equation 2.5, samples uniformly from the size-distribution of crystals resting at the surface, according to the principle of equal mobility [Willetts, 1998]. Because we aim at establishing a link between the snowfall and blowing-snow size distributions, we assume that the saltation process starts over a post-snowfall surface. We therefore simulate impact and fragmentation of snowfall crystals by applying equation 2.1 to an exponential snowfall size-distribution bounded within 0.75 and 2 mm (dashed black line in Figure A.2 of appendix A), which is typical of precipitation intensities of the order of ~ 0.3 mmh^{-1} [Gunn and Marshall, 1958]. The resulting size-distribution of surface crystals proves similar to that obtained by sieve analysis in very cold conditions [Granberg, 1985] (dashed grey line in Figure A.2 of appendix A).

The second source term in equation 2.5 is the fragment production rate $F(D,t)$, which, following equation 2.1, reads

$$F(D,t) = \int_0^1 I\left(\frac{D}{\lambda}, t\right)\lambda^{-\gamma} p(\lambda)\,\mathrm{d}\lambda. \tag{2.9}$$

If we assume again that $p(\lambda) = \delta(\lambda - \Lambda)$, we obtain $F(D,t) = I(D/\Lambda, t)\,\Lambda^{-\gamma}$.

We solve equation 2.5 numerically, letting the system evolve until a stationary condition is reached. We then compute the size-distribution of blowing-snow by normalizing $N(D,t)$ in stationary conditions.

2.6 Model results

We first perform a model simulation using $\gamma = 2.1$ and $\Lambda = 0.3$, which are representative of the dendritic snow crystal considered in section 2.3. To evaluate the results of our statistical-mechanics model of blowing-snow fragmentation, we analyze all known published datasets of blowing-snow size distributions, collected from field campaigns in the United States [Schmidt, 1982b], Canada [Gordon and Taylor, 2009], French Alps [Nishimura et al., 2014], and Antarctica [Nishimura and Nemoto, 2005] (see section A.4 of appendix A for more details). We only consider size-distribution measurements within the saltation height, which is approximately of the order of 15 cm [Gordon et al., 2009, Nishimura and Nemoto, 2005]. If several saltation measurements are available for the same dataset, we average them to obtain the mean size-distribution. Additionally, we present the blowing-snow size-distribution that we measured in wind tunnel tests. We carried out the experiments over a post-snowfall surface at the Institute for Snow and Avalanche Research (SLF/WSL) in Davos, Switzerland, at 1670 m above sea level [Clifton et al., 2006]. We obtain the blowing-snow size-distribution by averaging three series of measurements within the saltation layer, namely at 10, 17, and 30 mm above the surface.

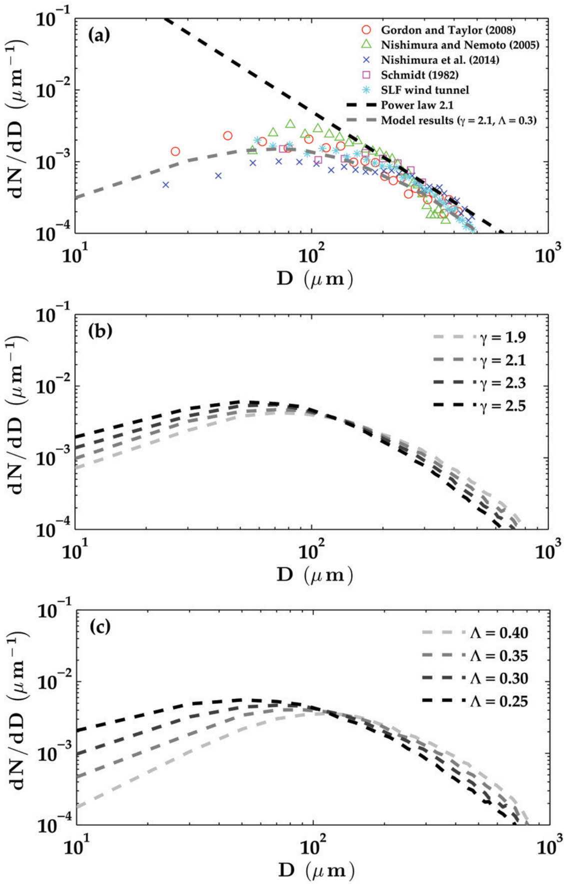

Figure 2.3 – (a) Size-distribution of saltating snow crystals, modeled with the proposed fragmentation theory (dashed grey line), reported in published datasets [Gordon and Taylor, 2009, Nishimura et al., 2014, Nishimura and Nemoto, 2005, Schmidt, 1982b], and measured in the SLF wind tunnel in Davos, Switzerland (colored dots). Because the normalized distributions are sensitive to the specific range of sizes measured by the instruments, we rescaled the distributions such that all of them are tangent to a unique power-law (black dashed line) in the range where they show a scale-invariant behavior (200 ∼ 500 μm). (b) Sensitivity analysis of the modeled blowing-snow size distribution to the fractal dimension γ. (c) Sensitivity analysis of the modeled blowing-snow size distribution to the dimensionless fragment size Λ.

Figure 2.3 shows the size-distribution $\mathrm{d}N/\mathrm{d}D$ as obtained from the fragmentation model (grey dashed line) and dataset analyses (colored dots). The measured size-distributions, which are commonly approximated by a gamma function, are well reproduced by the proposed fragmentation theory. In particular, results highlight that blowing-snow size-distributions display a power-law scaling for the largest crystal sizes ($D > 200$ μm) and a systematic deviation from this self-similar scaling for smaller sizes. Interestingly, the power-law exponent seems to be approximately 2.1, suggesting that the fractal dimension is indeed a control on snow crystal fragmentation. The deviation from the power-law indicates that there exists an under-production of fragments smaller than 200 μm, that is, not all the small branches are chipped off the crystal contour. In fact, as shown in Figure 2.2, the fragmentation process yields small fragments only after multiple impacts, when a significant number of the larger fragments has already moved to suspension with smaller branches still attached. It is worth noting, however, that the small-scale deviation observed in the measured size-distributions may in part be due to the rapid sublimation of the smallest ice fragments [Groot Zwaaftink et al., 2011].

The results thus suggest that a fractal power-law scaling emerges in the size range for which turbulent eddies are not efficiently carrying crystals in suspension (200 – 500 μm). On the contrary, below 200 μm, turbulence starts to be efficient in removing crystals from the saltation layer and reducing the production of smaller fragments. As a result, the peak of the blowing-snow size-distributions lies at ~ 100 μm, where there is the optimal trade-off between the two described mechanisms.

We further perform a sensitivity analysis of the model results to variations in the fractal dimension γ, within the range suggested by measurements, and fragment size Λ, within the range suggested by the DEM simulations. The purpose of this analysis is to test whether variations in the structure of the fractal snow crystal may significantly alter the blowing-snow size distribution. Figures 2.3b and 2.3c suggest that varying γ and Λ produces significant quantitative variations in the results. Despite this quantitative sensitivity, the main qualitative features of the results seem robust relative to reasonable variations in γ and Λ.

2.7 Discussion and conclusions

We proposed a fragmentation theory for snow crystals to test the hypothesis that fragmentation processes constitute the missing link between the seemingly inconsistent size distributions of snowfall and blowing-snow. A key assumption underlying our model is that the fragment size and the fragment number follow from the power-law distribution of surface irregularities typical of fractal geometries. We used discrete element simulations of snow crystal breaking to explicitly test this assumption. These simulations indicated that the theoretical results in terms of fragment size and number is indeed representative of a dendritic snowflake geometry (Figure 2.1). The results of a statistical-mechanics model of saltation, accounting for the proposed fragmentation theory, are consistent with measurements (Figure 2.3a).

Our results suggest that the self-similarity of snow crystals shapes the blowing-snow size-distribution. In particular, our model predicts, and measurements support, a self-similar scaling for crystal sizes larger than 200 μm (Figure 2.3). The deviation from the power-law observed at the lower end of crystal size is due to the relatively large turbulent-diffusivity of particles smaller than 200 μm, which are efficiently transported in suspension and are thus less likely to produce smaller fragments upon impact.

Overall, our analysis suggests that fragmentation processes can indeed transform an exponential snowfall distribution into the so-called gamma distribution of blowing-snow. In particular, the typical features of a gamma distribution emerge, on one side, from the fractal geometry and, on the other side, from the interactions between inertial particles and turbulent eddies.

Further analyses show that these features are conserved for a wide range of fractal dimensions and fragment sizes (Figures 2.3b and 2.3c). This suggests that the proposed fragmentation dynamics may hold for a wide range of dendritic snowflakes. It is worth noting that some commonly observed snow crystals, such as needles and plates, do not present the fractal structure considered in our theory. Figure 2.3a indicates, however, that our model can reproduce several measured size distributions, which may have resulted from fragmentation of snowflakes with different shapes. This suggests that our theory may still provide an effective prediction of the size and number of fragments produced by non-dendritic crystals, although the assumptions on which the theory rests are not supposed to hold for these shapes.

Our work also points toward the need of accurate estimations for the typical time- and length-scale necessary to complete the transition from the size-distribution of snowfall to that of blowing-snow. This would clarify the importance of accounting for fragmentation processes in snow transport models and in climate models, in order to improve the predictions of surface mass and energy balances in snow-covered regions.

2.8 Acknowledgments

I would like to thank all the co-authors for their comments and feedbacks on the submitted paper.

3 Energy- and momentum-conserving model of splash entrainment in sand and snow saltation

An edited version of this chapter was published by AGU. ©2017. *American Geophysical Union.* All Rights Reserved.

Comola, F., and M. Lehning (2017), Energy- and momentum-conserving model of splash entrainment in sand and snow saltation, Geophys. Res. Lett., 44,1-9, doi: 10.1002/2016GL071822.

To view the published open abstract, go to http://dx.doi.org and enter the DOI.

F. C. developed the ejection model, took part in the research design, performed the research, collected literature data, analyzed the data, and contributed to the writing of the paper.

3.1 abstract

Despite being the main sediment entrainment mechanism in aeolian transport, granular splash is still poorly understood. We provide a deeper insight into the dynamics of sand and snow ejection with a stochastic model derived from the energy and momentum conservation laws. Our analysis highlights that the ejection regime of uniform sand is inherently different from that of heterogeneous sand. Moreover, we show that cohesive snow presents a mixed ejection regime, statistically controlled either by energy or momentum conservation depending on the impact velocity. The proposed formulation can provide a solid base for granular splash simulations in saltation models, leading to more reliable assessments of aeolian transport on Earth and Mars.

3.2 Introduction

Saltation of sand-sized granular materials plays a key role in a wide range of environmental processes. Wind-driven sediment transport is responsible for dune and ripple development and erosion of geological features on Earth, Mars, Venus, and Titan [Iversen and White, 1982, Kok et al., 2012]. In alpine terrain, drifting and blowing snow exert strong control on the snow depth distribution [Mott et al., 2010], with relevant implications for hydrology and avalanching [Lehning and Fierz, 2008]. Furthermore, aeolian processes affect the surface mass balance in Antarctica, transporting a significant amount of snow from the ice sheets to the ocean [Scarchilli et al., 2010].

The behavior of granular materials set to motion by aerodynamic forces was the subject of the early work of Bagnold [1941], which laid the basis for Owen's steady-state saltation model [Owen, 1964]. Since then, the study of aeolian transport led to numerical models that embraced the full saltation process [Anderson and Haff, 1988, 1991, McEwan and Willetts, 1991, 1993, Doorschot and Lehning, 2002], generated experimental data sets against which these models were tested [Willetts and Rice, 1986, Shao and Raupach, 1992, Rice et al., 1995, 1996, Guala et al., 2008], and inspired theoretical advances that yet furthered the field [Kok and Renno, 2008, Diplas et al., 2008, Ho et al., 2011, Carneiro et al., 2011, 2013].

It has been long known that the granular splash problem lies at the heart of aeolian saltation physics. After being accelerated by the wind, saltating grains impact the bed at high speed and low angle. The bed at the site of impact consists of grains that may differ in diameter, and that may be glued to one another to differing degrees, by sintering in the case of snow or by menisci of water in the case of sand. The impact energy and momentum are partially retained by the impactor, which typically rebounds from the bed at lower speed and higher angle. The remaining energy and momentum are consumed in the ejection of other grains, typically $1-10$, and in the frictional rearrangement of several other grains near the impact site. Recent studies indicated that splash entrainment is more efficient than aerodynamic forces in lifting grains from the surface, both for sand [Walter et al., 2014] and snow [Paterna et al., 2016]. The control exerted by splash entrainment is even stronger on Mars, where the lower gravity and air density allow grains to follow higher and longer ballistic trajectories, yielding larger impact velocities and thus more ejections per impact [Parteli and Herrmann, 2007, Almeida et al., 2008, Kok, 2010]. This granular splash problem is highly stochastic, as it depends upon the size and velocity of the impacting grain, the size distribution in the granular bed, and the cohesion among grains near the impact site. One of the main challenges in the development of comprehensive aeolian saltation models is to arrive at a statistical representation of the splash process that accounts for all these relevant factors.

Here, we attempt such a representation starting from fundamental conservation laws. The proposed formulation allows us to predict the number of ejections upon impact of a grain with given size and velocity. The model accounts for size distribution and cohesion of surface grains, such that it can be adapted to study the ejection regime of a wide range of granular materials. We employ the model to address long-standing problems related to aeolian transport. In particular, while the momentum balance proves statistically more restrictive than the energy balance in terms of the number of ejections from a loose granular bed [Kok and Renno, 2009], the opposite may be true for cohesive particles. Moreover, previous studies by Anderson and Bunas [1993] suggest that the multi-grain size problem in splash entrainment lies at the heart of the reverse grading and migration of aeolian ripples. The ejection regimes of heterogeneous sand may in fact be inherently different from that of uniform sand due to the negative correlation between size and velocity of splashed grains. The proposed formulation can provide a solid base for simulations of splash entrainment in saltation models, ultimately leading to improved assessments of aeolian transport processes on Earth and Mars.

3.3 Ejection model

Let us consider the impact of a single particle of mass m_i and velocity v_i with the granular bed. Upon impact, this particle has a probability $P_r \in [0;1]$ of rebounding with velocity v_r. Moreover, a certain number of particles may be ejected from the granular bed. We define the reference system (x, y, z) such that the vertical plane (x, z) contains the impact velocity vector $\vec{v}_i$ (see Figure 3.1). Mass, velocity and number of ejected particles are constrained by the energy and momentum conservation laws [Kok and Renno, 2009]. The energy balance equation reads

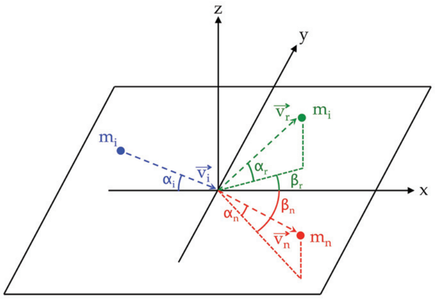

Figure 3.1 – Schematic representation of the impact-ejection dynamics. The impacting particle (blue circle) has mass m_i and velocity v_i. Upon impact, the particle can rebound (green circle) with velocity v_r and eject other particles (red circle) of mass m_n and velocity v_n. The reference system is such that the vertical plane (x,z) contains the impact velocity vector $\vec{v}_i$, which forms an angle α_i with the horizontal plane (x,y). The rebound velocity vector $\vec{v}_r$ forms an angle α_r with the horizontal plane (x,y), and an angle β_r with the vertical plane (x,z). Similarly, the ejection velocity vector $\vec{v}_n$ forms an angle α_n with the horizontal plane (x,y), and an angle β_n with the vertical plane (x,z).

$$\sum_{n=1}^{N}\left(\frac{1}{2}m_n v_n^2+\phi_n\right)=\left(1-P_r\epsilon_r-\epsilon_f\right)\frac{1}{2}m_i v_i^2, \tag{3.1}$$

where N indicates the number of ejections; m_n and v_n are mass and velocity of the n^{th} ejected particle; ϕ_n is the cohesive bond exerted on the n^{th} particle by its neighboring particles; ϵ_r is the fraction of impact energy retained by the rebounding particle, while ϵ_f is the fraction of impact energy lost to the bed.

Because the impact angle α_i is generally small, approximately 10° [Bagnold, 1941], most of the impact momentum is directed along x. The momentum balance equation in this direction reads

$$\sum_{n=1}^{N}\left(m_n v_n \cos\alpha_n \cos\beta_n\right)=\left(1-P_r\mu_r-\mu_f\right)m_i v_i \cos\alpha_i, \tag{3.2}$$

where α_n and β_n are the vertical and horizontal ejection angles of each splashed particle; μ_r is the fraction of impact momentum retained by the rebounding particle in the $x-$direction, while μ_f is the fraction of impact momentum lost to the bed. Cohesive forces do not appear in equation 3.2, as the sum of pairwise equal particle interactions acting in opposite directions always conserves momentum. By dividing both sides of equations 3.1 and 3.2 by N we obtain

$$N=\frac{\left(1-P_r\epsilon_r-\epsilon_f\right)m_i v_i^2}{\dfrac{1}{N}\displaystyle\sum_{n=1}^{N}m_n v_n^2+2\phi}, \tag{3.3}$$

$$N = \frac{\left(1 - P_r \mu_r - \mu_f\right) m_i v_i \cos\alpha_i}{\frac{1}{N}\sum_{n=1}^{N} m_n v_n \cos\alpha_n \cos\beta_n}, \tag{3.4}$$

where we have assumed a mean value of cohesion ϕ for all ejecta. The ejection problem is highly underdetermined, presenting just two equations and $2N+1$ unknowns, namely N values of mass, N values of velocity, and the number of ejections N. Nevertheless, we may seek a solution by approximating the arithmetic means in equations 3.3 and 3.4 with the corresponding ensemble means $\langle m v^2\rangle$ and $\langle m v \cos\alpha \cos\beta\rangle$, which are equivalent to the arithmetic means in the limit $N \to \infty$. This approximation, in fact, allows us to exploit our knowledge of the probability distributions of ejecta's mass and velocity to solve the ejection problem. We therefore write

$$N_E = \frac{\left(1 - P_r \epsilon_r - \epsilon_f\right) m_i v_i^2}{\langle m v^2\rangle + 2\phi}, \tag{3.5}$$

$$N_M = \frac{\left(1 - P_r \mu_r - \mu_f\right) m_i v_i \cos\alpha_i}{\langle m v \cos\alpha \cos\beta\rangle}. \tag{3.6}$$

N_E and N_M are the number of ejections predicted by the energy and momentum balance, respectively. Because the approximated energy and momentum balances (equations 3.5 and 3.6) generally yield two different solutions, i.e., $N_E \neq N_M$, a physically sensible ejection function must satisfy $N = \min\left(N_E, N_M\right)$, so that neither energy nor momentum are created [Kok and Renno, 2009, McElwaine et al., 2004].

We further manipulate the mean values in equations 3.5 and 3.6 to account for the negative correlation between ejecta's size and velocity, that is

$$\langle m v^2\rangle = \langle m\rangle\langle v^2\rangle + r_E \sigma_m \sigma_{v^2}, \tag{3.7}$$

$$\langle m v \cos\alpha \cos\beta\rangle = \langle m\rangle\langle v\rangle\langle\cos\alpha\rangle\langle\cos\beta\rangle + r_M \sigma_m \sigma_v, \tag{3.8}$$

where σ_m, σ_v, and σ_{v^2} are the standard deviations of m, v and v^2, respectively; r_E is the correlation coefficient between m and v^2, and r_M is the correlation coefficient between m and v. The physical interpretation of these correlations is that heavier particles are likely to be ejected with smaller velocities due to their larger inertia. The effect of such negative correlations is to reduce the mean values in equations 3.5 and 3.6 and thus increase the total number of ejections necessary to close the energy and momentum balances.

Further manipulation can be carried out by considering well established probability distributions for

m and v. For granular beds, the particle sizes normally follow a lognormal distribution [Kolmogorov, 1941a, Colbeck, 1986, Barndorff-Nielsen, 1986]. Moreover, the ejection velocity is usually well described by an exponential distribution [Anderson and Haff, 1988, 1991, Mitha et al., 1986, Beladjine et al., 2007]. Denoting with $\langle d\rangle$ and σ_d the mean and standard deviation of the ejecta's diameter, we obtain

$$N_E = \frac{\left(1 - P_r\epsilon_r - \epsilon_f\right) d_i^3 v_i^2}{2\langle v\rangle^2 \left(\langle d\rangle + \dfrac{\sigma_d^2}{\langle d\rangle}\right)^3 \left(1 + r_E\sqrt{5\left[1+\left(\dfrac{\sigma_d}{\langle d\rangle}\right)^2\right]^9 - 5}\right) + 2\phi}, \tag{3.9}$$

$$N_M = \frac{\left(1 - P_r\mu_r - \mu_f\right) d_i^3 v_i \cos\alpha_i}{\langle v\rangle \left(\langle d\rangle + \dfrac{\sigma_d^2}{\langle d\rangle}\right)^3 \left(\langle\cos\alpha\rangle\langle\cos\beta\rangle + r_M\sqrt{\left[1+\left(\dfrac{\sigma_d}{\langle d\rangle}\right)^2\right]^9 - 1}\right)}, \tag{3.10}$$

where d_i is the impacting grain's diameter (we provide additional details on the derivation of equations 3.9 and 3.10 in section 1 of the supplemental materials). Equations 3.9 and 3.10 allow us to estimate the number of ejections upon impact of a grain of size d_i at velocity v_i. The novelty of the proposed approach stems from the possibility of accounting for the full spectrum of particle sizes, cohesion, and the negative correlation between ejection size and velocity, which has been observed experimentally and is likely to occur in natural saltation. We can thus employ equations 3.9 and 3.10 to simulate the ejection process of a wide range of granular materials, both loose and cohesive. In particular, we apply our model to investigate the ejection regime of sand and snow, relying on the extensive literature data to assign well established values to the model parameters.

The model formulation depends on a series of parameters, which we assign based on literature data. We summarize in Table 3.1 the model parameters, their range of variation estimated from published literature, and the value assumed in our simulations. In section 2 of the supplemental materials we provide additional details on the model parameters and the mathematical formulations of P_r and $\langle v\rangle$, which are commonly expressed as functions of the impact velocity v_i [Anderson and Haff, 1988, Kok et al., 2012]. Furthermore, in section 3 of the supplemental materials, we show that the model is robust to variations of ±20% in the model parameters.

3.4 Sand ejection

We first investigate the ejection regime of uniform sand, assigning $d_i = \langle d\rangle = 1$ mm, $\sigma_d = 0$ mm and $\phi = 0$ J to be consistent with the experimental conditions of previous studies [Werner, 1987, Anderson and Haff, 1988]. It is worth noting that $\sigma_d = 0$ in equations 3.9 and 3.10 implies that the correlation coefficients r_E and r_M do not play a role. We study the mean ejection regime with the Monte Carlo method, to account for the variability in impact velocity and impact direction. Specifically, for increasing values of impact velocity v_i, we carry out stochastic sampling of the impact angle α_i, calculating the number of ejecta with equations 3.9 and 3.10 (see section 4 of the supplemental materials for additional details on the Monte Carlo procedure). We then average the values of N_E and N_M resulting from each simulation to provide the mean ejection numbers $\langle N_E\rangle$ and $\langle N_M\rangle$.

Table 3.1 – Model parameters. $^{(*)}$ Estimates of the correlation coefficients are only available for sand (values $r_E = r_M = 0$ are assumed for snow). $^{(**)}$ Estimates of cohesion apply only to snow (a value $\phi = 0$ J is used for loose sand). Equations B.11 and B.12 are given in the supplemental materials. NA means not applicable.

Parameter	Range in literature	Value used in the model	Relevant literature
ϵ_r	0.25 – 0.36	0.30	Rice et al. [1995], Araoka and Maeno [1981], Nalpanis et al. [1993], and Nishimura and Hunt [2000]
ϵ_f	0.61 – 0.72	0.67	Ammi et al. [2009]
μ_r	0.44 – 0.54	0.50	Rice et al. [1995] and Nishimura and Hunt [2000]
μ_f	0.37 – 0.44	0.40	Rice et al. [1995]
$r_E{}^*$	Unclear	−0.30	Rice et al. [1995]
$r_M{}^*$	Unclear	−0.40	Rice et al. [1995]
ϕ^{**}	$10^{-10} - 10^{-8}$	10^{-10}, 10^{-9}, 10^{-8}	Gauer [2001] and Zwaaftink et al. [2014]
$\langle \cos\alpha \rangle$	0.76 – 0.83	0.80	Willetts and Rice [1986], Willetts and Rice [1989], Rice et al. [1995], Rice et al. [1996], Nalpanis et al. [1993], Nishimura and Hunt [2000]
$\langle \cos\beta \rangle$	0.41 – 0.97	0.97	Ammi et al. [2009] and Xing and He [2013]
P_r	NA	Function of v_i (equation B.11)	Anderson and Haff [1991] and Andreotti [2004]
$\langle v \rangle$	NA	Function of v_i (equation B.12)	Kok and Renno [2009] and Kok et al. [2012]

Figure 3.2 shows the trends of $\langle N_E \rangle$ and $\langle N_M \rangle$ in the range of impact velocity typical of natural saltation. The results indicate that the momentum balance is statistically more restrictive than the energy balance in terms of mean number of ejections. Momentum balance is therefore what is expected to control the number of ejections in uniform sand saltation, as was observed in a previous analysis [Kok and Renno, 2009]. Moreover, the momentum-conserving solution shows a linear increase of $\langle N \rangle$ with impact velocity, which is consistent with several previous studies [Werner, 1990, McEwan and Willetts, 1991]. The shaded areas in Figure 3.2 correspond to the mean error introduced by solving equations 3.5 and 3.6 in place of equations 3.3 and 3.4, which we solve by sequential sampling of ejected particles until we reach the balances of energy and momentum. In principle, the error introduced when replacing arithmetic means with ensemble means is larger for small values of N, i.e., when the impact velocity is small. Under the same circumstances, however, both the ensemble and the arithmetic means are close to zero due to the small ejection velocity, thus balancing the mean error across the whole range of N. Figure 3.3a shows the momentum- and energy-conserving solution $\langle N \rangle = \min(\langle N_E \rangle, \langle N_M \rangle)$ for uniform sand (magenta line), which proves consistent with previous experimental and numerical data [Werner, 1987, Anderson and Haff, 1988] (black markers) as well as with state-of-the-art parameterizations for

sand ejections (black line) [Kok and Renno, 2009].

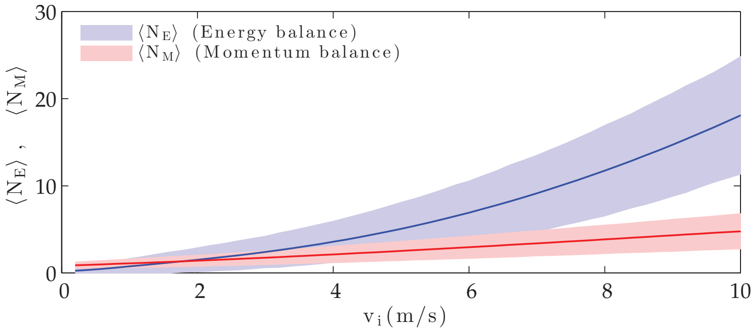

Figure 3.2 – Mean number of ejections as predicted by equations 3.9 (blue line) and 3.10 (red line) for uniform sand with $\langle d\rangle = 1$ mm, $\sigma_d = 0$ mm and $\phi = 0$ J. The shadowed bands represent the errors introduced with respect to the exact energy and momentum balance equations 3.3 and 3.4.

We further apply the model to simulate the ejection regime of heterogeneous sand. To our knowledge, among all experimental investigations carried out with heterogeneous sand, only Rice et al. [1995] successfully measured the ejection velocity of grains of different size, highlighting the existence of negative correlations. Accounting for all the experimental tests reported in Rice et al. [1995], we estimate overall correlation coefficients $r_E \approx -0.3$ and $r_M \approx -0.4$. To reproduce the experimental conditions, we assign $\langle d\rangle = 250$ µm and $\sigma_d = 50$ µm. The granular splash resulting from a heterogeneous bed differs greatly depending upon the size of the impactor. To handle both the role of the sorting at the site of the impact and the size of the impactor, we carry out a series of Monte Carlo simulations similar to those performed for uniform sand, but with the additional random sampling of the impact diameter. In particular, we sample d_i from the log-normal distribution of ejected grains, truncated within 70 and 500 µm, accounting for the fact that smaller grains are mostly in suspension and larger ones in reptation [Shao, 2008]. Figure 3.3b shows that the mean number of ejections obtained with $r_E = -0.3$ and $r_M = -0.4$ (solid magenta line) deviates significantly from that obtained with $r_E = r_M = 0.0$ (dashed magenta line), leading to a more accurate prediction of the experimental data for heterogeneous sand. Existing ejection models [Kok and Renno, 2009] (dashed black line) that do not account for such negative correlations fail to capture the larger ejection numbers measured for heterogeneous sand.

3.5 Snow ejection

We consider typical snow properties by assigning $\langle d\rangle = 200$ µm and $\sigma_d = 100$ µm. Because the correlation between mass and velocity of ejected snow has never been experimentally quantified, we focus the analysis only on the effect of cohesion and assign $r_E = r_M = 0$ for simplicity. Previous energy conserving models of snow ejection [Gauer, 2001, Zwaaftink et al., 2014] suggest that ϕ may span the range $10^{-10} - 10^{-8}$ J, depending on sintering among ice grains. We carry out Monte Carlo simulations following the same random sampling procedure adopted for the heterogeneous sand case. Figure 3.4a shows the variation of $\langle N_E\rangle$ for three different values of cohesion. For $\phi = 10^{-10}$ J, there is a threshold value of impact velocity dividing a lower range in which the ejection regime is limited by the energy balance from an upper range in which the momentum balance is the main control. For $\phi = 10^{-9}$ J the threshold impact velocity increases significantly and for strongly sintered snow, with $\phi = 10^{-8}$ J, the energy balance limits the number of ejections across the whole range of impact velocity. These results confirm and extend previous observations [Dietrich, 1977] suggesting that the impact energy exerts a

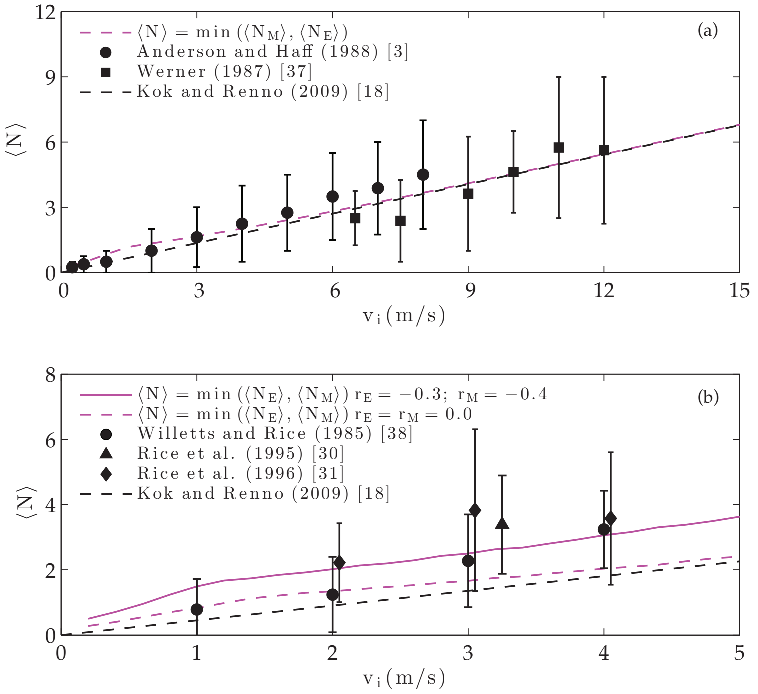

Figure 3.3 – (a) Predicted number of ejections (magenta line) for uniform sand with $\langle d \rangle = 1$ mm, $\sigma_d = 0$ mm. Black squares refer to wind-tunnel tests performed with uniform sand of size 800 µm [Werner, 1987]. Black circles refer to numerical simulations of uniform sand of size 1 mm [Anderson and Haff, 1988]. Vertical bars indicate standard deviations. The dashed black line is the ejection function of the COMSALT model [Kok and Renno, 2009]. (b) Predicted number of ejections for heterogeneous sand with $\langle d \rangle = 250$ µm, $\sigma_d = 50$ µm, including (solid magenta line) and neglecting (dashed magenta line) the negative correlation between ejecta's mass and velocity. The black markers refer to wind-tunnel studies carried out with a mixture of fine (150 – 250 µm), medium (250 – 355 µm) and coarse (355 – 600 µm) sand fractions [Willetts and Rice, 1985, Rice et al., 1996, 1995]. Vertical bars indicate standard deviations. Results of the COMSALT model (dashed black line) are shown as reference simulation of uniform sand ejection. Experiments [Oger et al., 2005, Beladjine et al., 2007, Ammi et al., 2009, Mitha et al., 1986] and models [Crassous et al., 2007] from sediments other than sand are omitted because different sphericity, elasticity and friction coefficients are likely to produce different ejection regimes.

major control on ejection of cohesive materials. As suggested by equations 3.9 and 3.10, cohesion acts as a sink of impact energy but not of impact momentum, such that energy conservation becomes the principal constraint to granular splash of highly cohesive materials.

Figure 3.4b shows the predicted number of ejections $\langle N \rangle = \min(\langle N_E \rangle, \langle N_M \rangle)$ for the three tested values of ϕ together with experimental data on snow [Sugiura and Maeno, 2000] and ice particle ejection [Kosugi et al., 1995]. The snow ejection measurements, carried out with both fresh and compact snow cover, lie close to the curve corresponding to $\phi = 10^{-10}$ J, while the data points obtained for densely packed ice particles lie close to the curve corresponding to $\phi = 10^{-8}$ J. The empirical ejection function obtained by fitting a power-law to the compact snow data (dashed black line) [Sugiura and Maeno, 2000], commonly adopted in snow transport models, significantly deviates from the momentum conserving solution for large values of impact velocities.

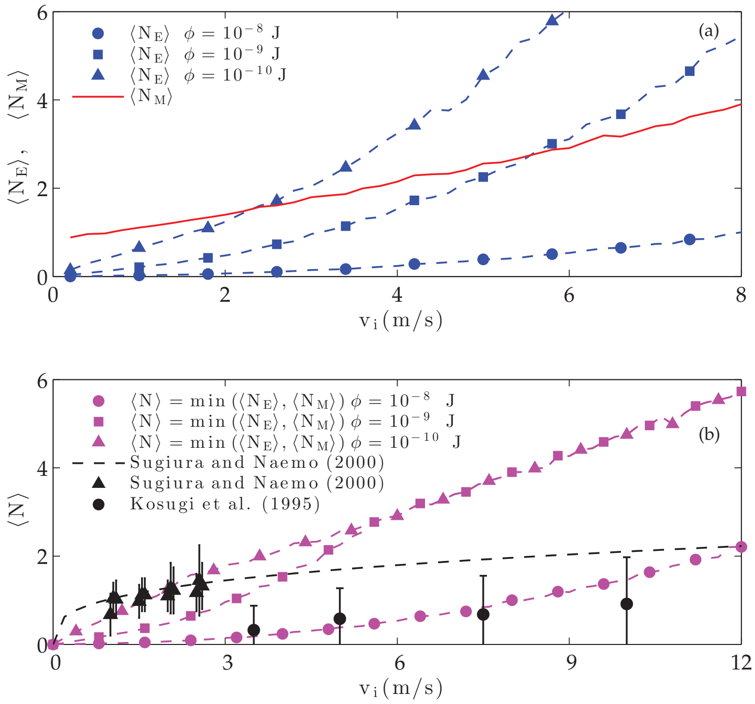

Figure 3.4 – (a) Number of snow ejections predicted by the momentum balance equation 3.10 (red line) and by the energy balance equation 3.9, for different values of cohesion ϕ (blue lines). Snow size distribution parameters are $\langle d \rangle = 200$ µm, $\sigma_d = 100$ µm. (b) Predicted number of snow ejections (magenta lines) resulting from the lower envelopes of the red and blue lines in Figure 3.4a. Black triangles refer to wind-tunnel studies on ejection of both fresh and compact snow [Sugiura and Maeno, 2000]. Black circles refer to ejection experiments carried out with densely packed ice particles and for impact angles between 5° and 15°, typical of saltation [Kosugi et al., 1995]. Vertical bars indicate standard deviations. The dashed black line refers to the empirical ejection function obtained by fitting a power-law to the compact snow data [Sugiura and Maeno, 2000].

3.6 Conclusions

In aeolian saltation, wind-blown grains follow ballistic trajectories close to the surface and frequently impact the granular bed to generate what is called the granular splash. Surface grains may be loose, as in the case of dry sand, or bound to one another, by sintering in the case of snow or by water menisci in the case of wet sand. The impacting grain typically rebounds from the bed, retaining part of the impact energy and momentum. The remaining energy and momentum drive the frictional rearrangement of several grains near the impact site and the ejection of other grains, which is the most efficient entrainment mechanism in aeolian transport on Earth and Mars.

Our proposed ejection model provides a deeper insight into sediment transport. Our results confirm that momentum balance is the main control on loose sand ejection and that the number of ejecta per impact scales linearly with the impact velocity (Figure 3.2). We also show that the relatively larger ejection rate observed in experiments carried out with heterogeneous sand is successfully explained by our theory that includes a negative correlation between size and velocity of ejected grains (Figure 3.3). The correlation coefficients estimated from experimental results by Rice et al. [1995] yield a good match between modeled and measured number of ejections. This suggests that the ejection regime of heterogeneous sand is inherently different from that of uniform sand, for which the correlations do not play a role because $\sigma_d = 0$ (see equations 3.9 and 3.10). In fact, when negative correlation coefficients are considered, the predicted number of ejection is almost twice as large as that obtained for uniform sand. Such a larger ejection efficiency is likely to influence the self-balanced transfer of momentum among fluid and saltating particles, leading to a larger separation between the wind speed required for aerodynamic entrainment and that required for continuation of transport.

Our model simulations of snow ejection highlight that cohesion produces a mixed ejection regime, statistically controlled by energy conservation below a threshold impact velocity and by momentum conservation above it (Figure 3.4). We observe that the threshold impact velocity increases with increasing cohesion. Our model suggests that the reason for such behavior lies in the effect of cohesion, as the breaking of bonds in the substrate dissipates impact energy but does not affect momentum conservation. However, the general, yet not well supported, opinion that energy conservation is the sole control on snow ejection may be a misconception, as there exists a large range of cohesion values for which momentum conservation controls ejection at high impact velocity.

Saltation models commonly track the trajectories of wind-blown particles, explicitly solving for their size d_i and velocity v_i upon impact with the granular bed [Nemoto and Nishimura, 2004, Vinkovic et al., 2006, Kok and Renno, 2009, Dupont et al., 2013, Zwaaftink et al., 2014]. Accordingly, these models may directly benefit from the proposed splash function, ultimately leading to improved simulations of larger scale processes such as saltation intermittency and both ripple and dune development. Our results also point toward future needs in terms of experimental work for more precise quantifications of the model parameters, in particular concerning the dependence of snow cohesive properties on temperature and relative humidity.

3.7 Acknowledgements

I would like to thank all the co-authors for their comments and feedbacks on the submitted paper. The authors of the paper thank Jasper F. Kok, Henning Löwe, Johan Gaume, and Christine Groot Zwaaftink for insightful discussions.

4 Large eddy simulations of drifting and blowing snow in mountain terrain

An edited version of this chapter will be submitted for publication.

Comola, F., M. G. Giometto, M. B. Parlange, and M. Lehning (2016), Large eddy simulations of drifting and blowing snow in mountain terrain. In preparation.

F. C. implemented the Lagrangian stochastic model in the large eddy simulation model, took part in the research design, performed the research, analyzed the data, and wrote the chapter.

4.1 Abstract

The aeolian transport of snow plays a fundamental role in the surface mass and energy balances of alpine and polar regions. Although recent studies identified the dominant factors controlling initiation and continuation of snow transport over flat surfaces, very little is known on how the process develops over complex terrains. Here, we adopt a comprehensive modeling approach, based on Lagrangian-stochastic modeling of particle dynamics and large-eddy simulations of turbulent flows, to investigate the role of drifting and blowing snow in shaping the snow depth distribution in mountain terrain. In particular, we simulate drifting and blowing snow around a Gaussian hill, assigning the initial snow depth distribution equal to the snowfall deposition pattern obtained from the simulation of chapter 1. We account for the complex series of processes involved in snow transport, namely aerodynamic entrainment, flow-particle interactions, rebound and splash entrainment. Our results suggest that snow erosion is localized on the windward side of the hilltop, where the large surface shear stress drives aerodynamic entrainment. During the saltation process towards the lee side of the hill, particles accelerate and splash a relevant amount of grains from the surface. We estimate that splash entrainment is, in fact, significantly more efficient than aerodynamic entrainment in lifting grains from the surface. When particles reach the leeward side of the hill, the reduced wind velocity is not able to sustain the drifting process, such that the larger particles deposit and the smaller ones are caught by turbulent eddies and transported in suspension. As a result, a significant deposition peak forms on the leeward side of the summit and a plume of blowing snow diffuses in the wake region. Moreover, we observe that a significant amount of suspended snow deposits at the toe of the leeward slope, due to the flow recirculation behind the ridge. Overall, the final snow depth distribution radically changes with respect to the initial snowfall deposition pattern, suggesting the importance of accounting for both

precipitation and wind measurements in hydrological models at hillslope scale.

4.2 Introduction

The aeolian transport of granular materials, such as sand and snow, is responsible for a wide range of environmental processes in cold and arid regions [Kok et al., 2012, Pomeroy and Gray, 1990]. Snow transport, in particular, has received considerable scientific attention owing to the important role it plays in the mass and energy balances over Antarctic ice sheets [Scarchilli et al., 2010], as well as for avalanche danger [Lehning and Fierz, 2008], hydrology [Lehning et al., 2006], and water resources management in alpine regions [Finger et al., 2012].

Experimental studies [Nalpanis et al., 1993] suggest that snow saltation has very similar dynamics to sand saltation. The wind-driven erosion of sand grains was initially studied by Bagnold [1941] who observed that, when wind shear stress at the surface exceeds the so-called fluid threshold, some grains are lifted by aerodynamic entrainment. These grains are accelerated by the wind and follow ballistic trajectories in the so-called saltation layer. Upon impact with the surface, particles may either deposit or rebound, depending on their momentum. Furthermore, a fraction of the grain's energy and momentum is transferred to the snow bed, possibly driving the ejection of other particles. The particle concentration in the saltation layer increases until a relevant part of wind momentum is extracted and an equilibrium state is reached. Numerical studies by Carneiro et al. [2011] suggest that aerodynamic entrainment is the main driver of aeolian transport at the onset of saltation, while in steady-state saltation the impact-ejection dynamics, the so-called splash entrainment [Comola and Lehning, 2017], are more efficient in lifting grains from the surface [Paterna et al., 2016]. Moreover, recent wind tunnel studies [Paterna et al., in review] indicate that snow transport may occur in two distinct regimes, namely weak and strong saltation, dominated by aerodynamic and splash entrainment, respectively. In weak saltation, the turbulent flow and the mass flux are strongly coupled, while in strong saltation, snow transport develops its own temporal and spatial scales. Numerical studies further suggest that saltation dynamics might be significantly affected by midair particle collisions [Carneiro et al., 2013] and by the electrostatic forces that arise as a result these collisions [Schmidt et al., 1999, Kok and Renno, 2008].

If snow particles gain enough momentum to reach a considerable height, they might be caught by turbulent eddies and transported in suspension for long distances. These blowing-snow particles experience sublimation processes [MacDonald et al., 2010] that may account for a significant loss of mass. The trajectories of suspended snow particles are controlled by the aerodynamic forces exerted by the turbulent flow. Numerical studies have shown that the complex shapes of snow crystals may significantly affect the flow-particle interactions and therefore the height of the suspension layer [Huang et al., 2011]. Field measurements [Gordon and Taylor, 2009], however, suggest that blowing-snow particles generally present a spheroidal shape as a result of the fragmentation processes that occur along with saltation [Comola et al., in review].

State-of-the-art models of aeolian transport [Kok and Renno, 2009, Zwaaftink et al., 2014, Nemoto and Nishimura, 2004] simulate the Lagrangian trajectories of particles in saltation and suspension. In particular, large eddy simulations (LES) [Pope, 2001] in combination with Lagrangian stochastic models (LSM) [Thomson, 1987] provide an effective modeling framework for accurate simulations of turbulence-particles interactions [Nemoto and Nishimura, 2004]. Recent LES-LSM models have been successfully employed to simulate snow transport [Zwaaftink et al., 2014], sand transport [Vinkovic et al., 2006], and saltation intermittency [Dupont et al., 2013] over flat erodible surfaces.

To our knowledge, LES-LSM simulations of aeolian transport over complex terrains have not been attempted so far. A better insight into the process of sediment erosion over complex surfaces may improve quantifications of small scale surface processes in alpine terrain. Mott et al. [2010] observed, in fact, that drifting snow plays a key role in shaping small scale surface patterns, such as dunes and cornices.

In this chapter, we aim at investigating the influence of drifting and blowing snow on the snow depth distribution at hillslope scale. We propose a comprehensive LES-LSM model with an immersed boundary method (IBM) to account for the form drag exerted by the topography on the surrounding flow. The model set-up is similar to that used in chapter 1 to simulate snowfall deposition. Here, we extend the model implementation to include saltation processes such as aerodynamic entrainment, particle rebound, and splash entrainment. We apply the model to study the aeolian transport of snow over the Gaussian ridge introduced in chapter 1, assigning the initial snow depth distribution based on the snowfall deposition pattern resulting from the previous simulation. The relevance of our work lies in the novel modeling approach that includes the effect of topography on aeolian transport and in the new insights on the relative contribution of snowfall and drifting snow to the distribution of snow depth in complex terrains.

In section 4.3 we summarize the different components of the LES-LSM model and describe the parameterizations used to simulate saltation processes. In section 4.4 we present the model results on drifting and blowing snow around a ridge. Discussion and conclusions close the chapter.

4.3 Methods

4.3.1 Modeling technique

In the following, we summarize the main model components, namely the LES, IBM, and LSM, which were discussed in more detail in chapter 1. The LES technique solves the filtered isothermal Navier-Stokes equations (equations 1.1) [Orszag and Pao, 1975], adopting a static Smagorinsky closure model (equation 1.2) for the sub-grid scale (SGS) stress tensor. This allows us to solve for the energy-containing scales of motions $\tilde{\mathbf{u}}$ and pressure $\tilde{p}$, relying on the SGS model to account for the small scale motions responsible for energy dissipation. Accordingly, the filter size should belong to the inertial subrange.

We solve the filtered Navier-Stokes equations on a regular domain, using a pseudo spectral collocation approach in the horizontal directions and a second-order accurate centered finite differences scheme in the vertical direction. We perform the time integration adopting a fully explicit second-order accurate Adams-Bashforth scheme and employ a fractional step method to compute the pressure field. We apply free-lid conditions at the upper boundary (equations 1.1c), a no-slip boundary condition at the surface (equation 1.1d), and periodic conditions at the lateral boundaries due to the Fourier expansions used in the pseudo spectral approach. This implementation of the LES model has been used in several previous studies [Meneveau et al., 1996, Albertson and Parlange, 1999, Porté-Agel et al., 2000, Bou-Zeid et al., 2005, Sharma et al., 2016].

Because of the complex topography, the surface exerts both a form drag and a shear stress on the LES flow field [Giometto et al., 2016]. We account for the form drag of the resolved topographic scales through the IBM, and compute the shear stress at the surface with a law of the wall in the normal direction to the surface (equation 1.1e). The IBM represents the complex topography as the zero level-set of a signed distance function $\tilde{\phi}(x, y, z)$, such that the computational domain is partitioned in two regions, i.e., the below-surface region Ω_s where $\tilde{\phi}(x,y,z) < 0$, and the above-surface region Ω_f where $\tilde{\phi}(x,y,z) > 0$. We fix the velocity field to zero in the inside region Ω_s through a penalty method and enforce the law of the wall (equation 1.1e) in all the grid nodes that fall in the region $-1.1\Delta < \tilde{\phi}(x,y,z) < 1.1\Delta$. It is worth noting that we do not simulate the evolution of the surface topography as a result of the erosion and deposition processes. Although such variations may produce significant modifications on the flow field in the long term, it is reasonable to neglect them at the time scales considered in this study. Furthermore, this version of the model does not include blowing-snow sublimation. Although this process may play an important role in the overall mass balance of the snow surface, it mostly affects particles in suspension and is thus not likely to produce visible effects on the snow depth distribution.

We use the LSM component to compute the Lagrangian trajectories of inertial snow particles, which move under the effect of drag forces and gravity (equation 1.6). We compute the drag forces assuming that drifting snow particles are sufficiently rounded to be represented as spheres, in which case the drag coefficient has the expression given in equation 1.7. In the computation of the drag force, the relative velocity vector between flow and particle is computed as $\mathbf{u}_r = \tilde{\mathbf{u}} + \mathbf{u}^{SGS} - \mathbf{u}_p$, where $\mathbf{u}^{SGS}$ is the SGS component of the flow velocity and $\mathbf{u}_p$ is the particle velocity. The computation of $\mathbf{u}^{SGS}$ is based on the Langevin equation proposed by Thomson [1987] (equation 1.3), where the deterministic drift term follos from the well-mixed assumption and the stochastic dispersion term follows from the expression of the second order velocity structure function in the inertial subrange. We also include a correction term to account for the reduced autocorrelation time scale of the SGS velocity when following heavy particle trajectories instead of fluid parcel trajectories (equation 1.4), as suggested by Wilson [2000]. We then compute the forcing term $\tilde{\mathbf{f}}^p$ in the filtered Navier-Stokes equations as the sum of the drag forces exerted by the inertial particles on the flow. Although previous studies suggested that inter-particle collisions may affect small scale saltation dynamics [Carneiro et al., 2013], we assume that such effects can be neglected for the purpose of studying the erosion and deposition pattern at the spatial scales of our interest.

4.3.2 Parameterization of surface processes

At the onset of snow saltation, surface particles are lifted from the surface through aerodynamic entrainment, which occurs when the norm of the surface shear stress $|\tilde{\mathbf{t}}|$ (equation 1.1e) exceeds the so-called fluid threshold t_f. According to Bagnold [1941], the fluid threshold can be expressed as

$$\mathrm{t}_f = A^2 g \langle d_p \rangle \left(\rho_p - \rho\right), \tag{4.1}$$

where g is the acceleration of gravity, $\langle d_p \rangle$ is the mean particle diameter, ρ_p is the particle density, and ρ is the air density. We assume a coefficient $A = 0.2$, which was shown to be representative of cohesive snow beds [Clifton et al., 2006]. The number of aerodynamically entrained particles per unit area and unit time n_a is then proportional to the excess of surface shear stress with respect to the fluid threshold [Anderson and Haff, 1991], i.e.

$$n_a = \frac{C_e}{8\pi \langle d_p \rangle^2} \left(|\tilde{\mathbf{t}}| - \mathrm{t}_f\right). \tag{4.2}$$

Doorschot and Lehning [2002] adopted a value of $C_e = 1.5$, but also observed that the value of this proportionality coefficient is largely uncertain due to the lack of experimental evidence. Nevertheless, the snow transport simulations of Zwaaftink et al. [2014], which also assumed a value $C_e = 1.5$, yielded good estimations of measured saltation mass fluxes, suggesting that such value of the proportionality coefficient may be an acceptable approximation.

Denoting with $\Delta\Gamma_s$ the resolution of the discretized surface and with Δt the computational time step, the number of particles entrained at a certain time step in a certain grid node reads $N_a = n_a \Delta\Gamma_s \Delta t$. We then combine these particles into a single parcel, for which we then solve the trajectory. It is noteworthy that the aerodynamic entrainment of particles evolves in time and space according to the excess shear stress.

We sample the particle diameter from a lognormal distribution of mean $\langle d_p \rangle$ and standard deviation σ_d. For the initial parcel velocity we assume a lognormal distribution that varies as a function of the local friction velocity [Nishimura and Hunt, 2000]. Parcels are initialized at an elevation $h = 4\langle d_p \rangle$ from the surface, which is in the range where experimental measurements of initial particle velocity were made. We sample the vertical entrainment angle α_a from a lognormal distribution that varies as a function of the particle size [Clifton and Lehning, 2008]. Because the probability distribution of the horizontal entrainment angle β_a has, to our knowledge, never been studied, we assume that the parcel is entrained along the direction of the local wind velocity, i.e., $\beta_a = \arctan(\tilde{u}_2 / \tilde{u}_1)$.

Upon impact of a particle with the surface, we simulate rebound and splash entrainment (see Figure 3.1 for a schematic representation of these surface processes). We calculate the probability of rebound P_r, which varies as a function of the impact velocity v_i [Anderson and Haff, 1991]. In the computation of the rebound velocity v_r we assume a restitution coefficient $v_r / v_i = 0.5$, according to several previous studies [Anderson and Haff, 1991, Shao and Li, 1999]. We sample the vertical rebound angle α_r from an exponential distribution of mean $\langle \alpha_r \rangle = 45°$ [Kok and Renno, 2009]. For simplicity, we assume that the horizontal direction of the impacting parcel does not change after rebound, that is, $\beta_r = \beta_i$.

We model splash entrainment with the energy and momentum conserving ejection function presented in chapter 3 (equations 3.9 and 3.10), which allows us to explicitly account for particle size distribution and cohesion in the computation of the number of ejected grain [Comola and Lehning, 2017]. Splashed parcels are initialized at an elevation of $h = 4\langle d_p \rangle$ from the surface, with initial velocity sampled from an exponential distribution (see Appendix B.3 for additional information). The vertical entrainment angle of splashed particles α_n is described by an exponential distribution of mean value 50° [Kok and Renno, 2009], while the horizontal entrainment angle β_n is sampled from a normal distribution centered on the direction of the impacting grain and with standard deviation 15° [Xing and He, 2013].

It is worth noting that the previous parameterizations for the ejection angles of aerodynamically entrained, rebounding, and splashed parcels are based on experimental studies carried out on flat surfaces. To provide a more comprehensive description of topographic effects on particle trajectories, we express these angles with respect to the local slope of the surface. Zwaaftink et al. [2014] previously tested a similar implementation of the LES-LSM model against wind tunnel data on snow saltation, showing that these surface parameterizations provide reliable time series of snow mass fluxes.

4.4 Results

We present the results of a snow transport simulation around the bi-dimension ridge previously described in chapter 1. To be consistent with our previous snowfall simulations, we adopt the same domain size and spatial resolution. We initialize the snow depth distribution with the preferential deposition pattern obtained from the previous snowfall simulation (Figure 1.6). We assume that the snow size distribution is well described by a lognormal distribution with mean $\langle d_p \rangle = 200$ µm and standard deviation $\sigma_d = 100$ µm, which are typical values for drifting snow particles [Nishimura and Nemoto, 2005]. We assume, in fact, that the transition from the snowflake size distribution to the drifting snow size distribution, discussed in chapter 2, takes place at scales that are relatively small compared to those relevant for variations in snow depth distribution. Because we assume that the erosion process starts shortly after a snowfall event, we consider a weakly sintered bed with cohesion $\phi = 10^{-10}$ J.

Given a snow density $\rho_p = 910$ kg/m^3, the fluid threshold computed with equation 4.1 is $t_f \approx 0.07$ N/m^2. We therefore increase the flow velocity with respect to the snowfall deposition study, such that aerodynamic entrainment starts in the areas where the surface shear stress exceeds the fluid threshold. Figure 4.1 shows the time-average velocity field around the obstacle. We observe that the free stream velocity is approximately three times larger compared to the previous simulation (Figure 1.4) and that the recirculation regions extends for a longer distance beyond the ridge.

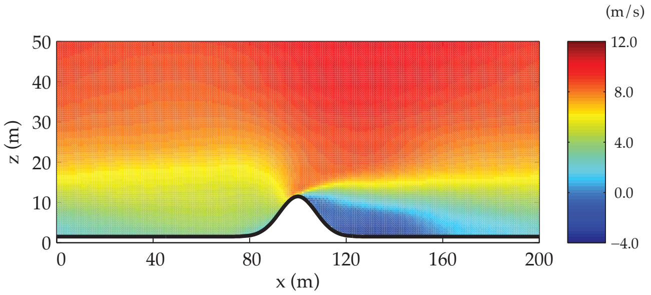

Figure 4.1 – Time-averaged horizontal velocity field around the Gaussian ridge.

From the time-averaged shear stress distribution (Figure 4.2), we can deduce important information on the areas where aerodynamic entrainment is most likely to take place. The topographic effect on the mean stress distribution is remarkable and yields a sharp maximum on the windward side of the hilltop, approximately 5 ~ 6 times larger than the stress on the flat areas upwind and downwind of the hill. We observe that, on average, the surface shear stress overcomes the fluid threshold (red dashed line) only on the windward side of the hill. The maximum values of the time-averaged excess shear stress is approximately 0.05 N/m^2, which corresponds to an aerodynamic entrainment of 0.3 g/m^2/s.

Sporadically aerodynamic entrainment, however, may also occur in areas where the time-averaged shear stress is much below the fluid threshold. We show in Figure 4.3 an instantaneous distribution of surface shear stress, suggesting that snow erosion also takes place upstream of the hill, due the passage of relatively intense turbulence structures.

A snapshot of the instantaneous location of drifting and blowing snow parcels is shown in Figure 4.4. Several parcels are aerodynamically entrained on the windward side of the ridge and drift near the

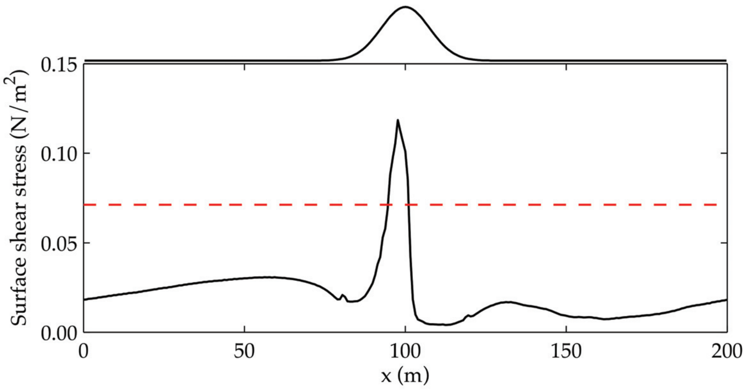

Figure 4.2 – Longitudinal profile of the surface shear stress (averaged in time and along y). The red dashed line indicates the fluid threshold t_f.

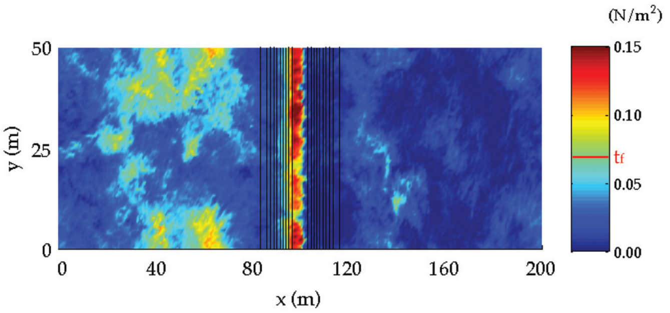

Figure 4.3 – Instantaneous distribution of surface shear stress. The black lines are iso-elevation curves of the Gaussian hill. The red mark on the colorbar indicates the value of fluid threshold, calculated with equation 4.1.

surface towards the lee side. We also observe a significant amount of airborne particles behind the ridge, suspended in the recirculation region. Upon impact of drifting snow parcels with the surface, several other parcels are lifted from the surface through splash entrainment. In order to quantify the relative importance of splash entrainment as opposed to aerodynamic entrainment, we calculate at each time step the number of particles lifted from the surface through each of the two mechanisms and plot the results in Figure 4.5. The results indicate that splash entrainment is significantly more efficient than aerodynamic entrainment in lifting snow from the surface. In fact, splash entrainment exceeds aerodynamic entrainment on average by a factor 4, and reaches up to ~ 10 times higher peak values. The exact values would however need further experimental investigations, due to the uncertainty affecting the proportionality coefficient C_e in the aerodynamic entrainment formulation (equation 4.2).

To provide a more quantitative description of amount and distribution of blowing snow particles in the recirculation region, we compute the time-averaged snow concentration field and show the results in Figure 4.6. We observe large concentration values in proximity of the leeward side of the hilltop. The transition from drifting to blowing snow mostly occurs in this region, which thus acts as a localized source of airborne parcels. Once in suspension, parcels disperse in the recirculation region, such that

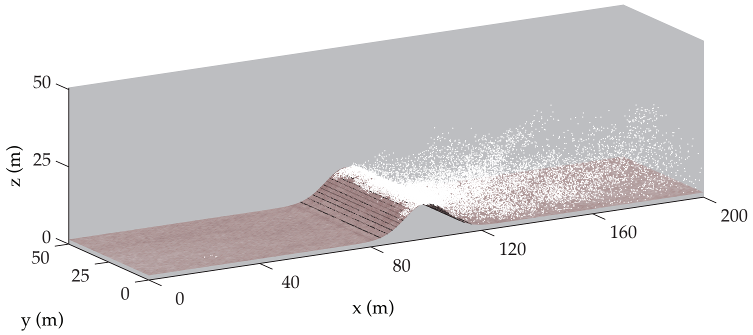

Figure 4.4 – Snapshot of the snow transport process. White dots indicate the position of the snow parcels.

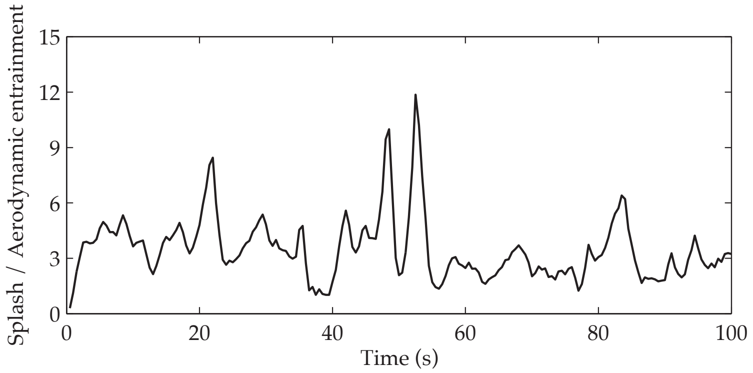

Figure 4.5 – Time evolution of the ratio between splash entrainment and aerodynamic entrainment.

snow concentration progressively decreases with increasing distance from the hilltop.

Figure 4.7 shows the normalized snow deposition profiles, calculated with equation 1.9, at the beginning (dashed red line) and at the end (solid black line) of the simulation. We observe a significant difference between the initial and final snow depth profiles. In particular, a relevant amount of snow is eroded from the windward side of the hilltop and transported towards the leeward side. The location of the deposition maximum coincides with the area of high airborne particle concentration (Figure 4.6), suggesting that a relevant fraction of the saltating particles reaching the leeward side of the ridge does not become suspended but rather deposits at the surface.

The factor that controls deposition and suspension of drifting snow the most is particle size. The turbulent flow can only carry the smaller drifting particles in suspension, while large snow grains deposit on the surface. To better understand this process, we compute the particle size distributions of drifting and blowing snow, setting a threshold distance from the surface $\delta h = 0.1$ m to distinguish between these two transport regimes [Gordon et al., 2009, Nishimura and Nemoto, 2005]. As Figure 4.8 suggests, blowing snow (red line) has a much larger fraction of small particles compared to drifting snow (blue line), confirming the control exerted by particle inertia in the suspension process.

Figure 4.7 also indicates an increase in snow depth over the whole leeward side of the hill. This accumulation is not likely to be caused by deposition of drifting snow, but rather by the recirculation of snow particles behind the ridge. As suggested by Figure 4.9, in fact, the mass flux at the toe of the

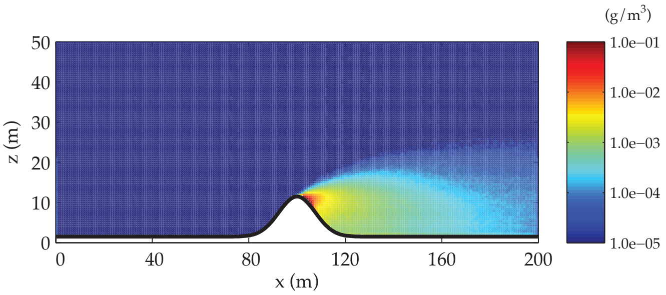

Figure 4.6 – Time-averaged snow concentration field around the Gaussian ridge.

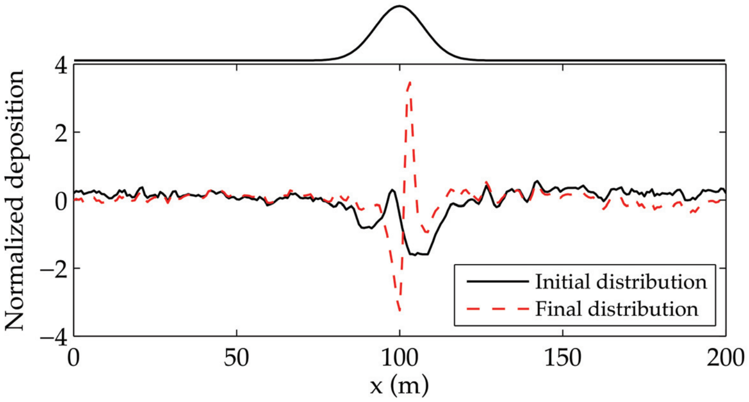

Figure 4.7 – Longitudinal profiles of snow depth at the beginning (red dashed line) and at the end (black solid line) of the snow transport simulation. The longitudinal profiles are obtained by space averaging in the $y-$direction.

leeward slope is negative, i.e., directed towards the hill.

4.5 Discussion and conclusions

We adopted a combined LES-IBM-LSM model to simulate aeolian snow transport over a Gaussian ridge. We previously used the same model set-up and case study to simulate preferential deposition of snowfall. Here, we extended our analysis by including the effect of drifting and blowing on the distribution of snow depth around the ridge.

We initialized the snow depth distribution with the preferential deposition pattern obtained from our snowfall simulation (chapter 1) and increased the wind speed around the ridge so to generate aerodynamic entrainment of particles in the areas where the surface shear stress exceeds the fluid threshold. The results indicate that these areas are located on the windward side of the hilltop. Here, particles start a saltation process that leads them towards the leeward side of the ridge. During the saltation process, splash entrainment provides an additional and relevant contribution to surface erosion. We estimated that splash entrainment is significantly more efficient than aerodynamic entrainment in lifting snow particle from the surface. Although recent wind tunnel studies [Paterna et al., 2016, in review] indicated that splash may indeed play the most important role in snow entrainment over flat

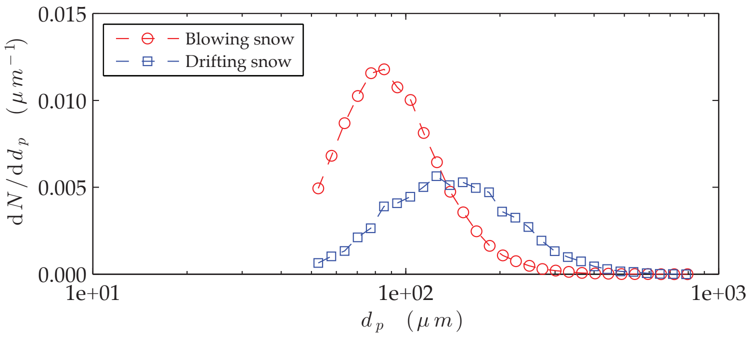

Figure 4.8 – Particle size distributions of blowing snow (red line) and drifting snow (blue line).

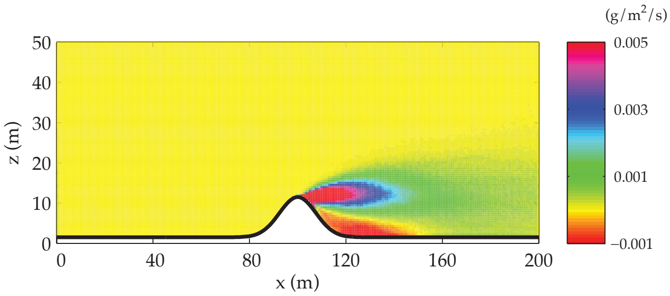

Figure 4.9 – Time-averaged horizontal mass flux around the Gaussian ridge. Negative values indicate mass fluxes that are in the opposite direction to x.

surfaces, this is the first time that the relative contribution is investigated over complex topography with a physically based ejection function. Our observations on the relative importance of aerodynamic and splash entrainment may also prove relevant at much smaller scale, e.g., for the development of snow dunes.

Once the saltating snow particles reach the leeward side of the ridge, the decreased wind velocity is not sufficient to sustain the drifting process and a significant deposition occurs. Some of the smaller particles, however, are caught in the turbulent flow and become suspended in the recirculation region behind the ridge. Our results highlighted a visible plume of blowing snow departing from the leeward side of the hill summit. As a result of these transport processes, the final snow depth distribution varied significantly from the initial one. In particular, we observed a relevant decrease in snow depth on the windward side of the hilltop, which is where a local maximum of snowfall deposition was observed (Figure 1.6). Conversely, our results indicated the formation of a deposition maximum on the leeward side of the hill. This may be the main mechanism leading to cornice formation, although further studies would be necessary to thoroughly investigate the process. Finally, we observed that particles suspended in the recirculation region are preferentially advected towards the toe of the leeward slope, which causes an overall increase of snow depth in this region.

Overall, the proposed modeling approach seems to provide a valuable tool for simulation of aeolian transport over complex terrain. As such, it may guide future studies to more reliable estimations of snow erosion and deposition over realistic alpine topographies, as well as on Antarctic surfaces. Future model developments will include the spatial and temporal evolution of the surface, such that the effects of prolonged erosion and deposition on the flow field will be taken into account. Furthermore, such improvements will allow us to study in larger detail some relevant surface processes, such as the formation of dunes and sastrugi.

Our model results also point toward the need of accounting for frequency and intensity of drifting snow events in hydrological models at hillslope scale. The redistribution of large amounts of snow from the windward slope the leeward slope may radically changes the volume of water routed to the different branches of the stream network, with relevant implications for the spatial and temporal variability of streamflow and stream temperature.

4.6 Acknowledgements

I wish to thank Marco Giometto for his support in the implementation and application of the LES code.

5 Thermodynamics in the hydrologic response: Travel time formulation and application to Alpine catchments

An edited version of this chapter was published by AGU. ©2015. *American Geophysical Union.* All Rights Reserved.

Comola, F., B. Schaefli, A. Rinaldo, and M. Lehning (2015), Thermodynamics in the hydrologic response: Travel time formulation and application to Alpine catchments, Water Resour. Res., 51, 1671–1687, doi:10.1002/2014WR016228.

To view the published open abstract, go to http://dx.doi.org and enter the DOI.

F. C. developed the theoretical and numerical model, took part in the research design, performed the research, analyzed the data, and contributed to the writing of the paper.

5.1 abstract

This paper presents a spatially-explicit model for hydro-thermal response simulations of Alpine catchments, accounting for advective and non-advective energy fluxes in stream networks characterized by arbitrary degrees of geomorphological complexity. The relevance of the work stems from the increasing scientific interest concerning the impacts of the warming climate on water resources management and temperature-controlled ecological processes. The description of the advective energy fluxes is cast in a travel time formulation of water and energy transport, resulting in a closed form solution for water temperature evolution in the soil compartment. The application to Alpine catchments hinges on the boundary conditions provided by the fully-distributed and physically-based snow model Alpine3D. The performance of the simulations is illustrated by comparing modeled and measured hydrographs and thermographs at the outlet of the Dischma catchment (45 km^2) in the Swiss Alps. The Monte Carlo calibration shows that the model is robust and that a simultaneous fitting of streamflow and stream temperature reduces the uncertainty in the hydrological parameters estimation. The calibrated model also provides a good fit to the measurements in the validation period, suggesting that it could be employed for predictive applications, both for hydrological and ecological purposes. The temperature of the subsurface flow, as described by the proposed travel time formulation, proves warmer than the stream temperature during winter and colder during summer. Finally, the spatially-explicit results of the model during snowmelt show a notable hydro-thermal spatial variability in the river network, owing to the small spatial correlation of infiltration and meteorological forcings in Alpine regions.

5.2 Introduction

In Alpine catchments, a significant amount of precipitation is stored as snow and ice throughout an extended period of time before the start of the melting process at the beginning of the summer season. Accordingly, snow and ice are very important water resources not only for mountain catchments but also for large and dry lowland areas of western America, central Asia, northern India and southern Europe [Barnett et al., 2005, Trujillo and Molotch, 2014]. This yearly accumulation and melt of snow and ice give rise to strong annual hydrological cycles, with pronounced low flows during the winter [Schaefli et al., 2013], melt-driven high flows throughout the summer and strong recessions during fall [Biswal and Marani, 2010, Mutzner et al., 2013]. Given that the yearly cycle of snow accumulation and melt strongly depends on temperature, the global warming widely predicted by climate models will most likely have a strong impact and the hydrologic regime of Alpine catchments. Recent investigations suggest that a shift in the streamflow peak from summer to spring may be expected due to the warming-induced earlier melting of snow and ice [Bavay et al., 2009, 2013], possibly accompanied by lower glacier melt rates [Stahl et al., 2008] and a change in snow cover [Stewart et al., 2005].

The hydrologic regime of Alpine catchments has a strong impact on their thermal response [Brown and Hannah, 2007] due to the different temperatures of the streamflow sources, i.e. meltwater from glaciers and snowpack [Finger et al., 2013], karstic groundwater and hillslope aquifers [Brown et al., 2005]. The thermal regime of Alpine catchments, in turn, strongly controls ecological processes, as many freshwater organisms tend to migrate according to their temperature preferences [Coutant, 1977]. The thermal cycle of Alpine streams generally presents a close to freezing temperature during winter, an increasing phase from spring to summer and a descending phase in autumn. In recent years the scientific community has developed a great interest in the effects of climate change on stream temperature [Matulla et al., 2007, Kurylyk et al., 2013]. A intensive analysis of high resolution records collected by Hari et al. [2006] in 25 Alpine streams in Switzerland demonstrated that significant warming has taken place during the last 25 years of the 20th century. The stream network being an important ecological corridor [Ward and Tockner, 2001], the warming climate is thus expected to cause a redistribution, if not even the extinction, of many aquatic species [Mohseni et al., 2003].

All these investigations emphasize the strong interconnection between streamflow, stream temperature and ecosystem services, suggesting that a reliable model for flow and temperature simulations in Alpine streams may be an extremely useful tool to predict the impacts of climate, land use or water management changes on water resources and biodiversity. Numerical simulations are however a challenging task, due to the complexity and space-time variability of meteorology, near-surface snow processes, transport and exchange dynamics in soils and channel networks. The existing modeling approaches differ from each other in terms of spatial detail, ranging from fully-distributed to lumped models, and physical representativeness, ranging from physically based to conceptual models. For a review of rainfall-runoff and stream temperature models see e.g. Todini [2007] and Caissie [2006], respectively.

The physical description of the transport dynamics may be addressed through a Lagrangian or an Eulerian framework that formally differ from each other but both are derived from conservation equations in a control volume. The formulation of transport by travel time distribution arises in a Lagrangian stochastic context and has initially been applied to provide a statistical mechanical description of solute mass response functions [Rinaldo and Marani, 1987, 1989] and geomorphological dispersion in the hydrologic response [Rinaldo et al., 2006, 1991, Rinaldo and Rodriguez-Iturbe, 1996]. More recently, the travel time framework has led to theoretical advances in the description of soil moisture dynamics [Botter et al., 2010, Rinaldo et al., 2011] and kinematics of water age mixing in soils [Benettin et al., 2013a]. On the modeling side, successful applications of the travel time formulation of reactive solutes transport [Botter et al., 2005] have been achieved by Bertuzzo et al. [2013] and Benettin et al. [2013b].

In this study, we seek a novel approach to simulate hydrologic and thermal regimes, describing the mass and energy transport in soil compartments with a travel time framework. The application of the derived formulation to Alpine catchments relies on the boundary conditions provided by Alpine3D, the physically-based and fully-distributed model of snow processes developed at the WSL institute for snow and avalanche research [Lehning et al., 2006]. The theoretical relevance of the work stems from an extension of previous travel time frameworks to a more complete treatment that includes the energy dynamics. From a practical perspective, we believe that the coupled and spatially-explicit simulation of streamflow and temperature is promising for future investigations of ecohydrological processes in Alpine regions.

In section 5.3, we derive the travel time formulation of energy transport at sub-catchment scale, recalling previous results on the age mixing theory [Botter et al., 2010]. In fact, the age of water cannot be disregarded when simulating the concentration in water of reactive scalars, such as chemicals or temperature, for which the exchange processes strongly depend on the contact time between mobile (water) and immobile (soil) phases. In section 5.4, the numerical model used to solve the coupled hydro-thermal problem is introduced. Following, the case study of the high Alpine Dischma catchment (Grisons, Switzerland) is described. The numerical results are discussed in section 5.6 and conclusions finally close the paper.

5.3 Theoretical framework

In this section we propose a travel time formulation of mass and energy transport at sub-catchment scale, resulting in a closed form solution of water temperature evolution in the soil compartment. In order to facilitate the reading, we also provide a list of the recurrent symbols in Table 5.1.

Table 5.1 – List and meaning of symbols used in chapter 5.

Symbol (units)	Meaning
$S(t)$ (m)	Groundwater storage per unit area.
$I(t)$ (ms^{-1})	Infiltration.
$Q(t)$ (ms^{-1})	Subsurface flow.
$E(t)$ (ms^{-1})	Evapo-transpiration.
t_i (s)	Injection time
$P(t-t_i \mid t_i)$ (−)	Travel time cumulative distribution function.
$p(t-t_i \mid t_i)$ (s^{-1})	Travel time probability density function.
$\theta(t_i)$ (−)	infiltration partition function.
$H(t)$ (Jm^{-2})	Energy of the groundwater storage.
$T(t-t_i, t_i)$ (K)	Temperature of the transport volume.
$T_I(t)$ (K)	Temperature of the infiltrating water.
$\phi(t)$ (Wm^{-2})	Energy flux.
K_s (s)	Characteristic time of thermal exchange.

5.3.1 Mass transport

The travel time formulation of water transport that we present hereafter was initially proposed by Botter et al. [2010], who derived and discussed the equations in much details. In this section we provide a concise and effective recall of those results that are essential to further derive the formulation of energy transport.

Let us assume the control volume to be the portion of soil delimited, laterally, by the water divide of the catchment and bounded by the land surface. The lower boundary is considered as a deep and impervious surface [Brutsaert, 2005]. The domain can be further decomposed in smaller units, called sub-catchments, each of them defined as the portion of a catchment draining into a single stream of the river network, as shown in Fig. 5.1a. The sub-catchment water storage $S(t)$ (m) is fed by the infiltration $I(t)$ (ms^{-1}) occurring at the land surface and depleted by subsurface flow into the stream $Q(t)$ (ms^{-1}) and evapo-transpiration $E(t)$ (ms^{-1}). All the introduced variables are expressed per unit sub-catchment area.

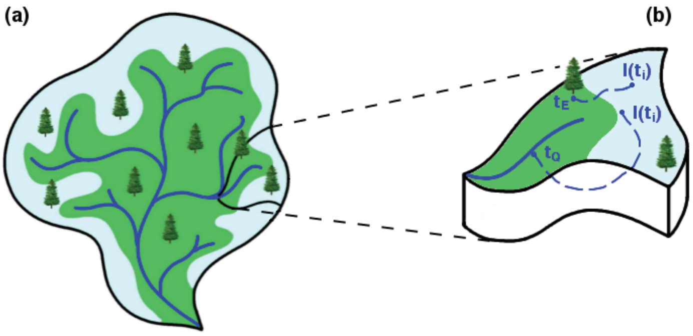

Figure 5.1 – (a) Subdivision of the catchment into source areas (sub-catchments) assumed to be independent hydrological control volumes. Each sub-catchment drains water into a single stream, which can be of order 1 or higher. (b) Trajectory of generic transport volumes, infiltrating at injection time t_i and leaving the control volume through evapo-transpiration, after a travel time t_E, or through subsurface flow, after a travel time t_Q.

Let $I(t_i)dt_i$ (m) be a transport volume infiltrating at the injection time t_i and $t - t_i$ (s) be its travel time, i.e. the time elapsed between t_i and the time $t > t_i$ at which the transport volume leaves the sub-catchment through $Q(t)$ or $E(t)$. The travel time is, in general, a function of the injection time, as it strongly depends on the moisture content of the soil at the time at which the particle infiltrates [Rinaldo et al., 2011]. Every transport volume injected in the sub-catchment at time t_i follows a different trajectory and presents a different value of travel time. One may thus consider the travel time of each transport volume as an independent realization of a stochastic ergodic process associated to the exceedance probability function $P(t - t_i \mid t_i)$.

The groundwater storage $S(t)$ contained in the control volume is given by the sum of all transport volumes infiltrating at increasing injection times t_i whose travel times are shorter than $t - t_i$, which reads as

$$S(t) = \int_{-\infty}^{t} I(t_i) P(t - t_i \mid t_i) dt_i. \tag{5.1}$$

The time rate variation of water storage may be obtained by differentiating Eq. 5.1 with respect to t. Using the Leibniz rule, it follows that

$$\frac{dS}{dt} = I(t) - \int_{-\infty}^{t} I(t_i) p(t - t_i \mid t_i) dt_i \tag{5.2}$$

where $p(t - t_i \mid t_i)$ (s^{-1}) is the probability density function obtained by differentiating $P(t - t_i \mid t_i)$ with respect to t. Eq. 5.2 can be seen as a mass balance equation for the control volume where the right hand side is the algebraic sum of all incoming and outgoing fluxes. Consequently, one can write

$$Q(t) + E(t) = \int_{-\infty}^{t} I(t_i) p(t - t_i \mid t_i) dt_i. \tag{5.3}$$

To evaluate the individual contributions of $Q(t)$ and $E(t)$ in Eq. 5.3, one should distinguish between the transport volumes that will be drained by subsurface flow and the ones that will be up-taken by evapo-transpiration processes. As shown in Fig. 5.1b, the travel time can be a travel time to subsurface flow t_Q or a travel time to evapo-transpiration t_E.

Defining $\theta(t_i) \in [0, 1]$ as the infiltration partition function that expresses the relative fraction of transport volumes, injected at t_i, that will leave the sub-catchment as subsurface flow (see e.g. Bertuzzo et al. [2013] for more details), $p(t - t_i \mid t_i)$ can now be written as

$$p(t - t_i \mid t_i) = \theta(t_i) p_Q(t - t_i \mid t_i) + [1 - \theta(t_i)] p_E(t - t_i \mid t_i). \tag{5.4}$$

Finally, one may write the individual contributions in Eq. 5.3 as

$$Q(t) = \int_{-\infty}^{t} I(t_i) \theta(t_i) p_Q(t - t_i \mid t_i) dt_i \tag{5.5}$$

$$E(t) = \int_{-\infty}^{t} I(t_i) [1 - \theta(t_i)] p_E(t - t_i \mid t_i) dt_i. \tag{5.6}$$

To derive an analytical solution for $p_Q(t - t_i \mid t_i)$ and $p_E(t - t_i \mid t_i)$ one shall write the mass conservation of the generic transport volume. Let $I(t_i) dt_i P(t - t_i \mid t_i)$ be the fraction of the transport volume injected at time t_i that is still inside the sub-catchment at time t. Assuming that part of the transport volume is up-taken by Q and E at time t following a random sampling process, the sought mass conservation equation reads

$$\frac{d\left[I(t_i)dt_iP(t-t_i \mid t_i)\right]}{dt} = -\left[Q(t)+E(t)\right]\frac{I(t_i)dt_iP(t-t_i \mid t_i)}{S(t)}. \tag{5.7}$$

Eq. 5.7 states that Q and E drive the rate of change of the transport volume proportionally to its relative abundance within the water storage - according to the random sampling assumption - given by the ratio of the transport volume over the total storage at the right hand side. Eq. 5.7 leads to the first order, homogeneous, linear ODE with non-constant coefficients

$$\frac{dP(t-t_i \mid t_i)}{dt} + \frac{Q(t)+E(t)}{S(t)}P(t-t_i \mid t_i) = 0, \tag{5.8}$$

whose solution, after imposing the initial condition $P(0 \mid t_i) = 1$, reads as

$$P(t-t_i \mid t_i) = e^{-\int_{t_i}^{t}\frac{Q(x)+E(x)}{S(x)}dx}. \tag{5.9}$$

By replacing Eq. 5.4 into Eq. 5.8 and using the result from Eq. 5.9, one finally obtains

$$p_Q(t-t_i \mid t_i) = \frac{Q(t)}{S(t)\theta(t_i)}e^{-\int_{t_i}^{t}\frac{Q(x)+E(x)}{S(x)}dx} \tag{5.10}$$

$$p_E(t-t_i \mid t_i) = \frac{E(t)}{S(t)[1-\theta(t_i)]}e^{-\int_{t_i}^{t}\frac{Q(x)+E(x)}{S(x)}dx}. \tag{5.11}$$

Eq. 5.10 and 5.11 express the travel time distributions of transport volumes infiltrating at time t_i that leave the domain through subsurface and evapo-transpiration.

5.3.2 Energy transport

To derive the travel time formulation of energy transport we consider temperature as a passive-reactive scalar carried by water, as Bertuzzo et al. [2013] also assumed for chemical tracers. On one side, passivity implies that water temperature does not affect the advection field. On the other side, reactivity implies that the amount of thermal energy of a generic transport volume is not conserved during the transport processes.

Let $T(t-t_i, t_i)$ (K) be the temperature at time t of the transport volume injected at time t_i. The assumption that $T(t-t_i, t_i)$ does not depend on any spatial variable can be reasonably accepted if the spatial correlation scale of the infiltration field is much larger than the one of the heterogeneous reactive and advective processes. Similar considerations have been used to derive other travel time formulations of transport for passive-reactive scalars [Benettin et al., 2013b]. Point sources are instead a delicate subject, as they tend to provide inherently stochastic processes [Dagan, 1990, Rinaldo and Marani, 1989]. One may express the internal energy of the groudwater storage $H(t)$ (Jm^{-2}) at time t as

$$H(t) = \rho c_p \int_{-\infty}^{t} I(t_i) T(t - t_i, t_i) P(t - t_i \mid t_i) dt_i, \tag{5.12}$$

where ρ (kg m^{-3}) and c_p (J kg^{-1}K^{-1}) are density and specific heat of water. By differentiating Eq. 5.12 using the Leibniz rule, one my express the time rate variation of the energy of the water storage as

$$\begin{aligned} \frac{dH}{dt} &= \rho c_p I(t) T_I(t) - \rho c_p \int_{-\infty}^{t} I(t_i) T(t - t_i, t_i) p(t - t_i \mid t_i) dt_i \\ &+ \rho c_p \int_{-\infty}^{t} I(t_i) P(t - t_i \mid t_i) \frac{dT(t - t_i, t_i)}{dt} dt_i. \end{aligned} \tag{5.13}$$

Eq. 5.13 is the energy balance equation for the control volume and the right hand side is the algebraic sum of the incoming and outgoing energy fluxes. In particular, the first term is the energy gained from infiltration $\phi_I(t)$ (Wm^{-2}), where $T_I(t)$ (K) is the temperature of the water volume infiltrating at time t. The second terms represents the advective energy fluxes driven by subsurface flow $\phi_Q(t)$ and evapo-transpiration $\phi_E(t)$

$$\phi_Q(t) + \phi_E(t) = -\rho c_p \int_{-\infty}^{t} I(t_i) T(t - t_i, t_i) p(t - t_i \mid t_i) dt_i. \tag{5.14}$$

The third term includes all the reactive energy processes $\phi_\Delta(t)$ affecting the time evolution of water temperature

$$\phi_\Delta(t) = \rho c_p \int_{-\infty}^{t} I(t_i) P(t - t_i \mid t_i) \frac{dT(t - t_i, t_i)}{dt} dt_i. \tag{5.15}$$

An analytical solution for $T(t - t_i, t_i)$ can be obtained by writing the energy conservation of the transport volume. Let $\rho c_p I(t_i) dt_i T(t - t_i, t_i) P(t - t_i \mid t_i)$ (Jm^{-2}) be the energy of the transport volume fraction that is still inside the sub-catchment at time t. Recalling that $Q(t)$ and $E(t)$ follow a random sampling process among all transport volumes, the energy conservation equation reads as

$$\begin{aligned}\rho c_p \frac{d\left[I(t_i)dt_iP(t-t_i \mid t_i)T(t-t_i,t_i)\right]}{dt} &= -\rho c_p\left[Q(t)+E(t)\right]\frac{I(t_i)dt_iP(t-t_i \mid t_i)}{S(t)}T(t-t_i,t_i)\\ &+ \rho c_p I(t_i)dt_iP(t-t_i \mid t_i)\frac{\left[T_s(t)-T(t-t_i,t_i)\right]}{K_s}. \end{aligned} \tag{5.16}$$

The first term at the right-hand side of Eq. 5.16 represents the advection-driven energy loss due to $Q(t)$ and $E(t)$, which is proportional to the relative abundance of the transport volume in the water storage, according to the random sampling assumption. The second term represents the energy variation due to the reactive processes. A simple yet reasonable parametrization for this term has been introduced by forcing the water-soil thermal exchange to incorporate the effect of all the underlying reactive processes. In this case, soil temperature $T_s(t)$ should act as an external forcing that follows the daily and seasonal cycles resulting from the surface energy budget, which depends on land use, presence of snow/ice cover and slope exposure. Accordingly, the water-soil thermal exchange is modeled as a one way-coupled system and the transport volume experiences an energy gain/loss proportional to the difference between soil temperature and water temperature. Recalling that the spatial correlation of infiltration is assumed much larger than the one of reactive processes, we can consider the amount of energy exchanged between water and soil as a function of the contact time, disregarding the specific trajectory followed by the transport volume. K_s (s) is an effective parameter influencing the characteristic time of the water-soil thermal exchange.

Recalling Eq. 5.7, after proper simplifications Eq. 5.16 leads to the following first order, non-homogeneous, linear ODE with non-constant coefficients

$$\frac{dT(t-t_i,t_i)}{dt}+\frac{T(t-t_i,t_i)}{K_s}=\frac{T_s(t)}{K_s}. \tag{5.17}$$

The analytical solution of Eq. 5.17, sought by imposing the initial condition $T(0,t_i)=T_I(t_i)$, reads

$$T(t-t_i,t_i)=\left[T_I(t_i)+\int_{t_i}^{t}\frac{T_s(x)}{K_s}e^{(x-t_i)/K_s}dx\right]\cdot e^{-(t-t_i)/K_s}. \tag{5.18}$$

One may notice that, with respect to Eq. 5.9, there is an additional term that sums up to the initial condition, arising from the non-homogeneous nature of the ODE. Two sample solutions of Eq. 5.18, obtained for two different values of K_s, are shown in Fig. 5.2. Eq. 5.18 reduces to the much simpler form of Eq. 5.19 when assuming a constant soil temperature.

$$T(t-t_i,t_i)=T_I(t_i)e^{-(t-t_i)/K_s}+T_s\left[1-e^{-(t-t_i)/K_s}\right]. \tag{5.19}$$

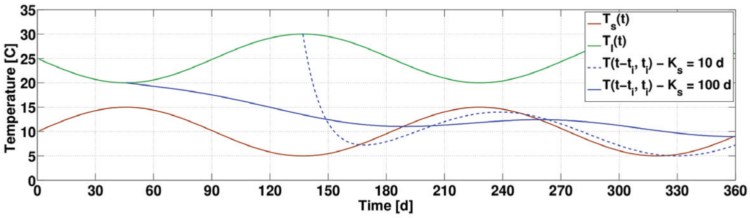

Figure 5.2 – Sample solutions of Eq. 5.18 for two different values of K_s. The solutions are obtained considering a constant storage $S(t) = 5$ m and the shown sinusoidal evolutions for $T_s(t)$ and $T_I(t)$.

Recalling Eqs. 5.8, 5.12 and 5.17, Eq. 5.14 and Eq. 5.15 finally read

$$\phi_Q(t) + \phi_E(t) = \frac{Q(t) + E(t)}{S(t)} H(t) \tag{5.20}$$

$$\phi_\Delta(t) = \frac{\left[\rho c_p S(t) T_s(t) - H(t)\right]}{K_s}. \tag{5.21}$$

The following section will show how the energy balance Eq. 5.13 can be efficiently solved using Eqs. 5.20 and 5.21 to express the energy fluxes in terms of the state variables $S(t)$ and $H(t)$.

Special attention has to be paid when applying the proposed framework to Alpine catchments, where the passivity assumption may break down. In fact, when water temperature approaches 0 °C, the freezing process affects mass transport dynamics. The relaxation of the passivity assumption would require an additional temperature-dependent term in the mass balance Eq. 5.7 to account for the probability that the transport volume undergoes freezing and melting processes. Moreover, the energy balance Eq. 5.16 should also be extended to account for the latent heat fluxes associated to freezing and melting. Although a fully coupled description of mass and energy transport in an active-scalar travel time framework seems feasible, it would certainly require additional and not desirable parametrizations. In the following section we therefore propose a different solution for reliable applications of the passive-scalar based model to Alpine catchments, based on the physical description of surface processes provided by Alpine3D.

5.4 Implementation for Alpine catchments

This section presents the implementation for Alpine catchments of the spatially-explicit hydro-thermal response model. To properly account for soil water freezing, we implement the derived equations in the physical model Alpine3D, which simulates local scale snow processes and transport dynamics in the surface soil layer. The thickness of this layer is chosen so that the seasonal temperature variations at the bottom do not induce water freezing. In fact, the field investigations carried out by Jaesche et al. [2003] and Bayard et al. [2005] in high Alpine catchments have shown that temperature does not drop below the freezing point at depth larger than few meters. Accordingly, the assumptions of the travel time formulation hold for the simulation of the transport dynamics at sub-catchment scale using the boundary conditions provided by Alpine3D in terms of mass and energy fluxes at the bottom of the surface soil layer.

For a better description of the underlying hydrological processes, the travel time model accounts for two control volumes below the surface soil layer solved by Alpine3D, namely a upper and a lower compartment, as shown in Fig. 5.3. A similar model set-up was also adopted e.g. by Benettin et al. [2013b] and Bertuzzo et al. [2013]. In fact, the general solution presented in section 5.3 can be applied to each control volume provided that the corresponding incoming and outgoing water and energy fluxes are considered.

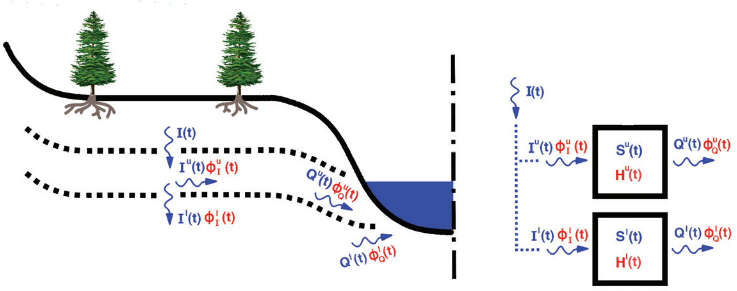

Figure 5.3 – Schematic representation of the mass and energy fluxes associated to the two modeled soil compartments. The upper compartment has a groundwater storage $S^u(t)$ with energy $H^u(t)$, while the lower one has a groundwater storage $S^l(t)$ with energy $H^l(t)$ (for an explanation of the variables see section 5.4).

5.4.1 Streamflow simulation

The flow simulation at sub-catchment scale is carried out considering that the portion $I^l(t) = \min\{R_{max}, I(t)\}$ of the infiltrating water $I(t)$ (ms^{-1}) at the bottom of the surface layer, given as boundary condition by Alpine3D, drains directly into the lower compartment, where R_{max} (ms^{-1}) is the maximum recharge rate. The exceeding part $I^u(t) = I(t) - I^l(t)$ feeds the upper compartment. We assume that the control volumes are not affected by evapo-transpiration fluxes, which take place in the surface soil layer and are fully simulated by Alpine3D. Accordingly, we assign $E^u(t) = E^l(t) = 0$. The subsurface flows from the upper and lower compartments, $Q^u(t)$ and $Q^l(t)$ (ms^{-1}) respectively, are collected by the stream and transported to the sub-catchment outlet. Therefore, the hydrologic response at sub-catchment scale can be described by two mass balances in the soil compartments (Eqs. 5.22 and 5.23, which are analogous to Eq. 5.2) and a mass balance in the stream (Eq. 5.24).

$$\frac{dS^u(t)}{dt} = I(t) - \min\{R_{max}, I(t)\} - Q^u(t) \tag{5.22}$$

$$\frac{dS^l(t)}{dt} = \min\{R_{max}, I(t)\} - Q^l(t) \tag{5.23}$$

$$Q^{out}(t) = Q^{in}(t) + [Q^{u}(t)] + Q^{l}(t)]A \tag{5.24}$$

where $S^u(t)$, $S^l(t)$ (m) are the water storages in the upper and lower compartment. $Q^{in}(t)$, $Q^{out}(t)$ (m^3s^{-1}) are the streamflows at the inlet and outlet of the stream and A (m^2) is the area of the sub-catchment. Eq. 5.24 embeds the assumption of instantaneous advection in the stream, which can be reasonably accepted considering that open channel flow is orders of magnitude faster than water transport in the soil compartments.

In the most general travel time framework, $Q^u(t)$ and $Q^l(t)$ are expressed by Eq. 5.5. Here we assume that the hydrologic response of the control volumes is linear and time-invariant, as the water age mixing induced by soil moisture dynamics mainly occurs in the surface soil layer, simulated by Alpine3D. Similar assumptions were introduced also by Botter et al. [2010]. Consequently, $Q^u(t)$ and $Q^l(t)$ can be expressed by the convolution integrals

$$Q^{u}(t) = \int_{-\infty}^{t} I^{u}(t_i) p^{u}(t - t_i) dt_i \tag{5.25}$$

$$Q^{l}(t) = \int_{-\infty}^{t} I^{l}(t_i) p^{l}(t - t_i) dt_i \tag{5.26}$$

where $p^u(t - t_i)$ and $p^l(t - t_i)$ (s^{-1}) are the unconditional travel time distributions in the two soil compartments, obtained as special cases of Eq. 5.10 under the stationarity assumption. Here we adopt exponential distributions, whose mean values τ^u and τ^l are the average travel times in the two soil compartments. It can be easily shown that, in this case, the expressions resulting from Eq. 5.25 and Eq. 5.26 are equivalent to the solution of linear reservoirs, i.e. $Q^u(t) = S^u(t)/\tau^u$ and $Q^l(t) = S^l(t)/\tau^l$. Previous investigations [Alexander, 1972, Pilgrim et al., 1982] suggested that the average travel time can be expressed as a power law of the sub-catchment size, i.e. $\tau^u = \overline{\tau}^u (A/A_{tot})^{1/3}$ and $\tau^l = \overline{\tau}^l (A/A_{tot})^{1/3}$, where A_{tot} (m^2) is the area of the entire catchment. Assuming such a scaling, the coefficients $\overline{\tau}^u$, $\overline{\tau}^l$ (s) can be assumed valid for all sub-catchments and obtained through calibration [Schaefli et al., 2014].

The algorithm is structured in such a way that Eqs. 5.22, 5.23 and 5.24 are initially solved for headwater sub-catchments. In the following steps, the outgoing flows $Q^{out}(t)$ from streams of order 1 are summed up to provide the incoming streamflow $Q^{in}(t)$ for the streams of higher order. The scheme proceeds until $Q^{in}(t)$ and $Q^{out}(t)$ are calculated for each node of the stream network. The values at points along the streams between the network nodes are obtained through linear interpolation.

5.4.2 Stream temperature simulation

Temperature simulation at sub-catchment scale is based on the solution of a system similar to Eqs. 5.22, 5.23 and 5.24. Here, two equations describe the energy balance in the soil compartments (Eqs. 5.27 and 5.28, which are analogous to Eq. 5.13) and one equation describes the energy balance in the stream (Eq. 5.29).

$$\frac{dH^u(t)}{dt} = \phi_I^u(t) - \phi_Q^u(t) + \phi_\Delta^u(t) \tag{5.27}$$

$$\frac{dH^l(t)}{dt} = \phi_I^l(t) - \phi_Q^l(t) + \phi_\Delta^l(t) \tag{5.28}$$

$$\phi_Q^{out}(t) = \phi_Q^{in}(t) + [\phi_Q^u(t) + \phi_Q^l(t)]A + \sum \phi^{na} \tag{5.29}$$

$H^u(t)$ and $H^l(t)$ (Jm^{-2}) are the energy of the groundwater storages in the upper and lower soil compartments. $\phi_I^u(t) = \rho c_p I^u(t) T_I(t)$ and $\phi_I^l(t) = \rho c_p I^l(t) T_I(t)$ (Wm^{-2}) are the incoming energy fluxes in the two soil compartments, and are functions of the temperature of infiltrating water $T_I(t)$. The infiltrating water is assumed to be in local thermal equilibrium with the bottom of the surface layer, whose temperature $T_s(t)$ is given as boundary condition by Alpine3D.

The outgoing energy fluxes can be expressed, recalling Eq. 5.20, as $\phi_Q^u(t) = Q^u(t)H^u(t)/S^u(t)$ and $\phi_Q^l(t) = Q^l(t)H^l(t)/S^l(t)$. One may notice that, owing the absence of evapo-transpiration fluxes below the surface soil layer, we can assign $\phi_E^u(t) = \phi_E^l(t) = 0$. According to Eq. 5.21, the water-soil thermal exchange fluxes are $\phi_\Delta^u(t) = [\rho c_p S^u(t) T_s(t) - H^u(t)]/K_s$ and $\phi_\Delta^l(t) = [\rho c_p S^l(t)\overline{T_s} - H^l(t)]/K_s$. In the upper compartment, we assume the soil temperature to be equal to $T_s(t)$ and, in the lower compartment, to be constant and equal to the time average $\overline{T_s}$ [Peters-Lidard et al., 1997] .

Eq. 5.29 refers to the energy balance in the stream. $\phi_Q^{in}(t) = \rho c_p Q^{in}(t) T_Q^{in}(t)$ and $\phi_Q^{out}(t) = \rho c_p Q^{out}(t) T_Q^{out}(t)$ (W) are the advective energy fluxes at the inlet and at the outlet of the stream. $T_Q^{in}(t)$ and $T_Q^{out}(t)$ are the temperatures of the incoming and outgoing streamflow. $\sum \phi^{na}$ is the sum of the non-advective energy fluxes, taking place both at the water surface - sensible heat flux $\phi_h(t)$, latent heat flux $\phi_e(t)$ and net radiative flux $\phi_r(t)$ - and at the river bed - conductive heat flux $\phi_g(t)$ and friction dissipation $\phi_f(t)$. These fluxes are not accounted for in the proposed travel time framework, which only describes advective fluxes, but standard formulations can be found in literature [Brown, 1969].

$$\phi_h(t) = \rho_a c_{pa} C_h U_a [T_a(t) - T_c(t)] wl \tag{5.30}$$

$$\phi_e(t) = \left(\rho_a 0.622 L/P_a\right) C_e U_a [e_a(t) - e_c(t)] wl \tag{5.31}$$

$$\phi_r(t) = \left[(1-\alpha)R_s(t) + R_l(t) - \epsilon\sigma T_c(t)^4\right] wl \tag{5.32}$$

$$\phi_g(t) = K_g \frac{T_s(t) - T_c(t)}{\Delta z} wl \tag{5.33}$$

$$\phi_f(t) = \gamma \frac{Q^{in}(t) + Q^{out}(t)}{2} \Delta h, \tag{5.34}$$

where U_a ($\mathrm{m\,s^{-1}}$) is the wind velocity, T_a (K) is the air temperature, $e_a(t)$ (Pa) is the atmospheric vapour pressure, R_s and R_l ($\mathrm{Wm^{-2}}$) are incoming shortwave and longwave radiations. C_h and C_e [-] are the bulk coefficients for sensible and latent heat, which are assumed to be equal. Alpine3D provides a fully-distributed and physical description of all these variables [Lehning et al., 2002, Stössel et al., 2010], so that no parametrization is necessary for the simulation of the non-advective energy fluxes.

ρ_a ($\mathrm{kg\,m^{-3}}$), c_{pa} ($\mathrm{J\,kg^{-1}K^{-1}}$) and P_a [Pa] are density, specific heat and total atmospheric pressure, respectively. $T_c \simeq (T_Q^{in} + T_Q^{out})/2$ (K) is the stream temperature. $e_c(t)$ [Pa] is the saturation vapour pressure at the stream surface. α [-] is the water albedo, ϵ [-] is the emissivity of water, σ ($\mathrm{W\,m^{-2}K^{-4}}$) is the Stefan-Boltzmann constant, K_g ($\mathrm{Wm^{-1}K^{-1}}$) is the soil thermal conductivity and Δz (m) is the depth of the surface layer of soil solved by Alpine3D. γ ($\mathrm{N\,m^{-3}}$) is the specific weight of water and Δh (m) is the altitude difference between stream inlet and outlet. l and w (m) are length and width of the stream, the former retrieved from the geomorphological analysis of the digital terrain model and the latter calculated with the relation $w(t) = 12.0\left\{\left[Q^{in}(t) + Q^{out}(t)\right]/2\right\}^{0.49}$, proposed by Magnusson et al. [2012].

Once the mass fluxes in the soil compartments are calculated, Eqs. 5.27, 5.28 and 5.29 can be solved for each sub-catchment to calculate water temperature $T_Q^{out}(t)$ at the outlet of the stream. Similarly to the case of streamflow modeling, the system is initially solved for headwater sub-catchments. In the following steps, outgoing energy fluxes $\phi_Q^{out}(t)$ from streams of order 1 are summed up to provide the incoming energy flux $\phi_Q^{in}(t)$ to streams of higher order. The scheme proceeds until $\phi_Q^{in}(t)$ and $\phi_Q^{out}(t)$ are calculated for each node of the stream network. The values at points along the streams are obtained through linear interpolation. The coupled hydro-thermal response model has 4 parameters to calibrate, summarized in Tab. 5.2.

Table 5.2 – A priori parameter ranges used for uniform parameter sampling during Monte Carlo simulations and sample set providing the best match with measured streamflow and temperature. Stream temperature simulation is affected by all the listed parameters, while stream flow is affected only by the first three.

Parameter	**Lower limit**	**Upper limit**	**Best performance**
R_{max} (mm/d)	5.0	50.0	12.2
$\overline{\tau}^u$ (d)	1.0	100.0	67.7
$\overline{\tau}^l$ (d)	100.0	600.0	288.0
K_s (d)	10.0	500.0	24.7

5.5 Case study and simulation set-up

The Dischma valley is located in the eastern part of the Swiss Alps, as shown in the inset of Fig. 5.4 . The catchment, closed at Dischma Kriegsmatte, drains an area of 43.3 km^2 and has an elevation range from 1677 to 3130 m. The land use is 36% sub-alpine meadow, 34% rock and the remaining part mainly forest and bushes [Swiss Federal Office for Statistic, 2001]. Glaciers cover only 2% of the catchment.

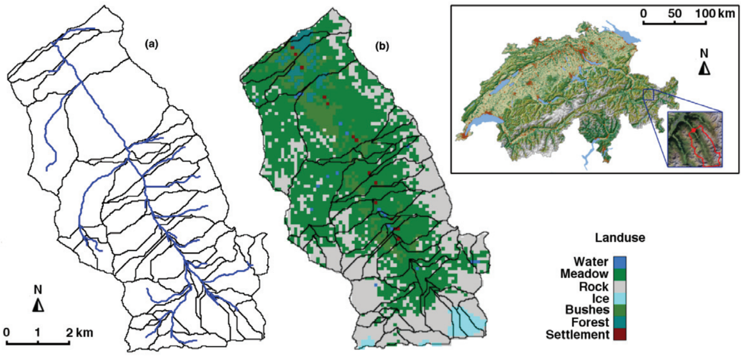

Figure 5.4 – (a) Sub-catchments and stream network delineation obtained applying the Taudem routines on a 25 m resolution digital elevation map [SwissTopo, 2005] and (b) 100 m resolution land use map of the Dischma catchment [Swiss Federal Office for Statistic, 2001].

Since part of the model simulates mass and energy dynamics within the river network, the Taudem routines [Tarboton, 1997] are used to extract the stream network and the sub-catchment distribution based on the information provided by digital elevation maps. The geomorphological analysis of the catchment, applied to a 25 m resolution digital elevation map, delineated 55 sub-catchments, as shown in Fig. 5.4a. This relatively high number of sub-catchments is adopted to validate the assumption of having source areas much smaller than the correlation scale of reactive and advective processes, as stated in Section 5.3. A 100 m resolution land use map of the catchment is shown in Fig. 5.4b.

Alpine3D simulations are carried for the period 1st October 2011 - 1st October 2012, which is used for the calibration of the hydro-thermal model, and 1st October 2012 - 1st October 2013, which is instead used for the model validation. We picked the starting date of the simulation periods in order to have a snow-free initial condition.

The Alpine3D simulations are based on the hourly records of 18 high Alpine automatic weather and snow stations (IMIS), deployed in the area by the Swiss Federal Institute for Snow and Avalanche Research (SLF) in cooperation with the Swiss mountain cantons. Measured parameters include wind, air temperature, relative humidity, snow depth, surface temperature, soil temperature, reflected short wave radiation and three temperatures within the snow cover. More detailed information can be found in [Lehning et al., 1999].

The rectangular domain covers an area of 12.8 km x 15.4 km containing the Dischma catchment and is meshed with squared elements of 100 m side length. The temporal resolution is 1 h. The main source of error affecting Alpine3D simulations lies in the average distance between the meteo-stations, which may not be sufficient to perform an interpolation able to capture the small scale variability of the atmospheric fields. Therefore, Alpine3D generally tends to overestimate snow deposition on steep terrains at high altitudes that, in addition, are smoothed according to spatial resolution of the digital elevation map. Such interpolation errors may ultimately result in an wrong estimation of the streamflow volume at the catchment outlet.

The Alpine3D simulations show that, at a depth of 5 m, soil temperature variations do not induce water freezing at any time of the year. We therefore use the local-scale description of infiltration and soil temperature evolution at this depth as boundary conditions to apply the model described in section 5.4 for the hydro-thermal response simulation of the catchment.

No information is available to assign a priori the initial conditions $S^u(0)$, $S^l(0)$ and $H^u(0)$, $H^l(0)$. Imprecise initial conditions result in a mismatch between modeled and measured values at the onset of the simulation, but their influence is lost after few months. Therefore, we perform an additional hydro-thermal simulation for the period 1st October 2010 - 1st October 2011, imposing arbitrary initial conditions, and use the values of S^u, S^l and H^u, H^l at the end of this simulation as initial conditions for the calibration period.

5.6 Results and discussion

5.6.1 Sensitivity, calibration and validation

Given that the model parameters are not representative of the local scale processes but of the global behaviour of the sub-catchment system, model calibration is in general a necessary operation. However, reasonable parameter ranges can be assigned owing to their direct physical meaning. 10^4 Monte Carlo simulations are initially carried out to fully explore the parameter space shown in Tab. 5.2 and to investigate the model sensitivity.

The fixed parameters are water albedo $\alpha = 0.1$, water density $\rho = 1000$ (kg m^{-3}), air density $\rho_a = 1.30$ (kg m^{-3}), atmospheric pressure $P_a = 101325$ [Pa], water heat capacity $c_p = 4190$ (Jkg^{-1}K^{-1}), air heat capacity $c_{pa} = 1010$ (Jkg^{-1}K^{-1}), emissivity $\epsilon = 0.995$, Stefan-Boltzman constant $\sigma = 5.67 \cdot 10^{-8}$ (Wm^{-2}K^{-4}) and soil thermal conductivity $K_g = 0.004$ (Wm^{-1}K^{-1}).

The performance of each corresponding simulation is evaluated by means of two Nash-Sutcliff indices, NS_Q and NS_T [Nash and Sutcliffe, 1970], the former telling the quality of the simulation in terms of flow and the latter in terms of temperature. It is noteworthy that no absolute meaning can be attached to the values of these indices, because they depend on the shape of the reference signal [Schaefli and Gupta, 2007].

The black lines in Fig. 5.5a and 5.5b show the distribution of the two indices in the chosen ranges, respectively for flow and temperature. To evaluate the robustness of the model, we investigated the parameter distribution of the simulations providing a $NS_Q > 0.91$, which corresponds to the 95% quartile of the NS_Q distribution. A further selection is done by extracting the subset of 100 best temperature simulations, having a $NS_T > 0.69$. In Fig. 5.5b, the filled bars indicate the NS_T distribution in this subset, which is relatively narrow and samples among the largest values of the original set. In Fig. 5.6, the model robustness can be assessed looking at the posterior probability distributions of the parameters, which are located in a well-defined sub space of the prior parameter space. Moreover, It can be noticed that the uncertainty of the hydrological parameters R_{max}, $\overline{\tau}^u$ and $\overline{\tau}^l$ is significantly reduced when streamflow and stream temperature are fitted simultaneously. In fact, the temperature signal contains hydrological information that cannot be directly extrapolated from the streamflow data and therefore helps the understating of the underlying transport processes.

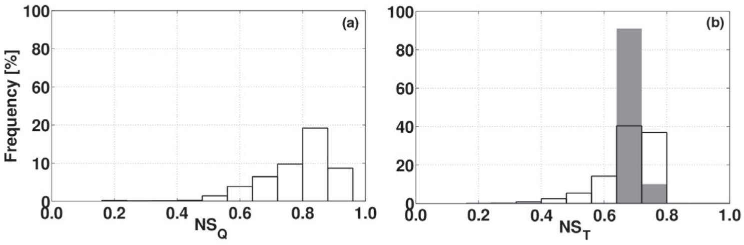

Figure 5.5 – Distribution of the Nash-Sutcliffe indices (a) for streamflow simulations and (b) for stream temperature simulations. Black lines refer to the distributions of all Monte Carlo simulations, the filled bars refer to the distribution of the subset of 100 best temperature simulations ($NS_T > 0.69$) sampled among the 5% best streamflow simulations ($NS_Q > 91$). It is observed that the NS_T distribution of the subset samples among the best temperature simulations of the Monte Carlo sets.

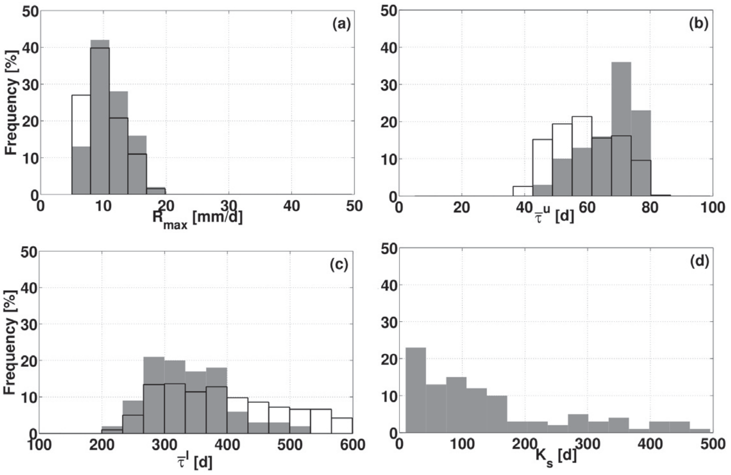

Figure 5.6 – Distribution of the parameters of the hydro-thermal model, i.e. (a) R_{max}, (b) $\overline{\tau}^u$, (c) $\overline{\tau}^l$ and (d) K_s. Black lines show the distribution of the best 5% streamflow simulations, i.e. $NS_Q > 0.91$, while filled bars show the distribution of the subset of 100 best temperature simulations, i.e. $NS_Q > 0.91$ and $NS_T > 0.69$. The results suggest that a simultaneous calibration of streamflow and temperature reduces the uncertainty in the estimation of hydrological parameters.

Within the defined subset, the best temperature simulation is characterized by $NS_T = 0.73$ and $NS_Q = 0.92$, obtained with the parameter set listed in Tab. 5.2. The good match of the corresponding simulations to the measurements is shown in Fig. 5.7a and Fig. 5.7b, together with the interquartile range of the Monte Carlo simulations. The results suggest that the model is less effective in simulating the transport dynamics in June, when streamflow and temperature are respectively under- and over-estimated. It is worth noting that the adopted NS-based calibration for streamflow tends to penalize the correct simulation of the snowmelt peaks in favor of a better representation of the mean flow. However, considering the number and the complexity of involved processes, the general performance turns out to be promising. In particular, we observe good temperature simulations despite of an extremely simple geometric description of the river network and the interactions with the surrounding topography. Moreover, we would like to emphasize that no calibration has been carried out to optimize the boundary conditions provided by Alpine3D, which relies on a physical representation of mass and energy dynamics and is meant to provide reliable predictions at the local scale without prior calibration.

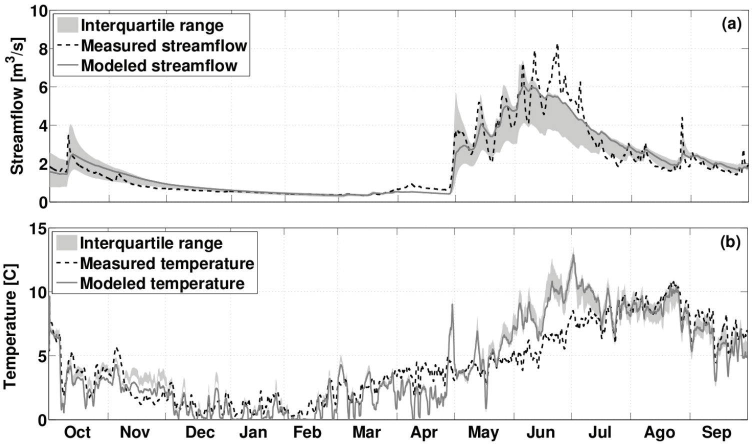

Figure 5.7 – Comparison between measured and modeled (a) streamflow and (b) stream temperature at the outlet, during the calibration period (October 2011 - October 2012). The solid lines represent the modeled results corresponding to the best NS indices (0.92 for streamflow and 0.73 for temperature), the dashed lines represent the measured data. The filled bands correspond to the interquartile range of the Monte Carlo simulations. Signals are averaged over 24 h.

Figs. 5.8a and 5.8b show the results of the model validation, which is performed by using the best parameters set listed in Tab. 5.2. A good match can be observed both for streamflow, with a $NS_Q = 0.83$, and for temperature, with a $NS_T = 0.81$. Such a good agreement suggests that the model setup could be employed for predictive applications, both for hydrological and ecological purposes. The identified range of good parameter sets is of course case study specific and their transferability to other environments has to be tested. For additional information on mean travel time estimations for a large variety of Alpine catchments the reader is referred to [Seeger and Weiler, 2014].

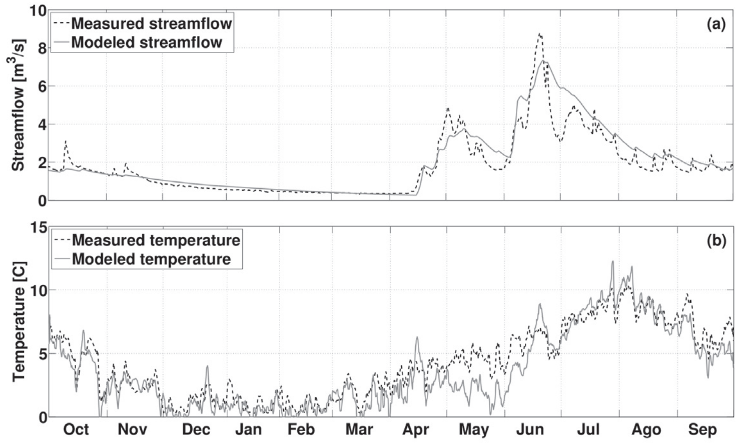

Figure 5.8 – Comparison between measured and modeled (a) streamflow and (b) stream temperature at the outlet during the validation period (October 2012 - October 2013). The corresponding indices are $NS_Q = 0.83$ and $NS_T = 0.81$. Signals are averaged over 24 h.

5.6.2 Temperature cycles of subsurface flow

A numerical experiment is carried out to provide a better insight into the temperature evolution of subsurface flow $T_Q(t)$ at the outlet of the catchment, calculated through the relation $\phi_Q^u(t)+\phi_Q^l(t) = \rho c_p[Q^u(t)+Q^l(t)]T_Q(t)$. This analysis is performed to validate the travel time formulation of the advective energy fluxes. The simulations are carried out with the best parameters set, listed Tab. 5.2. The results are shown in Fig. 5.9a and 5.9b, for the calibration and validation periods respectively.

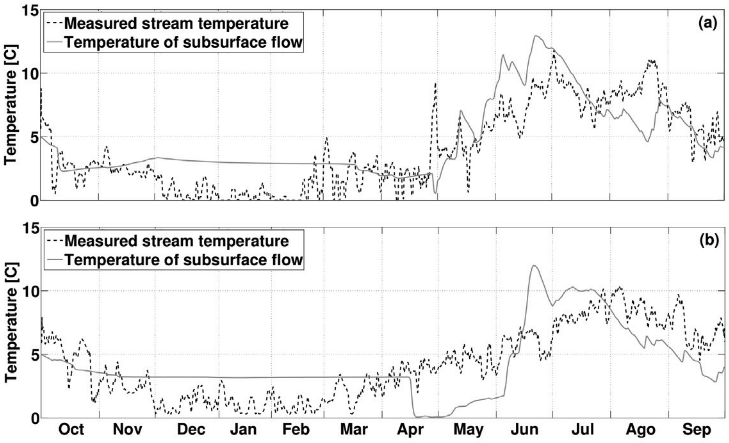

Figure 5.9 – Comparison of the temperature evolution of subsurface flow as opposed to stream temperature at the outlet of the catchment for (a) the calibration period (October 2011 - October 2012) and (b) the validation period (October 2012 - October 2013). Signals are averaged over 24 h.

We can observe that, in the winter season, the modeled subsurface flow temperature is almost constant and warmer than the stream temperature, which is supported by field investigations of Leach and Moore [2014] in Canadian headwater streams. At the onset of the melting season, respectively in late and mid April for the calibration and the validation periods, we observe a rapid decrease in subsurface flow temperature due the relatively fast transport of cold water in the upper soil layer. Following, we observe an increase of subsurface flow temperature due to an efficient thermal exchange with the warmer soil. The peak of subsurface flow temperature is observed in both cases around the end of June, before the peak of stream temperature occurs. Finally, starting from the end of July, subsurface flow temperature is colder than stream temperature, as also suggested by the field investigations of Story et al. [2003] in Canadian headwater streams.

Even though we could not extrapolate relevant information from the available stream temperature data to fully validate these early results, they appear to be consistent with recent studies [Kelleher et al., 2012, Luce et al., 2014] and with the underlying physical processes. This suggests that the proposed travel time formulation of energy transport may be a useful theoretical basis for thermal regime simulations, even in highly heterogeneous and topographically complex Alpine environments. However, as recently observed by MacDonald et al. [2014], there is still a lack of process understanding regarding the relative importance of in-stream energy processes in Alpine catchments. A more in-depth assessment of these model results has therefore to be guided by systematic field-based investigations.

5.6.3 Hydrologic and thermal variability in the stream network

This section presents some preliminary results on the spatial distribution of stream flow and temperature. The results focus in particular on the correlation between the hydro-thermal patterns and the spatial distribution of hydro-meteorological forcings, which might a priori play a determinant role in the hydrologic response of such a small Alpine catchment [Simoni et al., 2011].

Figs. 5.10a and 5.10b show the time-averaged streamflow and temperature over the entire network during May 2012, at the onset of the snowmelt process. The spatial correlation of snow depth is smaller than the size of the catchment [Trujillo et al., 2009], leading to an inhomogeneous distribution of streamflow as also observed by Smith et al. [2014] in Alpine environments. Similarly, stream temperature reflects the highly heterogeneous patterns of soil temperature, air temperature and incoming radiation. These observations support the conclusion that the local scale description of infiltration and meteorology provided by Alpine3D may add a considerable value to hydrological modeling in Alpine regions.

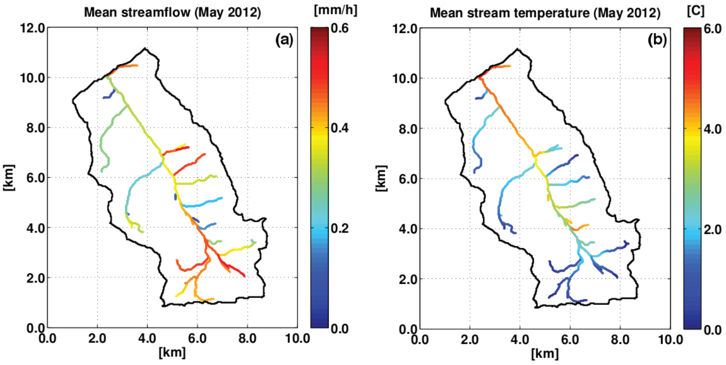

Figure 5.10 – Spatial distribution of (a) specific streamflow (per unit drained area) and (b) stream temperature during the snowmelt event in May 2012. The streamflow pattern strongly reflects the patchy infiltration distribution during snowmelt. The stream temperature pattern reflects the heterogeneous distribution of soil temperature and meteorological forcings.

5.7 Conclusions

In this paper, we presented a model for distributed simulations of streamflow and stream temperature in Alpine catchments. The model set-up relies on the local scale description of mass end energy fluxes in the surface soil layer, provided by the physical snow model Alpine3D, as boundary conditions for a travel time-based transport model at sub-catchment scale. The theoretical derivation of the travel time formulation of water and energy dynamics is based on the water age mixing theory and results in a closed form solution for water temperature evolution in soil compartments.

The model was tested on the Dischma catchment, in the eastern Swiss Alps. The results of a Monte Carlo simulation confirmed that the proposed hydro-thermal response model is robust in the tested parameter ranges. Moreover, a simultaneous fitting of streamflow and temperature reduces the uncertainties in hydrological parameters estimations, owing to the additional information on transport processes contained in the temperature data. Given that the temperature is very easy to observe, it would be helpful to calibrate the model only on short times series of stream temperature. However, from a physical perspective, this might be misleading, as a correct hydrological simulation is essential for the description of transported scalar quantities, such as chemical solutes or temperature. Future tests will show whether additional snapshot streamflow measurement campaigns are sufficient to well constrain all model parameters.

The calibrated model provides a good fit to the measured streamflow and temperature also in the validation period, which is a promising result considering that no calibration has been carried out to optimize the boundary conditions provided by Alpine3D. The observed ranges of good parameters are case specific and their transferability to other environments has to be tested. However, an effective spatial transferability is also expected, owing to the coupling to Alpine3D and to the explicit accounting for geomorphological complexity. On one side, in fact, a physical and spatially distributed description of snow processes does not require specific calibration and, on the other side, hydrologic residence times are strongly connected to sub-catchment size and stream network geometry.

The temporal evolution of subsurface flow, as described by the travel time component of the model, confirms previous experimental observations. In particular, subsurface flow is warmer than streamflow during winter and colder during large part of summer. During the two simulated years, typical observed features are also a drop of subsurface flow temperature at the onset of the melting season, when cold water is transported down to the streams, followed by an increase induced by an efficient thermal exchange with the warming soil. Given the qualitative agreement with field investigations and the support of reasonable physical arguments, we argue that the energy transport in the hydrologic response can be properly cast in a travel time framework, using the boundary condition provided by Alpine3D.

In parallel, we showed that the spatial distribution of streamflow during snowmelt is highly inhomogeneous, owing to the patchy distribution of infiltration. The spatial detail provided by Alpine3D in terms of infiltrating water fluxes is in this sense a noteworthy advantage. Similarly, stream temperature distribution reflects the notable spatial variability of soil temperature, air temperature and incoming radiation, typical of Alpine regions.

Overall, the travel time formulation extended previous findings to a more complete framework that includes energy transport and lead to an effective description of water soil temperature evolution. Moreover, the proposed coupling with Alpine3D yielded promising results and can present a new avenue for the hydro-thermal simulations of Alpine catchments, which has interesting applications, especially in stream ecology.

5.8 Acknowledgments

I would like to thank all the co-authors for their help and feedbacks on the published articles. The streamflow and stream temperature data was obtained from the Swiss Federal Office for the Environment. The meteorological data was obtained from the IMIS (Interkantonales Mess- und Informationssystem) network, MeteoSwiss and SLF stations. I wish to acknowledged Enrico Bertuzzo for his help in the development of the theoretical framework. Mathias Bavay supported the set-up of Alpine3D.

6 Scale-dependent effects of solar radiation patterns on the snow-dominated hydrologic response

An edited version of this chapter was published by AGU. ©2015. *American Geophysical Union.* All Rights Reserved.

Comola, F., B. Schaefli, P. D. Ronco, G. Botter, M. Bavay, A. Rinaldo, and M. Lehning (2015), Scale-dependent effects of solar radiation patterns on the snow-dominated hydrologic response. Geophys. Res. Lett., 42, 3895–3902, doi: 10.1002/2015GL064075.

To view the published open abstract, go to http://dx.doi.org and enter the DOI.

F. C. developed the theoretical and numerical model, took part in the research design, performed the research, analyzed the data, and contributed to the writing of the paper.

6.1 abstract

Solar radiation is a dominant driver of snowmelt dynamics and streamflow generation in alpine catchments. A better understanding of how solar radiation patterns affect the hydrologic response is needed to assess when calibrated temperature-index models are likely to be spatially-transferable for eco-hydrological applications. We induce different solar radiation patterns in a Swiss Alpine catchment through virtual rotations of the digital elevation model. Streamflow simulations are performed at different spatial scales through a spatially-explicit hydrological model coupled to a physically-based snow model. Results highlight that the effects of solar radiation patterns on the hydrologic response are scale-dependent, i.e. significant at small scales with predominant aspects and weak at larger scales where aspects become uncorrelated and orientation differences average out. Such scale-dependence proves relevant for the spatial transferability of a temperature-index model, whose calibrated degree-day factors are stable to different solar radiation patterns for catchment sizes larger than the aspect correlation scale.

6.2 Introduction

Understanding the hydrologic response of snow-dominated catchments is crucial for water resources management of many dry lowland regions where a large amount of water supply is provided during the snowmelt season [Barnett et al., 2005]. Timing and magnitude of streamflow generation in alpine catchments is strongly related to the spatial and temporal variability of snow depth and ablation [Grünewald et al., 2010], which interact in controlling the spatial pattern of snow water equivalent (SWE). The recent work of Clark et al. [2011] extensively reviewed the dominant processes controlling SWE distribution in alpine catchments, i.e. snow drifting [Schirmer et al., 2011], preferential deposition [Mott and Lehning, 2010], vegetation [Trujillo et al., 2009], melt energy [DeBeer and Pomeroy, 2010], and climate [Trujillo and Molotch, 2014]. Pomeroy et al. [2003] and Ellis et al. [2013] observed that the SWE distribution is significantly influenced by hillsope aspect, which acts as a main control on incoming solar radiation [Garnier and Ohmura, 1968].

The influence of catchment geomorphology has also been widely investigated in relation to rainfall-runoff transformation [Rodríguez-Iturbe and Valdes, 1979, Gupta et al., 1980, Rinaldo et al., 2006]. The structural complexity of the river network, i.e. the heterogeneity of paths available for hydrologic runoff, generates the so-called geomorphologic dispersion [Rinaldo et al., 1991, Rinaldo and Rodriguez-Iturbe, 1996]. This effect sums up to the kinematic dispersion, which stems from the systematic variability of the advective transport processes, becoming asymptotically predominant when the basin scale becomes much larger than the mean hillslope size [Saco and Kumar, 2002, Botter and Rinaldo, 2003]. More recently, signatures of catchment geomorphology were investigated for base flow recession curves [Biswal and Marani, 2010, Mutzner et al., 2013], for streamflow peaks [Rigon et al., 2011] and for nonstationarity in flood frequency [Slater et al., 2015].

The control exerted by a branching river network on the snowmelt-driven hydrologic response of alpine catchments has, however, not been studied so far. The presence of such a network may be particularly effective in connecting different source areas and in averaging out the heterogeneity of snowmelt processes. We therefore investigate whether the spatial distribution of solar radiation, altered artificially by virtual rotations of the Digital Elevation Model (DEM), leaves a detectable hydrologic signature at different spatial scales. We conduct the study by applying a spatially-explicit hydrologic response model coupled to a detailed physical snow model. The relevance of this study is both theoretical, as the link between solar radiation distribution and hydrologic response is still largely unexplored, and practical, as it explains why carefully calibrated temperature-index models [Hock, 2003], in which the aspect is not explicitly accounted for, may be spatially transferable when applied to sufficiently large catchments.

In section 6.3 we introduce the modeling approach and the virtual experiments carried out to investigate the scale-dependent signature of radiation patterns. Section 6.4 describes the case study of the Alpine Dischma catchment (Grisons, Switzerland) and the model setup. Section 6.5 presents the results and discusses the role of solar radiation patterns in relation to different spatial scales.

6.3 Methods

6.3.1 Modeling Approach

Alpine3D is the fully-distributed physically-based model of snow processes developed at the WSL Institute for Snow and Avalanche Research, SLF (Davos, Switzerland). The meteorological data measured by automatic weather stations are spatially interpolated with the MeteoIO library [Bavay and Egger, 2014]to provide the necessary boundary conditions. The near surface processes are modeled based on a DEM and a land use model, whose resolution determines the size of the cells for the surface disctretization. Alpine3D consists of two three-dimensional modules, i.e. the radiation balance model and the snow drift model, and of the one-dimensional module Snowpack [Schmucki et al., 2014], which simulates vertical transport of mass and energy in vegetation, snow and soil for every cell of the grid. All these model components are described in detail in [Lehning et al., 2006]. In particular, the radiation module is based on the so-called view-factor approach, which allows for a physically-based simulation of the radiation balance on steep terrains in combination with spatially-distributed information of surface processes [Helbig et al., 2010]. The snow transport module, introduced by Lehning et al. [2008], simulates the saltation process with the equilibrium saltation model of Doorschot et al. [2004] and the advection-diffusion process with the streamline upwind Petrov-Galerkin technique [Brooks and Hughes, 1982]. The one-dimensional Snowpack model predicts snow development with fine stratigraphic details, solving the heat transport equation and the Richards equation in the vertical direction using a finite element method [Wever et al., 2014]. Snowpack has been extended with a canopy module based on the big leaf concept, which simulates radiative and turbulent heat exchange between the vegetation and the snow/soil surface, evaporation of intercepted water, transpiration and evaporation from the land surface [Musselman et al., 2012, Gouttevin et al., 2015]. The spatially-explicit hydrologic module, described in detail in [Comola et al., 2015] transforms the sequence of snowmelt pulses into streamflow time series at all nodes along the river network. The underlying hydrological processes are described by mass balance equations at subcatchment-scale, i.e. within the catchment portions draining into individual reaches of the network. The model hinges on the stream network delineation provided by the analysis of the DEM and can thus account for arbitrary degrees of geomorphological complexity. The formulation of water transport is based on a travel time framework, accounting for water moisture dynamics and water age mixing processes [Botter et al., 2010]. The mean travel times are assumed to scale with the subcatchment area according to Alexander [1972] and Pilgrim et al. [1982]. Although the full snow transport module is not used for hydrological applications due to the very high resolution and computing capacity required, Alpine3D has been shown to provide reliable snowmelt predictions in numerous studies related to snow hydrology [Bavay et al., 2009, 2013].

6.3.2 Virtual Experiments

The effect of solar radiation patterns on the hydrologic response is analyzed through virtual experiments where the reference DEM of the catchment is rotated maintaining the relative positions of the weather stations. Accordingly, every rotation changes the aspects of the hillslope pixels and thus the pattern of incoming solar radiation, but preserves the spatial distribution of the other meteorological variables, i.e., wind speed and direction, air temperature, soil temperature, longwave radiation, relative humidity and precipitation. This procedure results in different spatial distributions of snowmelt but does not affect the snow accumulation pattern. We rotate the DEM of the study catchment three times by 90° and simulate snowmelt dynamics and streamflow generation in the four resulting configurations. A similar rotation procedure was also adopted by Taesam et al. [2015] to study the directional influence of moving storms on basin response. It is noteworthy that, in real environments, different slope configurations also affect wind and deposition patterns, inducing aspect-dependent differences in vegetation and soil development, with relevant hydrologic implications.

The scale-dependent effect on the hydrologic response is analyzed by simulating the streamflow at selected network nodes that drain progressively larger areas of the catchment. Each of these nodes drains a well-defined catchment having a characteristic size d (m) related to its drainage area A (m^2) according to the relation $d = \sqrt{4A/\pi}$. Accordingly, d is the diameter of the equivalent circular shape of the drained area. Regardless of the proportionality constant, $d \propto \sqrt{A}$ is a scaling expression commonly used to compare the characteristic size of a catchment to the spatial scale of the meteorological forcing. Nicótina et al. [2008] adopted, for instance, a similar approach to study the influence of rainfall spatial correlation on the hydrologic response. Here, we compare the characteristic size d to the correlation scale of the pixel aspects, which represents the distance at which the maximum spatial variability of aspects is sampled. A commonly used tool to estimate the correlation scale of random fields is the variogram [Tate et al., 2001], which can be numerically computed based on DEMs.

6.4 Case Study and Simulation Setup

The Dischma catchment spans 43.3 km^2 and is located in the Swiss Alps. The outlet is located at Dischma Kriegsmatte and the elevation ranges from 1677 to 3130 m. 36% of the land surface is covered by alpine meadows, 34% is rock-covered and the remaining fraction is mainly occupied by forest and bushes; 2% of the catchment area is currently glacier-covered [Zappa et al., 2003]. The absence of large forested areas in the catchment reduces the sources of variability of incoming radiation [Musselman et al., 2013] and establishes a more direct connection between aspect and radiation patterns. In the first Alpine3D study, Lehning et al. [2006] already showed the substantial influence of the topography-controlled solar radiation pattern in the snowmelt of the Dischma catchment.

The aspect maps for the four studied solar radiation distributions, which will be addressed hereafter as configuration A, B, C and D, are given in Figure 6.1a. The geomorphological analysis of the catchment is performed with the Taudem routines [Tarboton, 1997], applied to a 25 m resolution DEM, and delineates a stream network with 55 subcatchments (Figure 6.1b).

An Alpine3D simulation is carried out for the period October 2004 - October 2005, such that a snow-free surface can be prescribed as initial condition. The small glaciated area is initialized by providing ice depth at the corresponding pixels. The study catchment is discretized with squared elements of 100 m side length. The spatial distribution of the meteorological forcings, performed with a Kriging geostatistics interpolation, hinges on the hourly records of 18 high Alpine automatic weather and snow stations (IMIS), deployed in the area by the WSL Institute for Snow and Avalanche Research (SLF) in cooperation with the Swiss mountain cantons. The hydrologic response module runs with the parameter set reported in [Comola et al., 2015], which was calibrated for the year 2012 against the streamflow at the outlet of the Dischma catchment and validated for the year 2013.

The progressively larger catchment portions considered in the analysis of the scale-dependance are shown in Figure 6.1b, together with the corresponding size d. Catchment portions having darker colors are nested within the ones having lighter color, such that the drainage area progressively increases along the selected nodes. Even though streamflow measurements were not available for all the selected sections, the model setup can confidently provide reliable streamflow simulations at the intermediate network nodes owing to the physical description of distributed snow processes and the spatially-explicit setup that accounts for drainage areas in the scaling of the travel times.

6.5 Results and Discussion

Figure 6.1c shows the numerical variogram along with a fitted exponential model for visualization purposes. In the computation of the numerical variogram, the aspect field is treated as isotropic [Cressie and Cassie, 1993]. This procedure provides a simple yet meaningful estimation of the correlation scale.

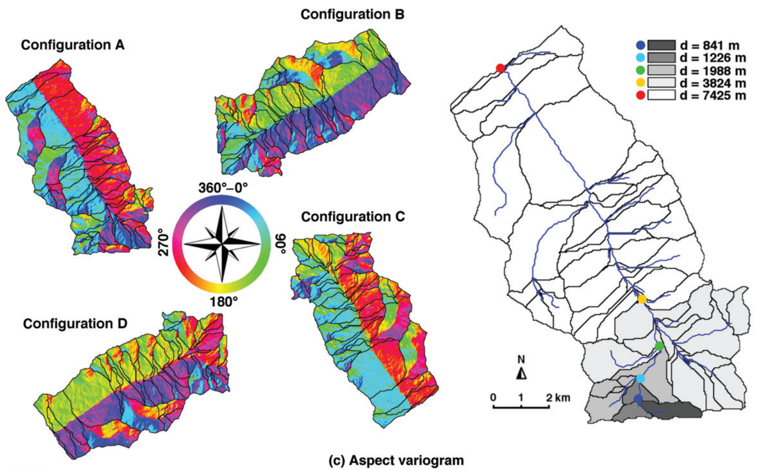

(a) Aspect distributions across the virtual rotations

(b) Increasing catchment size at the selected nodes

(c) Aspect variogram

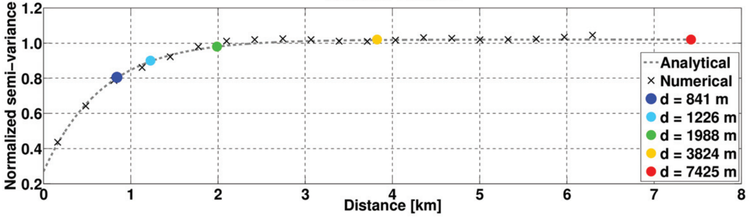

Figure 6.1 – (a) Digital maps of aspects in the original orientation of the catchment and after applying rotations of 90°, 180° and 270°. In the text, we refer to these orientations as configuration A, B, C and D. (b) Series of nested catchment portions, for which the effect of solar radiation patterns is analyzed, and corresponding characteristic size d (see text for details on its computation). (c) Numerical and analytical variograms of aspect spatial field, normalized with respect to the total variance of the aspect field.

Figure 6.1c shows that the variance reaches a threshold at distances of the order of 3 km (A ≃ 7 km^2). The nodes corresponding to the first three catchment portions analyzed lie below this threshold, while the characteristic size of the fourth one is approximately equal to this correlation scale. The variograms computed for other catchments of similar size in the Swiss Alps present similar trends (see Appendix C), suggesting that the de-correlation of aspects at certain scales is a typical feature in Alpine environments. The numerical variogram shown in Figure 6.1c is obtained by applying a random sampling to all pixels. This sampling technique is known to be the source of spurious nugget effects, as visible in Figure 6.1c at short lags, which however does not affect the estimation of the correlation scale [Weng, 2002].

The results in terms of specific streamflow are shown in Figure 6.2, where the signals during the snowmelt phase are given for the different catchment configurations and spatial scales. We observe that, at the smallest scale (Figure 6.2a), the effect of solar radiation distribution is evident during both the two major streamflow events, having their peaks in late May and late June, respectively. As shown in Figure 6.1a, the considered subcatchment is forced to change from east-facing, to north-, west- and south-facing through the three rotations. In May, when snowmelt is only energy-limited, the streamflow increases as a function of the incoming solar radiation. Accordingly, the largest streamflow increase is observed for the east- and south-facing configurations (A and D), showing values up to 50% larger than the north- and west-facing configurations (B and C) at the end of May. In June, instead, snowmelt is partly energy-limited and partly limited by the available snow. The largest streamflow occurs, in fact, for the north- and west-facing configurations (B and C), which receive less energy but have more snow available due to lower melt during the previous event. During this second streamflow event, the maximum difference among the tested configurations occurs at the end of June and is estimated around 30%.

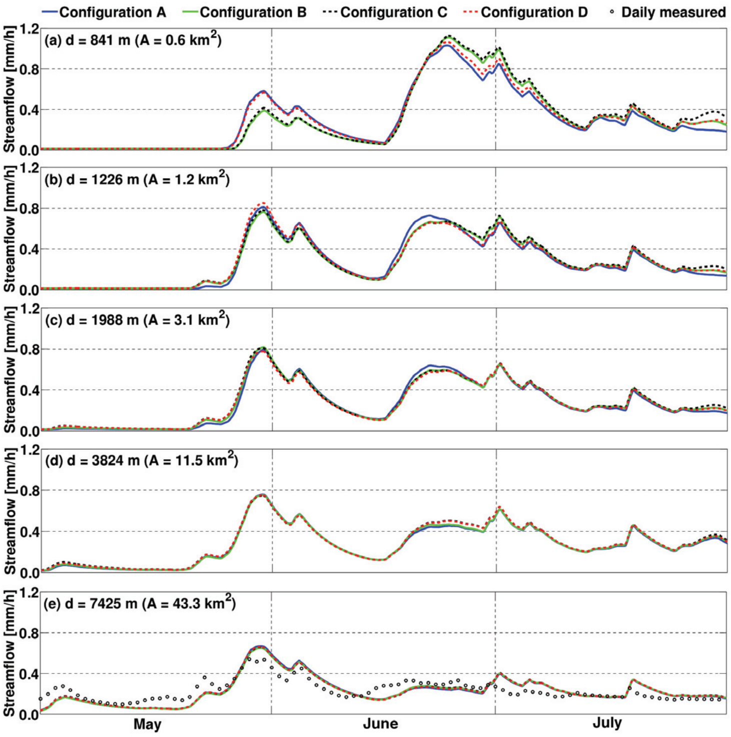

Figure 6.2 – Hydrologic response in the four different configurations and for progressively larger - from (a) to (e) - catchment portions. The results are given in terms of specific streamflow per unit catchment area during the melting season of the year 2005. Signals are averaged over 24 h.

The above analysis illustrates how the interplay of energy- and storage-limitation influences the hydrologic response of a subcatchment with a dominant aspect. At progressively increasing spatial scales, the distribution of the aspect is more heterogeneous, thereby preventing a straightforward interpretation of the results. Nevertheless, Figure 6.2b shows that the hydrologic response is still sensitive to the the spatial distribution of solar radiation up to a scale of around 1.2 km ($A \simeq 1$ km^2), where the combined effects of energy and storage limitation enhances the differences among the configurations. Figure 6.2c shows that at scales of around 2.0 km ($A \simeq 3$ km^2) the differences in the two snowmelt peaks become very small. At scales of around 3.8 km ($A \simeq 11$ km^2) small variations are visible only during the second snowmelt peak (Figure 6.2d) and they completely disappear at larger scales (Figure 6.2e). Here the size of the catchment is such that the spatial variability of aspects is fully sampled in all the tested configurations.

Accordingly, we argue that different spatial patterns of snowmelt resulting from different distributions of solar radiation do not influence catchment-scale streamflows, provided that the drainage area is large enough with respect to the aspect correlation scale. These observations are similar to the results obtained by Nicótina et al. [2008], who analyzed the impact of different rainfall patterns on the hydrologic response at catchment scale. They observed that, for catchments where Hortonian overland flow is negligible, the exact spatial distribution of rainfall is immaterial to the streamflow signal at the outlet, provided that the rainfall spatial average is conserved.

To provide a deeper insight into the observed scale-dependence, we averaged in time the spatially-distributed values of incoming solar radiation, snowmelt and specific streamflow during the peak of the first snowmelt event (25th May - 1st June) and plotted the corresponding coefficient of variation (CV), across the four different configurations (Figure 6.3). The coefficient of variation of SWE is shown and discussed in Appendix C. Significant variations in the solar radiation pattern occur across the ridges of the catchment (Figure 6.3a), where the terrain is steeper and aspects change significantly as a result of the rotations, while almost no differences are observed at the bottom of the valley. Accordingly, a similar pattern is observed for the coefficient of variation of snowmelt (Figure 6.3b). Figure 6.3c suggests that headwater streams generally exhibit a larger coefficient of variation, and therefore a large sensitivity to changes in solar radiation patterns, which is thereafter progressively lost towards the outlet. Figure 6.4a shows the coefficient of variation of specific streamflow at the nodes of the river network versus the catchment size at the corresponding nodes. It is observed that different solar radiation patterns have an influence on the hydrologic response up to a characteristic catchment size of the order of the aspect correlation scale. The reason of the scatter observed for small catchment sizes lies in the slope-dependent aspect variations induced by the DEM rotations. Accordingly, these rotations produce larger streamflow variations in steep subcatchments.

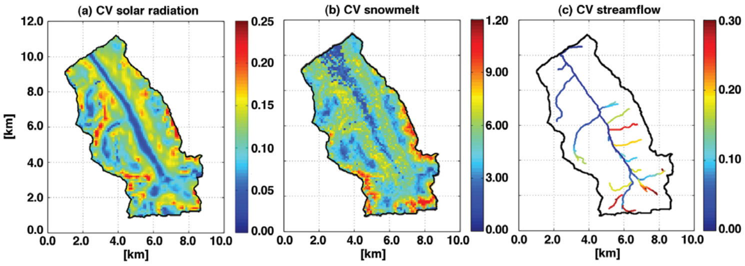

Figure 6.3 – Coefficient of variation, across the four tested configurations, of (a) the incoming solar radiation field, (b) the snowmelt field and (c) the specific streamflow along the network. The values refer to the time averaged values of the first snowmelt peak 25th May - 1st June.

The relevant implications on the spatial transferability of temperature-index models are shown by applying the spatially-explicit model SEHR-ECHO, described in detail in [Schaefli et al., 2014], which simulates the snow processes through a simple degree-day approach. In a first stage, all the 12 parameters of SEHR-ECHO were calibrated to match the streamflow computed by Alpine3D at the catchment outlet during the year 2005. For this calibration, the parameter set that maximizes the Nash-Sutcliffe efficiency is chosen among 35000 randomly generated parameter sets. In a second step, a degree-day factor (DDF) is calibrated for each network node by maximizing the Nash-Sutcliffe efficiency computed on the log-transformed streamflows, in order to reduce the spurious sensitivity to rainfall-driven peak flows. We repeated this second step for all the four configurations A, B, C, D and plotted the corresponding degree-day factors as a function of the catchment size in Figure 6.4b. Results highlight that the calibrated degree-day factors are sensitive to solar radiation distribution at small scales, where points belonging to different configurations are spread out, while they stabilize at catchment sizes of the order of the aspect correlation scale. Previous studies have investigated the sources of variability of the degree-day factors, identifying solar radiation as one of the most relevant [He et al., 2014]. Therefore, we argue that the stabilization of the degree-day factors beyond the aspect correlation scale is strictly related to the scale-dependent effects of the solar radiation patterns on the hydrologic response.

(a) CV streamflow vs. catchment size

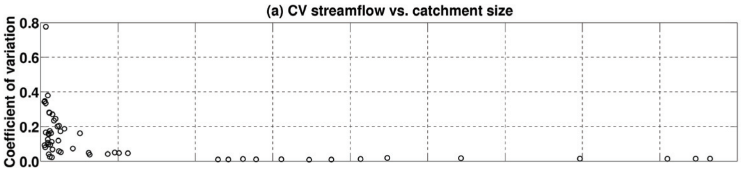

(b) Degree−day factor vs. catchment size

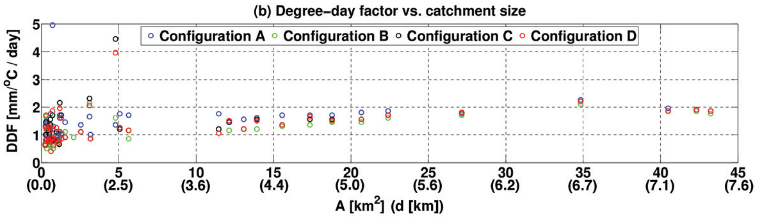

Figure 6.4 – (a) Coefficient of variation of specific streamflow, as provided by Alpine3D at all nodes of the network, and (b) degree-day factors of the spatially-explicit hydrological model SEHR-ECHO [Schaefli et al., 2014], calibrated to match the streamflow computed by Alpine3D, versus the catchment size at the corresponding nodes. The catchment size is given both in terms of drainage area *A* and characteristic size *d* for comparison with the aspect correlation scale. Only the points corresponding to a Nash-Sutcliffe efficiency higher than 0.5 are shown (94% of the total).

6.6 Conclusions

This chapter investigated the role of solar radiation distribution in the hydrologic response of Alpine catchments characterized by progressively larger drainage areas. The study was carried out numerically with a spatially-explicit hydrological model coupled to a physically-based snow model. Different solar radiation distributions were induced by virtual rotation of the catchment DEM. The relative positions of the meteorological stations were preserved in the rotations in order to change the snowmelt pattern without influencing the snow accumulation distribution.

The spatial analysis of the simulated streamflows showed that the signature of solar radiation patterns on the hydrologic response is scale-dependent, i.e. significant when the characteristic size of the catchment is smaller than the correlation scale of the aspects and almost inexistent when the catchment size is larger. Our analysis also suggested that such scale-dependence has an impact on the calibration of temperature-index models, whose degree-day factors might show variability at small scales but stabilize for catchment sizes larger than the correlation scale of aspects. Even though the presence of large forested areas may introduce an additional source of variability for the distribution of incoming solar radiation, and therefore for the degree-day factors, the results suggest that different solar radiation patterns do not impair the spatial transferability of temperature-index models for hydrological simulations of catchments larger than a reference length scale defined by their aspect spatial distribution.

6.7 Acknowledgements

I would like to thank all the co-authors for their help and feedbacks on the published article. The streamflow data were obtained from the Swiss Federal Office for the Environment. The meteorological data was obtained from the IMIS (Interkantonales Mess- und Informationssystem) network, MeteoSwiss and SLF stations.

Conclusions and perspectives

This thesis combined theoretical and numerical models to provide a better understanding of snowfall deposition and drifting snow in alpine terrain (chapters 1 to 4) and hydrologic response of snow-covered catchments (chapters 5 and 6). In the first part of the thesis, we investigated the near-surface flow-particle interactions that affect the snowfall deposition pattern over complex terrain, the fragmentation processes that occur upon impact of wind-blown snow crystals with the surface, the impact-ejection dynamics that drive the splash entrainment of surface snow particles, and the role played by drifting and blowing snow in shaping the snow depth distribution over complex terrain. In the second part of the thesis, we studied the relative importance of advective and non-advective energy fluxes in driving the thermal regime of alpine streams and the influence of the solar radiation pattern on the hydrologic response of snow-covered catchments.

The stochastic approach that we pursued in the development of our theoretical and numerical models allowed us to shed light on the complex snow transport processes that shape the snow depth distribution and on the hydro-thermal response of alpine catchments. Specifically, our studies suggest that the preferential deposition of snowfall can be explained to a great extent by near-surface flow particle interactions, without additional contributions from larger scale processes such as orographic precipitation or seeder-feeder mechanisms. The fragmentation of snow crystals, which has thus far been overlooked in snow saltation models, may then explain the transition from the size distribution of large snowflakes to that of small blowing-snow particles. We further showed that splash entrainment in snow saltation can be predicted based on the energy and momentum conservation laws. In particular, our results suggest that the ejection of cohesive snow is statistically controlled by energy conservation, while the ejection of fresh snow is statistically controlled by momentum conservation. The improved understanding and modeling of snow ejection dynamics proved fundamental for simulations of drifting and blowing snow over complex terrain. We showed that a significant aeolian transport of snow takes place from the windward slopes to the leeward slopes. Accordingly, very different snow depth spatial distributions at hillsope scale may result from the interplay between snowfall deposition and aeolian snow transport. Because of such inhomogeneous pattern of snow depth, the streamflow and stream temperature spatial distributions in alpine catchments present a remarkable variability during the melting season. We also showed that the thermal regime of alpine streams is significantly affected by the advective energy fluxes. Accordingly, reliable simulations of stream temperature dynamics need to properly account for the temperature of subsurface flow infiltrating at the river bed. Finally, our simulations indicated that different patterns of solar radiation do not visibly affect the hydrologic response of snow-covered catchments of size larger than the correlation scale of hillslope aspects, with relevant implications for the spatial transferability of degree-day models for eco-hydrological applications.

Some of the presented results might directly lead to future model developments. We refer in particular to the formulation of splash entrainment based on fundamental conservation laws, which presents a significant improvement over existing parameterizations. Aeolian transport models that solve the Lagrangian trajectories of saltating particles may benefit from the proposed model to provide better quantifications of snow transport not only in alpine terrain, but also in polar regions. It may thus contribute to improve predictions of dust emissions from deserts and snow transport in Antarctica, whose effects reach from global health to weather and climate change. Furthermore, our model can help to find the cause of the intense sand transport activity observed on Mars, where the low density of the atmosphere would rather suggest that winds are not sufficiently strong to erode surface particles.

It is well known that detailed aeolian transport models can only simulate computational domains that are much smaller than the typical size of the atmospheric boundary layer. This limitation, caused by the large scale separation between the typical saltation length (of the order of 1 cm) and the boundary layer height (of the order of 1 km), impairs our understanding of how large turbulent structures interact with the saltation cloud. The proposed ejection function may help the development of reliable sub-grid parameterizations of surface erosion to include in large-scale LES models. This may then allow us to study how saltation affects the coherent turbulent structures that form, under certain conditions, in boundary layer flows, such as hairpin eddies. Moreover, simulations of aeolian transport in the atmospheric boundary layer may shed light on the cause for saltation intermittency, which is normally observed in nature but rarely reproduced by numerical models.

To achieve these challenging goals, however, further experimental work is necessary. On one hand, the parameters of our splash entrainment model could be better constrained through wind tunnel investigations. In particular, quantifications of how snow surface properties, such as restitution coefficient and cohesion, change with air temperature and humidity are scarce. On the other hand, future experimental studies may also improve current formulations of aerodynamic entrainment by focusing, for instance, on the effect of particle shape and cohesion. Advances in these directions would eventually allow us to provide a definitive answer to the question of which, and under which conditions, entrainment mechanism is the most efficient.

Significant advances may also result from including our comprehensive saltation model in a LES code able to simulate thermally driven flows. Katabatic winds are in fact frequent over alpine slopes and Antarctic ice sheets. A deeper insight into the snow erosion driven by the low-level-jet typical of katabatic winds, as well as the flow retardation induced by the inertial particles, would improve the quantifications of snow mass fluxes in conditions of stable atmospheric stratifications.

Some of our results might play an important role for climate change impact studies. In particular, our results on snow fragmentation suggest that frequency and intensity of drifting snow events may be important controls on the reflective properties of snow surfaces, and thus on their energy balance. Furthermore, the proposed travel time distribution model, in combination with Alpine3D, may present a new avenue for predicting the effects of climate change on stream temperature dynamics and related ecological processes.

Overall, the different parts of this thesis added small but decisive contributions to the understanding of how nature works in high alpine environments. This work also opens a range of new research perspectives. In-depth studies of the interplay between flow-particle interactions and large scale processes, namely orographic precipitation and seeder-feeder mechanism, may ultimately provide a more complete view on the processes leading to inhomogeneous snowfall deposition. As for snow fragmentation processes, a better insight into the time and length scales necessary to complete the transition from the snowfall size distribution to the blowing-snow size distribution may indicate whether snow drift models should account for the evolution of particle size distribution for better quantifications of snow mass fluxes. Finally, our results raise new interesting questions on the effects of different snow depth distributions, as resulting from different interactions of snowfall deposition and aeolian transport, on the hydrologic response at different spatial scales. An answer to this question may help assessing at which spatial scale snowfall and snow transport need to be resolved in catchment scale hydrologic models.

A Appendix A

A.1 introduction

This Supplemental Material is organized as follows. In section A.2 we provide a derivation of the statistical-mechanics model of snow saltation accounting for the proposed fragmentation theory. In section A.3, we present the Discrete Element Model (DEM) used to validate the proposed theory of snow crystal fragmentation. In section A.4, we give the detailed list of datasets of blowing-snow size distributions used to validate our model results. Finally, in section A.5, we show the snowfall particle size distribution assumed in our model simulation, together with the particle size distribution of a post snowfall surface obtained by impact and fragmentation of snowfall crystals.

A.2 Residence time distribution model

We can differentiate equation 5 of the main manuscript using Leibniz's rule to obtain the mass balance equation

$$\frac{\mathrm{d}N(D,t)}{\mathrm{d}t} = E(D,t) + F(D,t) - \int_0^t \left[E\left(D,t'\right) + F\left(D,t'\right)\right] p\left(t-t' \mid D\right) \mathrm{d}t'. \tag{A.1}$$

where $p\left(t-t' \mid D\right)$ $\left(\mathrm{s}^{-1}\right)$ is the residence time probability density function. In equation A.1, the integral term is the sum of the mass fluxes depleting the number of crystals of size D in the saltation layer, i.e. the flux of particles to the suspension layer $S(D,t)$ and the impact rate $I(D,t)$. We have therefore

$$S(D,t) + I(D,t) = \int_0^t \left[E\left(D,t'\right) + F\left(D,t'\right)\right] p\left(t-t' \mid D\right) \mathrm{d}t'. \tag{A.2}$$

Let us introduce the partition function $\alpha(D) \in [0;1]$ defining the fraction of crystals of size D that move to the suspension layer. It follows that the remaining fraction $1-\alpha(D)$ stays in saltation and eventually fragments by impacting the surface. We can thus write the residence time as the weighted average of the residence time of particles going to suspension and that of particles impacting the surface, such that

$$p\left(t-t' \mid D\right)=\alpha(D)\, p_S\left(t-t'\right)+[1-\alpha(D)]\, p_I\left(t-t'\right). \tag{A.3}$$

Accordingly,

$$S(D,t)=\alpha(D)\int_0^t \left[E\left(D,t'\right)+F\left(D,t'\right)\right] p_S\left(t-t'\right)\mathrm{d}t', \tag{A.4}$$

$$I(D,t)=[1-\alpha(D)]\int_0^t \left[E\left(D,t'\right)+F\left(D,t'\right)\right] p_I\left(t-t'\right)\mathrm{d}t'. \tag{A.5}$$

If particles move independently from one another, the dynamics are well described by a Poisson process. This yields exponential residence time distributions

$$p_S\left(t-t'\right)=\frac{1}{t_S}\mathrm{e}^{-\dfrac{t-t'}{t_S}}, \tag{A.6}$$

$$p_I\left(t-t'\right)=\frac{1}{t_I}\mathrm{e}^{-\dfrac{t-t'}{t_I}}. \tag{A.7}$$

To our knowledge, the dependency of the mean residence times t_S and t_I on crystal properties and wind speed has never been thoroughly investigated. A reasonable assumption is that the mean time needed to reach the suspension layer equals the mean time needed to impact the surface, i.e., $t_S = t_I$. We can in fact deduce the equivalence of the two time scales from dimensional analysis. On one side, the time needed to reach the suspension layer transported by turbulent motions is approximately equal to the turnover time of an eddy with size equal to the saltation layer height h_0, i.e., $t_S \sim \epsilon^{-2/3} h_0^{1/3}$ [Pope, 2001]. We rely on surface-layer similarity to express the energy dissipation rate at height h_0 as $\epsilon \sim u^{*3}/kh_0$ [Stull, 2012], where k is the Von Karman constant, such that $t_S \sim k^{1/3} h_0/u^*$. On the other side, the time needed to impact the surface is approximately equal to the ballistic time of flight $t_I \sim 2v_r \cos\theta_r/g$, where v_r is the rebound velocity and θ_r is the rebound angle. If we consider typical values of snow saltation, that is, $h_0 = 15$ cm [Gordon et al., 2009, Nishimura and Nemoto, 2005], $u^* = 0.5$ m/s [Pomeroy and Gray, 1990], $v_r = 1$ m/s and $\theta_r = 60°$ [Araoka and Maeno, 1981], we obtain $t_S \sim t_I \sim 10^{-1}$ s. It is worth noting that the precise value of the mean residence times is not relevant to our purpose, as it would affect the time needed to reach a steady state but not the particle size distribution in stationary conditions.

In equations A.4 and A.5, $\alpha(D)$ is assumed equal to the turbulent-diffusivity correction for inertial particles with respect to passive tracers [Csanady, 1963], given that the two quantities obey the same limits and are governed by similar physics. In fact, the probability of becoming suspended is equal to 1 in the limit $D \to 0$, that is, for passive tracers, decreases as the settling velocity becomes relevant compared to turbulent fluctuations, and reaches the lower value 0 in the limit $D \to \infty$. We can then write

$$\alpha(D) = \left[1 + \frac{w_s^2(D)}{\sigma^2}\right]^{-\frac{1}{2}}. \tag{A.8}$$

In equation A.8, $\sigma^2 = 2.5u^{*2}$ [Stull, 2012] is the turbulence velocity variance and $w_s(D)$ is the settling velocity. In our model simulations we assign $u^* = 0.5$ m/s, which is representative of the values reported in the literature (see Table A.1). The settling velocity is calculated as

$$w_s(D) = \sqrt{\frac{2Dg}{3C(\mathrm{Re})}}. \tag{A.9}$$

$g\left(\mathrm{ms}^{-2}\right)$ is the acceleration of gravity and C is the drag coefficient, whose dependence on the particle Reynolds number $\mathrm{Re} = w_s(D)D/\nu$ reads [Clifton and Lehning, 2008]

$$C(\mathrm{Re}) = \frac{24}{\mathrm{Re}} + \frac{6}{1+\sqrt{\mathrm{Re}}} + 0.4. \tag{A.10}$$

Although equation A.10 implies particles of spherical shape, several numerical studies have shown that this formulation is sufficiently accurate for simulations of snow transport in turbulent flows [Clifton and Lehning, 2008, Zwaaftink et al., 2014].

A.3 Discrete element model

We use the DEM software PFC2D v5 [Itasca Consulting Group, 2014], which implements the discrete element method presented in [Cundall and Strack, 1979]. We simulate the fracture of a simplified snowflake structure impacting a rigid surface at given impact velocities v_i and impact angles θ_i. We model the snow crystal geometry to mimic the structure of a real dendritic snowflake, as shown in Figure A.1. The crystal model is formed of three orders of elements, each one presenting a specific size. The elements of order 0 have a diameter of 100 µm, while those of order 1 and 2 have diameters of 50 and 25 µm, respectively. Elements of the same order are bond together to form branches of equivalent order. The six branches of order 0, departing from the center at angular distances of 60°, present a length of 1 mm. Four branches of order 1 depart with angles of 60° from those of order 0. The two internal ones are 350 µm long, while the two external ones are 150 µm long. Two branches of order 2 depart with angles of 60° from each branch of order 1. The more internal ones are 75 µm long, while the more external ones are 50 µm long.

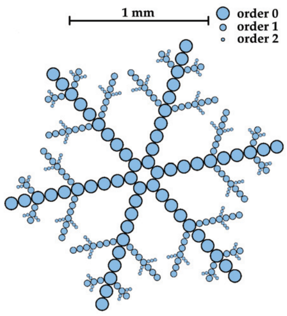

Figure A.1 – Representation of the snow crystal model used in our DEM simulations of fragmentation.

We use as bond contact law the PFC parallel bond model detailed in [Gaume et al., 2015]. A similar DEM model was used to simulate snow granulation and fragmentation processes during avalanche flow [Steinkogler et al., 2015]. We consider the typical mechanical properties of ice [Petrovic, 2003], i.e., elastic modulus $E = 9$ GPa, Poisson's ratio $\nu = 0.3$, friction coefficient $\mu = 0.5$, shear and tensile strengths $\tau_r = 2$ MPa and $\sigma_r = 2$ MPa, and restitution coefficient $e = 0.5$. The surface is also characterized by a friction coefficient μ to mimic the snow surface roughness. The normal force F_n between elements is the sum of a linear elastic and a viscous contribution calculated according to the spring-dashpot model [Akyildiz et al., 1990]. The shear force F_s between elements is linear elastic with a Coulombian friction threshold. The tensile stress σ and shear stress τ in the bonds are calculated via beam theory according to

$$\sigma = -\frac{F_n}{A} + |T| \frac{r_b}{L}, \tag{A.11}$$

$$\tau = -\frac{F_s}{A}, \tag{A.12}$$

where T is the bending moment, r_b is the bond radius (assumed equal to the discrete element radius), $A = \pi r_b^2$ is the bond area, and $L = \pi r_b^4/4$ its moment of inertia. If $\sigma > \sigma_r$, i.e., if the tensile stress exceeds the tensile strength, the bond breaks and both F_n and F_s are set to zero. If $\tau > \tau_r$, i.e., if the shear stress exceeds the shear strength, the bond breaks but the contact forces are not altered, provided that i) the shear force does not exceed the friction limit and ii) the normal force is compressive.

A.4 Datasets of blowing-snow size-distributions

Table A.1 provides information on all known published datasets of blowing-snow size distribution. We only list the measurements used to validate our model results, that is, the ones taken at elevations smaller than the saltation layer height (15 cm [Gordon et al., 2009, Nishimura and Nemoto, 2005]). In addition, Table A.1 lists the turbulence conditions and the measurement technique adopted for the wind tunnel tests performed at the WSL Institute for Snow and Avalanche research, SLF, Davos, Switzerland.

Table A.1 – Datasets of blowing-snow particle size distributions used to validate the model results. SPC indicates snow particle counter, while DC indicates digital camera.

Reference	**Location**	**u^* (m/s)**	**Technique**	**Elevations (cm)**
[Gordon and Taylor, 2009]	Manitoba, CA	0.40	DC	12
[Nishimura and Nemoto, 2005]	Mizuho, AN	0.33	SPC	2, 4, 6, 10, 15
[Nishimura et al., 2014]	Col du Lac Blanc, FR	0.56	SPC	2
[Schmidt, 1980]	Wyoming, US	0.60	SPC	5, 10
SLF wind tunnel	Davos, CH	0.50	SPC	1.0, 1.7, 3.0

A.5 Snowfall and surface particle size-distributions

Figure A.2 presents the two particle size-distributions that we discuss in our model of blowing-snow fragmentation. The black dashed line refers to a typical exponential snowfall size-distribution, as measured in [Gunn and Marshall, 1958] for precipitation intensity of 0.3 mm/h. The grey dashed line refers to a post snowfall surface, whose crystals originate from impact and fragmentation of snowfall crystals. This size distribution is in good agreement with sieve measurements presented in [Granberg, 1985] (red dots in Figure A.2).

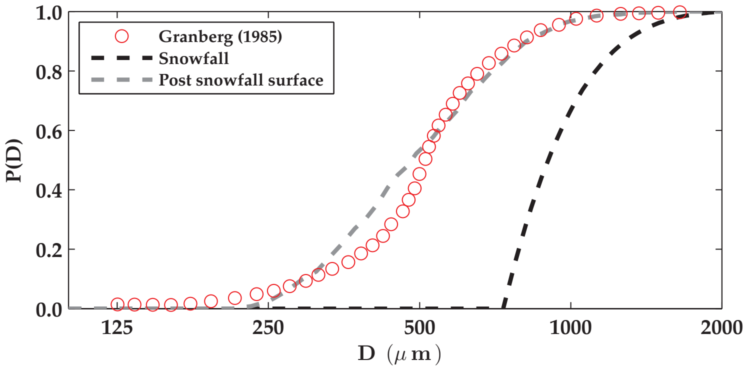

Figure A.2 – Cumulative probability size distribution $P(D)$ of snowfall crystals, as measured for precipitation intensities of ~ 0.3 mm/h [Gunn and Marshall, 1958] (black dashed line), of a post snowfall surface crystals modeled by fragmentation of exponentially-distributed snowflakes (grey dashed line), and of a post blowing-snow surface after settlement of saltating crystals (grey solid line). The red dots refer to a surface particle size distribution measured by sieving analysis [Granberg, 1985].

B Appendix B

B.1 Introduction

The supplemental materials are organized as follows. In section B.2, we provide the detailed derivation of equations 9 and 10. In section B.3, we specify the model setup that we use to simulate the ejection regime of sand and snow. In section B.4, we present a sensitivity analysis with respect to the model parameters. Finally, in section B.5, we describe the Monte Carlo simulations performed to investigate the ejection regime of sand and snow particles.

B.2 Derivation of the model equations

Let us consider the approximated energy and momentum conservation laws (equations 5 and 6)

$$N_E = \frac{\left(1 - P_r \epsilon_r - \epsilon_f\right) m_i v_i^2}{\langle m v^2 \rangle + 2\phi}, \tag{B.1}$$

$$N_M = \frac{\left(1 - P_r \mu_r - \mu_f\right) m_i v_i \cos\alpha_i}{\langle m v \cos\alpha \cos\beta \rangle}. \tag{B.2}$$

The mean values in equations B.1 and B.2 can be expressed as

$$\langle m v^2 \rangle = \langle m \rangle \langle v^2 \rangle + r_E \sigma_m \sigma_{v^2}, \tag{B.3}$$

$$\langle m v \cos\alpha \cos\beta \rangle = \langle m \rangle \langle v \rangle \langle \cos\alpha \rangle \langle \cos\beta \rangle + r_M \sigma_m \sigma_v. \tag{B.4}$$

σ_m, σ_v, and σ_{v^2} denote the standard deviations of m, v, and v^2, respectively. r_E, $r_M \in [-1;1]$ are the correlation coefficients between m and v^2, and between m and v. Since the transformation $v \to v^2$ is non-linear, the values of r_E and r_M may in general be different. Because particles with larger mass are likely to be ejected at lower speed due to their higher inertia, physical measurements of the correlation coefficients yield negative values [Rice et al., 1995]. In equation B.4, we have assumed that α and β are statistically independent, because there is neither a stringent physical reason nor experimental evidence for assuming otherwise.

Further manipulation of equations B.3 and B.4 requires a selection of specific probability distributions for v and m. A large number of numerical results [Anderson and Haff, 1988, 1991] and experimental studies [Mitha et al., 1986, Beladjine et al., 2007] suggest that v is distributed as $v \sim \mathrm{Exp}(\langle v \rangle)$. For such exponential distribution, it can be shown that $\sigma_v = \langle v \rangle$, $\langle v^2 \rangle = 2\langle v \rangle^2$, and $\sigma_{v^2} = 2\sqrt{5}\langle v \rangle^2$.

The probability distribution of m can be derived from that of the ejection diameter d. For fully aggregated sand and snow particles the size distribution is generally assumed lognormal [Kolmogorov, 1941a, Colbeck, 1986], i.e. $d \sim \ln\mathcal{N}(\mu, \sigma)$. μ and σ are the location parameter and the scale parameter, which can be expressed as functions of mean $\langle d \rangle$ and standard deviation σ_d. Assuming spherical grains of density ρ, it can be shown that $m \propto d^3 \sim \ln\mathcal{N}(3\mu, 3\sigma)$, yielding

$$\langle m \rangle = \rho \frac{\pi}{6} \left(\langle d \rangle + \frac{\sigma_d^2}{\langle d \rangle} \right)^3, \tag{B.5}$$

$$\sigma_m = \rho \frac{\pi}{6} \left(\langle d \rangle + \frac{\sigma_d^2}{\langle d \rangle} \right)^3 \sqrt{\left[1 + \left(\frac{\sigma_d^2}{\langle d \rangle} \right)^2 \right]^9 - 1}. \tag{B.6}$$

The derived expressions allow us to account explicitly for the probability distributions of v, m and for their correlation in the calculation of N_E and N_M, which read

$$N_E = \frac{\left(1 - P_r \epsilon_r - \epsilon_f\right) m_i v_i^2}{\frac{2\rho\pi\langle v \rangle^2}{6} \left(\langle d \rangle + \frac{\sigma_d^2}{\langle d \rangle} \right)^3 \left(1 + r_E \sqrt{5 \left[1 + \left(\frac{\sigma_d}{\langle d \rangle} \right)^2 \right]^9 - 5} \right) + 2\phi}, \tag{B.7}$$

$$N_M = \frac{\left(1 - P_r \mu_r - \mu_f\right) m_i v_i \cos\alpha_i}{\frac{\rho\pi\langle v \rangle}{6} \left(\langle d \rangle + \frac{\sigma_d^2}{\langle d \rangle} \right)^3 \left(\langle \cos\alpha \rangle \langle \cos\beta \rangle + r_M \sqrt{\left[1 + \left(\frac{\sigma_d}{\langle d \rangle} \right)^2 \right]^9 - 1} \right)}. \tag{B.8}$$

We then obtain equations 9 and 10 by assuming a spherical impacting grain of density ρ. It is noteworthy that the proposed model formulation bounds r_E and r_M at two critical negative values $r_{E,c}$ and $r_{M,c}$

$$r_{E,c} = -\frac{1}{\sqrt{5\left[1+\left(\frac{\sigma_d}{\langle d\rangle}\right)^2\right]^9-5}}, \tag{B.9}$$

$$r_{M,c} = -\frac{\langle\cos\alpha\rangle\langle\cos\beta\rangle}{\sqrt{\left[1+\left(\frac{\sigma_d}{\langle d\rangle}\right)^2\right]^9-1}}, \tag{B.10}$$

for which $\langle mv^2\rangle$ and $\langle mv\cos\alpha\cos\beta\rangle$ reach the lower boundary zero. This does not limit the ejection analysis for heterogeneous sand described in the manuscript, since the assumed values $r_E = -0.3$ and $r_M = -0.4$ are much larger than the critical values $r_{E,c} = -0.7$ and $r_{M,c} = -1.1$, obtained from equations B.9 and B.10 when $\langle d\rangle = 250$ µm, $\sigma_d = 50$ µm, $\langle\cos\alpha\rangle = 0.97$, and $\langle\cos\beta\rangle = 0.80$ (see section B.3 for more detailed information on the mean ejection angles of sand grains).

B.3 Model setup for sand and snow

Sand. – Numerical studies on sand saltation [Anderson and Haff, 1991, Andreotti, 2004] suggest that the probability of rebound upon impact, conditional to the impact velocity, is

$$\mathrm{P}_r = 0.95\left[1-\exp\left(-k\frac{v_i}{\sqrt{g\langle d\rangle}}\right)\right]. \tag{B.11}$$

where $k \approx 0.1$ for particle sizes typical of saltation on Earth ($\langle d\rangle \approx 250$ µm).

A wide range of experimental and numerical analyses highlight that the fraction of horizontal momentum retained by the rebounding particle is $\mu_r \approx 0.5$ [Rice et al., 1995], and that the fraction of kinetic energy retained by the rebounding particle is $\epsilon_r \approx 0.3$ [Anderson and Haff, 1988, McEwan and Willetts, 1991]. We also assume that the decrease of the restitution coefficient with increasing impact angle [Beladjine et al., 2007, Ammi et al., 2009] can be neglected, given that the range of collision angles in natural saltation is very narrow, around 10° [Shao, 2008]. Experimental investigations suggest that the fraction of impact momentum lost to the bed is $\mu_f \approx 0.4$ [Rice et al., 1995], while the fraction of impact energy dissipated though frictional process is $\epsilon_f \approx 0.96\,(1-\epsilon_r) \approx 0.67$ [Ammi et al., 2009].

Recent theoretical advances highlighted that the mean ejection velocity $\langle v\rangle$ depends on the impact velocity v_i. We therefore adopt the expression [Kok et al., 2012]

$$\frac{\langle v\rangle}{\sqrt{g\langle d\rangle}} = \frac{\mu}{a}\left[1-\exp\left(-a\frac{m_i}{\langle m\rangle}\frac{v_i}{\sqrt{g\langle d\rangle}}\right)\right], \tag{B.12}$$

which agrees well with experimental data [Rice et al., 1995, Willetts and Rice, 1986, 1989] and numerical results [Anderson and Haff, 1991]. In equation B.12, μ is the fraction of impact momentum transferred to the ejected grains, i.e. $\mu = 1 - P_r \mu_r - \mu_f$. Kok and Renno [2009] adopted a value $a = 0.02$ for their simulations of sand saltation on Earth (typical particle size $\langle d \rangle \approx 250$ μm).

Experimental and numerical studies [Rice et al., 1996, Anderson and Haff, 1991, Kok and Renno, 2009] suggest that the probability distribution of the vertical ejection angle is well described by an exponential distribution $\alpha \sim \mathrm{Exp}(\langle \alpha \rangle)$ with a mean ejection angle $\langle \alpha \rangle = 50°$ [Kok et al., 2012], such that $\langle \cos\alpha \rangle = 0.76$. Investigations of the three-dimensional behavior of the ejection process [Ammi et al., 2009, Xing and He, 2013] reveal that the horizontal splash angle follows a normal distribution centered in 0°, i.e., $\beta \sim \mathcal{N}(0, \sigma_\beta)$. For the specific case of sand grains, the standard deviation seems to be $\sigma_\beta = 15°$ [Xing and He, 2013], from which we calculate $\langle \cos\beta \rangle = 0.97$.

Snow. – Several wind-tunnel investigations have improved our understanding of snow particle impact, rebound and ejection [Araoka and Maeno, 1981, Kosugi et al., 1995, Sugiura et al., 1997, Sugiura and Maeno, 2000]. Although the effect of cohesion on the restitution coefficient has not been quantified, $\mu_r \approx 0.5$ and $\epsilon_r \approx 0.3$ were shown to be representative values both for snow and ice grains [Nishimura and Hunt, 2000]. Given that snow and sand saltation dynamics present significant similarities [Nalpanis et al., 1993] and that snow transport models effectively adopt formulations derived for sand [Clifton and Lehning, 2008, Zwaaftink et al., 2014], we investigate the effect of cohesion on snow ejection by relying on the same model set-up used for sand ejection.

B.4 Sensitivity analysis

Here, we analyze the model sensitivity to variations of the input parameters, namely μ_r, μ_f, ϵ_r, ϵ_f, r_E, and r_M. Our purpose is to verify that the ejection model is robust, i.e., that small variations in the input do not produce large variations in the output. It is worth noting that a variation of the coefficient ϵ_r also induces variations of $\epsilon_f = 0.96\,(1 - \epsilon_r)$. Because of this dependence, we study the model sensitivity to ϵ_r and ϵ_f by applying a direct variation only to ϵ_r.

The original values of the model parameters are $\mu_r = 0.5$, $\mu_f = 0.4$, $\epsilon_r = 0.3$, $r_E = -0.3$, and $r_M = -0.4$. We test the model sensitivity by increasing and decreasing each parameter by 20% of the original value. When we test the sensitivity to one parameter, we set the other parameters to the original values. We assign a particle size distribution with $\langle d \rangle = 250$ μm and $\sigma_d = 50$ μm.

Figure B.1 shows that the model presents a relatively larger sensitivity to μ_r and μ_f (panels a and b), in particular when their values are reduced by 20%. According to wind tunnel studies [Rice et al., 1995], however, these parameters present uncertainties smaller than 20%. The sensitivities to the other parameters (panels c to e) are instead relatively small and do not significantly affect the model results.

The performed sensitivity indicates that the model is robust and confirms the conclusions drawn in the manuscript regarding the physics of sand and snow ejection.

B.5 Monte Carlo simulations

We carry out the Monte Carlo simulations to compute the mean ejection number $\langle N \rangle$, i.e., the average number of ejections upon impact of a grain at given velocity v_i. For this purpose, we progressively

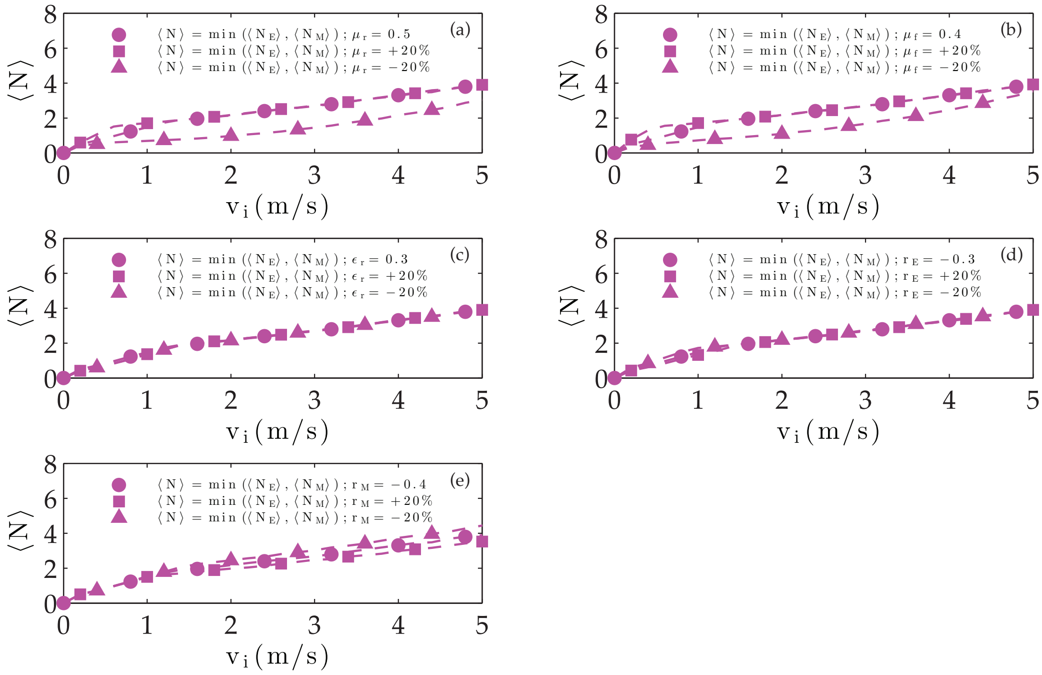

Figure B.1 – Sensitivity analysis of the model response to variations of the parameters by +20% and −20%. (a) Model responses to different values of μ_r, (b) μ_f, (c) ϵ_r, (d), r_E, and (e) r_M.

increase the impact velocity v_i by increments of 0.1 m/s and, for each value, we perform 10^4 ejection simulations as follows. We randomly sample the impact angle α_i within the range [5°;15°]. For uniform sand ejection, the size of the impacting grain is constant, i.e., $d_i = 1$ mm. On the contrary, for heterogeneous sand and snow ejection, we sample the size of the impacting grain from the lognormal distribution of the ejected grains, truncated within 70 and 500 μm, to account for the fact that smaller grains are mostly in suspension and larger ones in reptation [Shao, 2008]. We compute the rebound probability $P_r \in [0;1]$ with equation B.11. We then compute the number of ejections N_E and N_M according to equations 9 and 10, using the value of mean ejection velocity $\langle v \rangle$ obtained from equation B.12. In the computation of equations 9 and 10, we account for the properties of the sediment, i.e., particle size distribution parameters, mass-velocity correlation coefficients, and cohesion. Finally, we average the results of all 10^4 Monte Carlo simulations to compute the mean ejection numbers $\langle N_E \rangle$, $\langle N_M \rangle$, and $\langle N \rangle = \min(\langle N_E \rangle, \langle N_M \rangle)$, specific for the assigned impact velocity.

C Appendix C

C.1 Introduction

In section C.2 we provide additional details on the general trend of aspect variograms in Swiss Alpine environments. Section C.3 presents the analysis of the spatial variability of snow water equivalent (SWE) in the study catchment, as resulting from different solar radiation patterns. On one side, the presented material supports the conclusion that Alpine catchments generally present a well defined correlation scale of aspect distribution and, on the other side, sheds light on some interesting features of SWE variation patterns induced by the interplay of solar radiation and air temperature.

C.2 Aspect Variograms in Alpine Environments

Figure C.1 shows the variograms of pixel aspects computed for three Swiss Alpine catchments, whose location is given in the inset. These variograms present a trend similar to the one of the Dischma catchment, the case study of the article (Figure 1c of the manuscript), and suggest that the de-correlation of aspects is a typical feature of Alpine environments.

The variograms are computed numerically based on the digital elevation models of the catchments (25 m resolution). The aspect field is treated as isotropic, in order to provide a simple yet meaningful estimation of the correlation scale. The computation is carried out applying a random sampling to all pixel aspects. Such random sampling is the source of the spurious nugget effect, visible for short lags, which however does not influence the estimation of the correlation scale.

C.3 SWE Variations Induced by Different Solar Radiation Patterns

This section presents the variations of SWE in the study catchment induced by the different patterns of solar radiation, as resulting by virtual rotations of the reference DEM, in terms of standard deviation (Figure C.2a) and coefficient of variation (Figure C.2b). In a first stage, the distributed values of SWE are time-averaged during the first streamflow event (25th May - 1st June). Afterwards, the standard deviations are calculated pixel-by-pixel across the four tested configurations of the catchment. The coefficients of variation are obtained by dividing the values of standard deviation by the local mean of SWE.

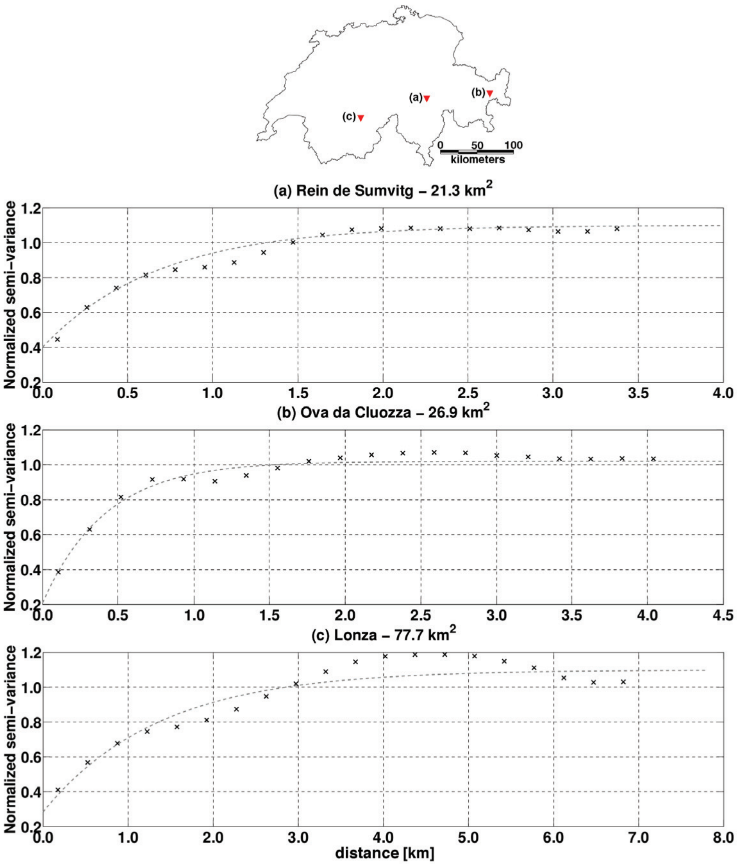

Figure C.1 – Numerical variograms and fitted exponential models computed for (a) the Rein de Sumvitg, (b) the Ova da Cluozza and (c) the Lonza catchment. The catchment locations are shown in the inset. For details on catchments (a) and (b), see [Schaefli et al., 2013], for catchment (c) see [Schaefli et al., 2005].

The results highlight that the pattern of standard deviation is consistent with the variation of solar radiation (Figure 3a of the manuscript), i.e. larger where the terrain is steeper and where the aspects change significantly as a results of the rotations. Moreover, a relatively strong standard deviation is evident for the small glacier in the south-east part of the catchment, which is much more sensitive to changes in incoming solar radiation due to a lower albedo. The pattern of the coefficient of variation, instead, is significantly different due to the strong elevation-dependence of the mean values of SWE. The results suggest that the large standard deviations observed on steep terrains, which are usually at higher elevations, are more than compensated by the large mean values of SWE resulting from the strong snow deposition in cold environments. Accordingly, the largest values of coefficient of variations are observed at mid elevations. This preliminary result needs to be supported by additional investigations, as Alpine3D does not yet account for complex meterological processes leading to preferential snow deposition [Mott and Lehning, 2010]. Moreover, the smoothing of steep slopes due to the surface discretization may lead to localaized overestimations of snow deposition.

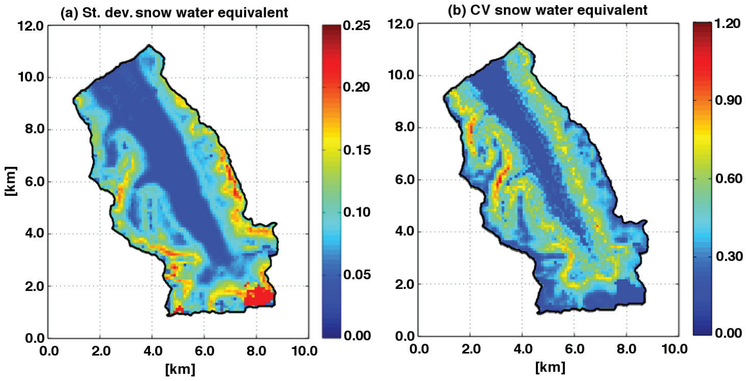
(a) St. dev. snow water equivalent
(b) CV snow water equivalent
12.0
10.0
8.0
6.0
4.0
2.0
0.0
[km]
0.0
2.0
4.0
6.0
8.0
10.0
[km]
0.25
0.20
0.15
0.10
0.05
0.00
1.20
0.90
0.60
0.30
0.00

Figure C.2 – Patterns of (a) standard deviation and (b) coefficient of variation computed for SWE across the four tested catchment configurations.

Bibliography

F. Akyildiz, R. Jones, and K. Walters. On the spring-dashpot representation of linear viscoelastic behaviour. *Rheol. Acta*, 29(5):482–484, 1990.

J. D. Albertson and M. B. Parlange. Surface length scales and shear stress: Implications for land-atmosphere interaction over complex terrain. *Water Resour. Res.*, 35(7):2121–2132, 1999.

G. Alexander. Effect of catchment area on flood magnitude. *J. Hydrol.*, 16(3):225–240, 1972.

M. P. Almeida, E. J. Parteli, J. S. Andrade, and H. J. Herrmann. Giant saltation on Mars. *Proc. Natl. Acad. Sci. U.S.A.*, 105(17):6222–6226, 2008.

M. Ammi, L. Oger, D. Beladjine, and A. Valance. Three-dimensional analysis of the collision process of a bead on a granular packing. *Phys. Rev. E*, 79(2):021305, 2009.

R. Anderson and P. Haff. Wind modification and bed response during saltation of sand in air. In *Aeolian Grain Transport 1*, pages 21–51. Springer, 1991.

R. S. Anderson and K. L. Bunas. Grain size segregation and stratigraphy in aeolian ripples modelled with a cellular automaton. *Nature*, 365:740–743, 1993.

R. S. Anderson and P. K. Haff. Simulation of eolian saltation. *Science*, 241(4867):820–823, 1988.

B. Andreotti. A two-species model of aeolian sand transport. *J. Fluid Mech.*, 510:47–70, 2004.

K. Araoka and N. Maeno. Dynamical behaviors of snow particles in the saltation layer. *Mem. Natl. Inst. Polar Res., Special Issue.*, 19:253–263, 1981.

R. A. Bagnold. *The physics of blown sand and desert dunes.* Methuen, London, 1941.

O. E. Barndorff-Nielsen. Sand, wind and statistics: Some recent investigations. *Acta Mech.*, 64(1-2): 1–18, 1986.

T. Barnett, J. Adam, and D. Lettenmaier. Potential impacts of a warming climate on water availability in snow-dominated regions. *Nature*, 438(7066):303–309, 2005.

M. Bavay and T. Egger. MeteoIO 2.4. 2: a preprocessing library for meteorological data. *Geosci. Model Dev.*, 7(6):3135–3151, 2014.

M. Bavay, M. Lehning, T. Jonas, and H. Löwe. Simulations of future snow cover and discharge in Alpine headwater catchments. *Hydrol. Proc.*, 23(1):95–108, 2009.

M. Bavay, T. Grünewald, and M. Lehning. Response of snow cover and runoff to climate change in high Alpine catchments of Eastern Switzerland. *Adv. Water Resour.*, 55(0):4 – 16, 2013.

D. Bayard, M. Stähli, A. Parriaux, and H. Flühler. The influence of seasonally frozen soil on the snowmelt runoff at two Alpine sites in southern Switzerland. *J. Hydrol.*, 309(1):66–84, 2005.

D. Beladjine, M. Ammi, L. Oger, and A. Valance. Collision process between an incident bead and a three-dimensional granular packing. *Phys. Rev. E*, 75(6):061305, 2007.

P. Benettin, A. Rinaldo, and G. Botter. Kinematics of age mixing in advection-dispersion models. *Water Resour. Res.*, 49(12):8539–8551, 2013a.

P. Benettin, Y. Velde, S. E. Zee, A. Rinaldo, and G. Botter. Chloride circulation in a lowland catchment and the formulation of transport by travel time distributions. *Water Resour. Res.*, 49(8):4619–4632, 2013b.

E. Bertuzzo, M. Thomet, G. Botter, and A. Rinaldo. Catchment-scale herbicides transport: Theory and application. *Adv. Water Resour.*, 52:232–242, 2013.

B. Biswal and M. Marani. Geomorphological origin of recession curves. *Geophys. Res. Lett.*, 37(24), 2010.

G. Botter and A. Rinaldo. Scale effect on geomorphologic and kinematic dispersion. *Water Resour. Res.*, 39(10), 2003.

G. Botter, E. Bertuzzo, A. Bellin, and A. Rinaldo. On the Lagrangian formulations of reactive solute transport in the hydrologic response. *Water Resour. Res.*, 41(4):W04008, 2005.

G. Botter, E. Bertuzzo, and A. Rinaldo. Transport in the hydrologic response: Travel time distributions, soil moisture dynamics, and the old water paradox. *Water Resour. Res.*, 46(3):W03514, 2010.

G. Botter, E. Bertuzzo, and A. Rinaldo. Catchment residence and travel time distributions: The master equation. *Geophys. Res. Lett.*, 38(11), 2011.

E. Bou-Zeid, C. Meneveau, and M. Parlange. A scale-dependent Lagrangian dynamic model for large eddy simulation of complex turbulent flows. *Phys. Fluids*, 17(2):025105, 2005.

A. N. Brooks and T. J. R. Hughes. Streamline upwind/Petrov-Galerkin formulations for convection dominated flows with particular emphasis on the incompressible Navier-Stokes equations. *Comput. Method. Appl. M.*, 32(1):199–259, 1982.

G. Brown. Predicting temperatures of small streams. *Water Resour. Res.*, 5(1):68–75, 1969.

J. H. Brown, V. K. Gupta, B.-L. Li, B. T. Milne, C. Restrepo, and G. B. West. The fractal nature of nature: power laws, ecological complexity and biodiversity. *Phil. Trans. R. Soc. B*, 357(1421):619–626, 2002.

L. Brown and D. Hannah. Alpine stream temperature response to storm events. *J. Hydrometeorol.*, 8(4): 952–967, 2007.

L. Brown, D. Hannah, and A. Milner. Spatial and temporal water column and streambed temperature dynamics within an alpine catchment: implications for benthic communities. *Hydrol. Proc.*, 19(8): 1585–1610, 2005.

W. Brutsaert. *Hydrology: an introduction.* Cambridge University Press, New York, 2005.

D. Caissie. The thermal regime of rivers: a review. *Freshwater Biol.*, 51(8):1389–1406, 2006.

M. V. Carneiro, T. Pähtz, and H. J. Herrmann. Jump at the onset of saltation. *Phys. Rev. Lett.*, 107:098001, 2011.

M. V. Carneiro, N. A. Araújo, T. Pähtz, and H. J. Herrmann. Midair collisions enhance saltation. *Phys. Rev. Lett.*, 111(5):058001, 2013.

S. Chester, C. Meneveau, and M. B. Parlange. Modeling turbulent flow over fractal trees with renormalized numerical simulation. *J. Comput. Phys.*, 225(1):427–448, 2007.

T. Choularton and S. Perry. A model of the orographic enhancement of snowfall by the seeder-feeder mechanism. *Q. J. R. Meteorol. Soc.*, 112(472):335–345, 1986.

V. Chukin, D. Mikhailova, and V. Nikulin. Two methods of determination of ice crystal fractal dimension. *Science Prospects*, 9(36):5–7, 2012.

M. P. Clark, J. Hendrikx, A. G. Slater, D. Kavetski, B. Anderson, N. J. Cullen, T. Kerr, E. Örn Hreinsson, and R. A. Woods. Representing spatial variability of snow water equivalent in hydrologic and land-surface models: A review. *Water Resour. Res.*, 47(7), 2011.

A. Clifton and M. Lehning. Improvement and validation of a snow saltation model using wind tunnel measurements. *Earth Surf. Process. Landf.*, 33(14):2156–2173, 2008.

A. Clifton, J.-D. Rüedi, and M. Lehning. Snow saltation threshold measurements in a drifting-snow wind tunnel. *J. Glaciol.*, 52(179):585–596, 2006.

S. Colbeck. Statistics of coarsening in water-saturated snow. *Acta Metall. Mater.*, 34(3):347–352, 1986.

F. Comola and M. Lehning. Energy- and momentum-conserving model of particle ejection reveals major controls on sand and snow erosion. *Geophys. Res. Lett.*, 44:1—–9, 2017.

F. Comola, B. Schaefli, A. Rinaldo, and M. Lehning. Thermodynamics in the hydrologic response: Travel time formulation and application to alpine catchments. *Water Resour. Res.*, 51(3):1671–1687, 2015.

F. Comola, J. F. Kok, J. Gaume, E. Paterna, and M. Lehning. Fragmentation of wind-blown snow crystals. *Geophys. Res. Lett.*, in review.

C. Coutant. Compilation of temperature preference data. *J. Fish. Res. Board Can.*, 34(5):739–745, 1977.

J. Crassous, D. Beladjine, and A. Valance. Impact of a projectile on a granular medium described by a collision model. *Phys. Rev. Lett.*, 99(24):248001, 2007.

N. A. Cressie and N. A. Cassie. *Statistics for spatial data*, volume 900. Wiley New York, 1993.

G. Csanady. Turbulent diffusion of heavy particles in the atmosphere. *J. Atmos. Sci.*, 20(3):201–208, 1963.

P. A. Cundall and O. D. L. Strack. A discrete numerical model for granular assemblies. *Géotechnique*, 29: 47–65, 1979.

G. Dagan. Transport in heterogeneous porous formations: spatial moments, ergodicity, and effective dispersion. *Water Resour. Res.*, 26(6):1281–1290, 1990.

C. M. DeBeer and J. W. Pomeroy. Simulation of the snowmelt runoff contributing area in a small alpine basin. *Hydrol. Earth Syst. Sc.*, 14(7):1205–1219, 2010.

D. R. DeWalle and A. Rango. *Principles of snow hydrology*. Cambridge University Press, 2008.

R. Dietrich. Impact abrasion of harder by softer materials. *J. Geol.*, 85:242–246, 1977.

P. Diplas, C. L. Dancey, A. O. Celik, M. Valyrakis, K. Greer, and T. Akar. The role of impulse on the initiation of particle movement under turbulent flow conditions. *Science*, 322(5902):717–720, 2008.

P. D'Odorico and R. Rigon. Hillslope and channel contributions to the hydrologic response. *Water Resour. Res.*, 39(5), 2003.

F. Domine, R. Salvatori, L. Legagneux, R. Salzano, M. Fily, and R. Casacchia. Correlation between the specific surface area and the short wave infrared (SWIR) reflectance of snow. *Cold Reg. Sci. Technol.*, 46(1):60–68, 2006.

J. J. Doorschot and M. Lehning. Equilibrium saltation: mass fluxes, aerodynamic entrainment, and dependence on grain properties. *Boundary-Layer Meteorol.*, 104(1):111–130, 2002.

J. J. Doorschot, M. Lehning, and A. Vrouwe. Field measurements of snow-drift threshold and mass fluxes, and related model simulations. *Bound.-Lay. Meteorol.*, 113(3):347–368, 2004.

S. Dupont, G. Bergametti, B. Marticorena, and S. Simoëns. Modeling saltation intermittency. *J. Geophys. Res.*, 118(13):7109–7128, 2013.

C. R. Ellis, J. W. Pomeroy, and T. E. Link. Modeling increases in snowmelt yield and desynchronization resulting from forest gap-thinning treatments in a northern mountain headwater basin. *Water Resour. Res.*, 49(2):936–949, 2013.

D. Finger, G. Heinrich, A. Gobiet, and A. Bauder. Projections of future water resources and their uncertainty in a glacierized catchment in the Swiss Alps and the subsequent effects on hydropower production during the 21st century. *Water Resour. Res.*, 48:W02521, 2012.

D. Finger, A. Hugentobler, M. Huss, A. Voinesco, H. Wernli, D. Fischer, E. Weber, P.-Y. Jeannin, M. Kauzlaric, A. Wirz, et al. Identification of glacial meltwater runoff in a karstic environment and its implication for present and future water availability. *Hydrol. Earth Syst. Sc.*, 17(8):3261–3277, 2013.

M. G. Flanner and C. S. Zender. Linking snowpack microphysics and albedo evolution. *J. Geophys. Res.*, 111(D12), 2006.

H. Gallée, G. Guyomarc'h, and E. Brun. Impact of snow drift on the Antarctic ice sheet surface mass balance: possible sensitivity to snow-surface properties. *Boundary-Layer Meteorol.*, 99(1):1–19, 2001.

B. J. Garnier and A. Ohmura. A method of calculating the direct shortwave radiation income of slopes. *J. Appl. Meteorol.*, 7(5):796–800, 1968.

T. J. Garrett and S. E. Yuter. Observed influence of riming, temperature, and turbulence on the fallspeed of solid precipitation. *Geophys. Res. Lett.*, 41(18):6515–6522, 2014.

P. Gauer. Numerical modeling of blowing and drifting snow in Alpine terrain. *J. Glaciol.*, 47(156):97–110, 2001.

J. Gaume, G. Chambon, N. Eckert, and M. Naaim. Influence of weak-layer heterogeneity on snow slab avalanche release: Application to the evaluation of avalanche release depths. *J. Glaciol.*, 59(215): 423–437, 2013.

J. Gaume, A. Van Herwijnen, G. Chambon, K. Birkeland, and J. Schweizer. Modeling of crack propagation in weak snowpack layers using the discrete element method. *Cryosphere*, 9(5):1915–1932, 2015.

J. Gaume, A. van Herwijnen, G. Chambon, N. Wever, and J. Schweizer. Snow fracture in relation to slab avalanche release: critical state for the onset of crack propagation. *Cryosphere*, 11(1):217–228, 2017.

M. Giometto, A. Christen, C. Meneveau, J. Fang, M. Krafczyk, and M. Parlange. Spatial characteristics of roughness sublayer mean flow and turbulence over a realistic urban surface. *Boundary-Layer Meteorol.*, pages 1–28, 2016.

D. Goossens. Wind tunnel experiments of aeolian dust deposition along ranges of hills. *Earth Surf. Process. Landf.*, 21(3):205–216, 1996.

D. Goossens. Aeolian deposition of dust over hills: the effect of dust grain size on the deposition pattern. *Earth Surf. Process. Landf.*, 31(6):762–776, 2006.

M. Gordon and P. A. Taylor. Measurements of blowing snow, part I: Particle shape, size distribution, velocity, and number flux at Churchill, Manitoba, Canada. *Cold Reg. Sci. Technol.*, 55(1):63–74, 2009.

M. Gordon, S. Savelyev, and P. A. Taylor. Measurements of blowing snow, part II: Mass and number density profiles and saltation height at Franklin Bay, NWT, Canada. *Cold Reg. Sci. Technol.*, 55(1): 75–85, 2009.

I. Gouttevin, M. Lehning, T. Jonas, D. Gustafsson, and M. Mölder. A two-layer canopy model with thermal inertia for an improved snowpack energy balance below needleleaf forest (model SNOWPACK, version 3.2.1, revision 741). *Geosci. Model Dev.*, 8(8):2379–2398, 2015. URL http://www.geosci-model-dev.net/8/2379/2015/.

H. Granberg. Distribution of grain sizes and internal surface area and their role in snow chemistry in a sub-Arctic snow cover. *Ann. Glaciol.*, 7:149–152, 1985.

C. Groot Zwaaftink, H. Löwe, R. Mott, M. Bavay, and M. Lehning. Drifting snow sublimation: A high-resolution 3-d model with temperature and moisture feedbacks. *J. Geophys. Res.*, 116(D16), 2011.

T. Grünewald and M. Lehning. Are flat-field snow depth measurements representative? A comparison of selected index sites with areal snow depth measurements at the small catchment scale. *Hydrol. Proc.*, 29(7):1717–1728, 2015.

T. Grünewald, M. Schirmer, R. Mott, and M. Lehning. Spatial and temporal variability of snow depth and ablation rates in a small mountain catchment. *Cryosphere*, 4(2):215–225, 2010.

M. Guala, C. Manes, A. Clifton, and M. Lehning. On the saltation of fresh snow in a wind tunnel: profile characterization and single particle statistics. *J. Geophys. Res.*, 113(F3), 2008.

K. Gunn and J. Marshall. The distribution with size of aggregate snowflakes. *J. Meteorol.*, 15(5):452–461, 1958.

V. K. Gupta, E. Waymire, and C. Wang. A representation of an instantaneous unit hydrograph from geomorphology. *Water Resour. Res.*, 16(5):855–862, 1980.

R. Hari, D. Livingstone, R. Siber, P. Burkhardt-Holm, and H. Guettinger. Consequences of climatic change for water temperature and brown trout populations in Alpine rivers and streams. *Glob. Change Biol.*, 12(1):10–26, 2006.

Z. H. He, J. Parajka, F. Q. Tian, and G. Blöschl. Estimating degree-day factors from MODIS for snowmelt runoff modeling. *Hydrol. Earth Syst. Sc.*, 18(12):4773–4789, 2014.

N. Helbig, H. Loewe, B. Mayer, and M. Lehning. Explicit validation of a surface shortwave radiation balance model over snow-covered complex terrain. *J. Geophys. Res.*, 115(D18), 2010.

M. Hess, P. Koepke, and I. Schult. Optical properties of aerosols and clouds: The software package OPAC. *Bull. Am. Meteorol. Soc.*, 79(5):831–844, 1998.

A. J. Heymsfield, C. Schmitt, A. Bansemer, and C. H. Twohy. Improved representation of ice particle masses based on observations in natural clouds. *J. Atmos. Sci.*, 67(10):3303–3318, 2010.

T. D. Ho, A. Valance, P. Dupont, and A. Ould El Moctar. Scaling laws in Aeolian sand transport. *Phys. Rev. Lett.*, 106(9):094501, 2011.

R. Hock. Temperature index melt modelling in mountain areas. *J. Hydrol.*, 282(1):104–115, 2003. doi: 10.1016/S0022-1694(03)00257-9.

R. A. Houze. Orographic effects on precipitating clouds. *Rev. Geophys.*, 50(1), 2012.

N. Huang, J. Sang, and K. Han. A numerical simulation of the effects of snow particle shapes on blowing snow development. *J. Geophys. Res.*, 116(D22), 2011.

Itasca Consulting Group. *PFC - Particle Flow Code, Ver. 5.0*, 2014.

J. D. Iversen and B. R. White. Saltation threshold on earth, mars and venus. *Sedimentology*, 29(1): 111–119, 1982.

P. Jaesche, H. Veit, and B. Huwe. Snow cover and soil moisture controls on solifluction in an area of seasonal frost, eastern Alps. *Permafrost Periglacial Process.*, 14(4):399–410, 2003.

C. Kelleher, T. Wagener, M. Gooseff, B. McGlynn, K. McGuire, and L. Marshall. Investigating controls on the thermal sensitivity of Pennsylvania streams. *Hydrol. Proc.*, 26(5):771–785, 2012.

H. Kirchner, G. Michot, H. Narita, and T. Suzuki. Snow as a foam of ice: plasticity, fracture and the brittle-to-ductile transition. *Philos. Mag. A*, 81(9):2161–2181, 2001.

D. Kobayashi. Studies of snow transport in low-level drifting snow. *Contrib. Inst. Low Temp. Sci.*, 24: 1–58, 1972.

J. F. Kok. Difference in the wind speeds required for initiation versus continuation of sand transport on Mars: Implications for dunes and dust storms. *Phys. Rev. Lett.*, 104(7):074502, 2010.

J. F. Kok. A scaling theory for the size distribution of emitted dust aerosols suggests climate models underestimate the size of the global dust cycle. *Proc. Natl. Acad. Sci. U.S.A.*, 108(3):1016–1021, 2011.

J. F. Kok and N. O. Renno. Electrostatics in wind-blown sand. *Phys. Rev. Lett.*, 100(1):014501, 2008.

J. F. Kok and N. O. Renno. A comprehensive numerical model of steady state saltation (COMSALT). *J. Geophys. Res.*, 114(D17), 2009.

J. F. Kok, E. J. Parteli, T. I. Michaels, and D. B. Karam. The physics of wind-blown sand and dust. *Rep. Prog. Phys.*, 75(10):106901, 2012.

A. Kolmogorov. On the logarithmic normal distribution of particle sizes under grinding. In *Dokl. Akad. Nauk SSSR*, volume 31, pages 99–101, 1941a.

A. N. Kolmogorov. The local structure of turbulence in incompressible viscous fluid for very large Reynolds numbers. In *Dokl. Akad. Nauk SSSR*, volume 30, pages 301–305. JSTOR, 1941b.

K. Kosugi, K. Nishimura, and N. Maeno. Studies on the dynamics of saltation in drifting snow. *Rept. Natl. Res. Inst. Earth Sci. Disaster Prevention*, 54:111–154, 1995.

L. Kumar, A. K. Skidmore, and E. Knowles. Modelling topographic variation in solar radiation in a GIS environment. *Int. J. Geogr. Inf. Sci.*, 11(5):475–497, 1997.

M. Kumar, D. Marks, J. Dozier, M. Reba, and A. Winstral. Evaluation of distributed hydrologic impacts of temperature-index and energy-based snow models. *Adv. Water Resour.*, 56:77–89, 2013.

F. Kun and H. J. Herrmann. Transition from damage to fragmentation in collision of solids. *Phys. Rev. E*, 59(3):2623, 1999.

B. Kurylyk, C.-A. Bourque, and K. MacQuarrie. Potential surface temperature and shallow groundwater temperature response to climate change: an example from a small forested catchment in east-central New Brunswick (Canada). *Hydrol. Earth Syst. Sc.*, 17(7):2701–2716, 2013.

J. Leach and R. Moore. Winter stream temperature in the rain-on-snow zone of the Pacific Northwest: influences of hillslope runoff and transient snow cover. *Hydrol. Earth Syst. Sc.*, 18(2):819–838, 2014.

L. Legagneux, A. Cabanes, and F. Dominé. Measurement of the specific surface area of 176 snow samples using methane adsorption at 77 K. *J. Geophys. Res.*, 107(D17), 2002.

M. Lehning and C. Fierz. Assessment of snow transport in avalanche terrain. *Cold Reg. Sci. Technol.*, 51 (2):240–252, 2008.

M. Lehning, P. Bartelt, B. Brown, T. Russi, U. Stöckli, and M. Zimmerli. Snowpack model calculations for avalanche warning based upon a new network of weather and snow stations. *Cold. Reg. Sci. Technol.*, 30(1–3):145 – 157, 1999.

M. Lehning, P. Bartelt, B. Brown, and C. Fierz. A physical SNOWPACK model for the Swiss avalanche warning: Part III: Meteorological forcing, thin layer formation and evaluation. *Cold. Reg. Sci. Technol.*, 35(3):169–184, 2002.

M. Lehning, I. Völksch, D. Gustafsson, T. Nguyen, M. Stähli, and M. Zappa. ALPINE3D: a detailed model of mountain surface processes and its application to snow hydrology. *Hydrol. Proc.*, 20(10): 2111–2128, 2006.

M. Lehning, H. Löwe, M. Ryser, and N. Raderschall. Inhomogeneous precipitation distribution and snow transport in steep terrain. *Water Resour. Res.*, 44(7), 2008.

J. Leinonen and D. Moisseev. What do triple-frequency radar signatures reveal about aggregate snowflakes? *J. Geophys. Res.*, 120(1):229–239, 2015.

J. Lenaerts, M. Den Broeke, W. Berg, E. v. Meijgaard, and P. Kuipers Munneke. A new, high-resolution surface mass balance map of Antarctica (1979–2010) based on regional atmospheric climate modeling. *Geophys. Res. Lett.*, 39(4), 2012.

R. Lieb-Lappen and R. Obbard. The role of blowing snow in the activation of bromine over first-year Antarctic sea ice. *Atmos. Chem. Phys.*, 15(13):7537–7545, 2015.

R. List and R. S. Schemenauer. Free-fall behavior of planar snow crystals, conical graupel and small hail. *J. Atmos. Sci.*, 28(1):110–115, 1971.

E. Loth. Drag of non-spherical solid particles of regular and irregular shape. *Powder Technol.*, 182(3): 342–353, 2008.

C. Luce, B. Staab, M. Kramer, S. Wenger, D. Isaak, and C. McConnell. Sensitivity of summer stream temperatures to climate variability in the Pacific Northwest. *Water Resour. Res.*, 50(4):3428–3443, 2014.

M. MacDonald, J. Pomeroy, and A. Pietroniro. On the importance of sublimation to an alpine snow mass balance in the Canadian Rocky Mountains. *Hydrol. Earth Sys. Sci.*, 14(7):1401–1415, 2010.

R. J. MacDonald, S. Boon, and J. M. Byrne. A process-based stream temperature modelling approach for mountain regions. *J. Hydrol.*, 511:920–931, 2014.

Y. Maday and A. Quarteroni. Spectral and pseudo-spectral approximations of the navier-stokes equations. *SIAM J. Numer. Anal.*, 19(4):761–780, 1982.

J. Magnusson, T. Jonas, and J. Kirchner. Temperature dynamics of a proglacial stream: Identifying dominant energy balance components and inferring spatially integrated hydraulic geometry. *Water Resour. Res.*, 48(6), 2012.

C. Magono. Aerodynamic studies of falling snowflakes. *J. Meteorol. Soc. Japan*, 43:139–147, 1965.

P. J. Mason and D. Thomson. Stochastic backscatter in large-eddy simulations of boundary layers. *J. Fluid Mech.*, 242:51–78, 1992.

C. Matulla, S. Schmutz, A. Melcher, T. Gerersdorfer, and P. Haas. Assessing the impact of a downscaled climate change simulation on the fish fauna in an Inner-Alpine river. *Int. J. Biometeorol.*, 52(2): 127–137, 2007.

J. N. McElwaine, N. Maeno, and K. Sugiura. The splash function for snow from wind-tunnel measurements. *Ann. Glaciol.*, 38(1):71–78, 2004.

I. McEwan and B. Willetts. Numerical model of the saltation cloud. In *Aeolian Grain Transport 1*, pages 53–66. Springer, 1991.

I. K. McEwan and B. B. Willetts. Adaptation of the near-surface wind to the development of sand transport. *J. Fluid Mech.*, 252:99–115, 1993.

C. Meneveau, T. S. Lund, and W. H. Cabot. A Lagrangian dynamic subgrid-scale model of turbulence. *J. Fluid Mech.*, 319:353–385, 1996.

S. Mitha, M. Tran, B. Werner, and P. Haff. The grain-bed impact process in aeolian saltation. *Acta Mech.*, 63(1-4):267–278, 1986.

O. Mohseni and H. Stefan. Stream temperature/air temperature relationship: a physical interpretation. *J. Hydrol.*, 218(3):128–141, 1999.

O. Mohseni, H. Stefan, and J. Eaton. Global warming and potential changes in fish habitat in US streams. *Climatic Change*, 59(3):389–409, 2003.

R. Mott and M. Lehning. Meteorological modeling of very high-resolution wind fields and snow deposition for mountains. *J. Hydrometeorol.*, 11(4):934–949, 2010.

R. Mott, M. Schirmer, M. Bavay, T. Grünewald, and M. Lehning. Understanding snow-transport processes shaping the mountain snow-cover. *Cryosphere*, 4(4):545–559, 2010.

R. Mott, D. Scipion, M. Schneebeli, N. Dawes, A. Berne, and M. Lehning. Orographic effects on snow deposition patterns in mountainous terrain. *J. Geophys. Res.*, 119(3):1419–1439, 2014.

K. N. Musselman, N. P. Molotch, S. A. Margulis, M. Lehning, and D. Gustafsson. Improved snowmelt simulations with a canopy model forced with photo-derived direct beam canopy transmissivity. *Water Resour. Res.*, 48(10), 2012.

K. N. Musselman, S. A. Margulis, and N. P. Molotch. Estimation of solar direct beam transmittance of conifer canopies from airborne LiDAR. *Remote Sens. Environ.*, 136(0):402 – 415, 2013. doi: 10.1016/j.rse.2013.05.021.

R. Mutzner, E. Bertuzzo, P. Tarolli, S. Weijs, L. Nicotina, S. Ceola, N. Tomasic, I. Rodriguez-Iturbe, M. Parlange, and A. Rinaldo. Geomorphic signatures on Brutsaert base flow recession analysis. *Water Resour. Res.*, 49(9):5462–5472, 2013.

U. Nakaya. *Snow crystals: natural and artificial.* Harvard University Press, 1954.

P. Nalpanis, J. Hunt, and C. Barrett. Saltating particles over flat beds. *J. Fluid Mech.*, 251:661–685, 1993.

J. Nash and J. Sutcliffe. *J. Hydrol.*, 10(3):282–290, 1970.

M. Nemoto and K. Nishimura. Numerical simulation of snow saltation and suspension in a turbulent boundary layer. *J. Geophys. Res.*, 109(D18), 2004.

L. Nicótina, E. Alessi Celegon, A. Rinaldo, and M. Marani. On the impact of rainfall patterns on the hydrologic response. *Water Resour. Res.*, 44(12), 2008.

K. Nishimura and J. Hunt. Saltation and incipient suspension above a flat particle bed below a turbulent boundary layer. *J. Fluid Mech.*, 417:77–102, 2000.

K. Nishimura and M. Nemoto. Blowing snow at Mizuho station, Antarctica. *Phil. Trans. R. Soc. A*, 363 (1832):1647–1662, 2005.

K. Nishimura, C. Yokoyama, Y. Ito, M. Nemoto, F. Naaim-Bouvet, H. Bellot, and K. Fujita. Snow particle speeds in drifting snow. *J. Geophys. Res.*, 119(16):9901–9913, 2014.

J. Nittmann and H. E. Stanley. Non-deterministic approach to anisotropic growth patterns with continuously tunable morphology: the fractal properties of some real snowflakes. *J. Phys. A Math. Gen.*, 20(17):L1185, 1987.

L. Oger, M. Ammi, A. Valance, and D. Beladjine. Discrete element method studies of the collision of one rapid sphere on 2D and 3D packings. *Eur. Phys. J. E Soft Matter*, 17(4):467–476, 2005.

A. Ohmura. Physical basis for the temperature-based melt-index method. *J. Appl. Meteorol.*, 40(4): 753–761, 2001.

S. Orlandini and A. Lamberti. Effect of wind on precipitation intercepted by steep mountain slopes. *J. Hydrol. Eng.*, 5(4):346–354, 2000.

S. A. Orszag and Y.-H. Pao. Numerical computation of turbulent shear flows. *Adv. Geophys.*, 18:225–236, 1975.

P. R. Owen. Saltation of uniform grains in air. *J. Fluid Mech.*, 20(02):225–242, 1964.

E. J. Parteli and H. J. Herrmann. Saltation transport on Mars. *Phys. Rev. Lett.*, 98(19):198001, 2007.

R. E. Passarelli and R. C. Srivastava. A new aspect of snowflake aggregation theory. *J. Atmos. Sci.*, 36(3): 484–493, 1979.

E. Paterna, P. Crivelli, and M. Lehning. Decoupling of mass flux and turbulent wind fluctuations in drifting snow. *Geophys. Res. Lett.*, 43(9):4441–4447, 2016.

E. Paterna, P. Crivelli, and M. Lehning. Wind tunnel observations of weak and strong snow saltation dynamics. *J. Geophys. Res.*, in review.

C. Peters-Lidard, M. Zion, and E. Wood. A soil-vegetation-atmosphere transfer scheme for modeling spatially variable water and energy balance processes. *J. Geophys. Res.*, 102(D4):4303–4324, 1997.

J. J. Petrovic. Review Mechanical properties of ice and snow. *J. Mater. Sci*, 38(1):1–6, 2003. ISSN 1573-4803. doi: 10.1023/A:1021134128038. URL http://dx.doi.org/10.1023/A:1021134128038.

D. Pilgrim, I. Cordery, and B. Baron. Effects of catchment size on runoff relationships. *J. Hydrol.*, 58(3): 205–221, 1982.

J. Pomeroy and D. Gray. Saltation of snow. *Water Resour. Res.*, 26(7):1583–1594, 1990.

J. W. Pomeroy, B. Toth, R. J. Granger, N. R. Hedstrom, and R. L. H. Essery. Variation in surface energetics during snowmelt in a Subarctic mountain catchment. *J. Hydrometeorol.*, 4(4):702–719, 2003.

S. B. Pope. *Turbulent flows.* IOP Publishing, 2001.

F. Porté-Agel, C. Meneveau, and M. B. Parlange. A scale-dependent dynamic model for large-eddy simulation: application to a neutral atmospheric boundary layer. *J. Fluid Mech.*, 415:261–284, 2000.

M. Rice, B. Willetts, and I. McEwan. An experimental study of multiple grain-size ejecta produced by collisions of saltating grains with a flat bed. *Sedimentology*, 42(4):695–706, 1995.

M. Rice, B. Willetts, and I. McEwan. Observations of collisions of saltating grains with a granular bed from high-speed cine-film. *Sedimentology*, 43(1):21–31, 1996.

R. Rigon, G. Bertoldi, and T. Over. GEOtop: A distributed hydrological model with coupled water and energy budgets. *J. Hydrometeorol.*, 7(3):371–388, 2006.

R. Rigon, P. D'Odorico, and G. Bertoldi. The geomorphic structure of the runoff peak. *Hydrol. Earth Syst. Sc.*, 15(6):1853–1863, 2011.

A. Rinaldo and A. Marani. Basin scale model of solute transport. *Water Resour. Res.*, 23(11):2107–2118, 1987.

A. Rinaldo and A. Marani, A.and Bellin. On mass response functions. *Water Resour. Res.*, 25(7):1603–1617, 1989.

A. Rinaldo and I. Rodriguez-Iturbe. Geomorphological theory of the hydrological response. *Hydrol. Proc.*, 10(6):803–829, 1996.

A. Rinaldo, A. Marani, and R. Rigon. Geomorphological dispersion. *Water Resour. Res.*, 27(4):513–525, 1991.

A. Rinaldo, G. Botter, E. Bertuzzo, A. Uccelli, T. Settin, and M. Marani. Transport at basin scales: 1. Theoretical framework. *Hydrol. Earth Syst. Sc.*, 10(1):19–29, 2006.

A. Rinaldo, K. Beven, E. Bertuzzo, L. Nicotina, J. Davies, A. Fiori, D. Russo, and G. Botter. Catchment travel time distributions and water flow in soils. *Water Resour. Res.*, 47(7):W07537, 2011.

I. Rodríguez-Iturbe and J. B. Valdes. The geomorphologic structure of hydrologic response. *Water Resour. Res.*, 15(6):1409–1420, 1979.

C. Rolland. Spatial and seasonal variations of air temperature lapse rates in alpine regions. *J. Climate*, 16(7):1032–1046, 2003.

P. M. Saco and P. Kumar. Kinematic dispersion in stream networks 1. Coupling hydraulic and network geometry. *Water Resour. Res.*, 38(11):26–1, 2002.

S. T. Salesky, M. Giometto, M. Chamecki, M. Laehning, and M. B. Parlange. The transport and deposition of heavy particles in complex terrain: an Eulerian model for large eddy simulation. *Water Resour. Res.*, in review.

T. Sato, K. Kosugi, S. Mochizuki, and M. Nemoto. Wind speed dependences of fracture and accumulation of snowflakes on snow surface. *Cold Reg. Sci. Technol.*, 51(2):229–239, 2008.

C. Scarchilli, M. Frezzotti, P. Grigioni, L. De Silvestri, L. Agnoletto, and S. Dolci. Extraordinary blowing snow transport events in East Antarctica. *Clim. Dynam.*, 34(7-8):1195–1206, 2010.

B. Schaefli and H. Gupta. Do Nash values have value? *Hydrol. Proc.*, 21(15):2075–2080, 2007.

B. Schaefli, B. Hingray, M. Niggli, and A. Musy. A conceptual glacio-hydrological model for high mountainous catchments. *Hydrol. Earth Syst. Sc.*, 9(1/2):95–109, 2005. URL http://www.hydrol-earth-syst-sci.net/9/95/2005/.

B. Schaefli, A. Rinaldo, and G. Botter. Analytic probability distributions for snow-dominated streamflow. *Water Resour. Res.*, 49(5):2701–2713, 2013.

B. Schaefli, L. Nicótina, C. Imfeld, P. Da Ronco, E. Bertuzzo, and A. Rinaldo. SEHR-ECHO v1.0: a Spatially Explicit Hydrologic Response model for ecohydrologic applications. *Geosci. Model Dev.*, 7 (6):2733–2746, 2014.

M. Schirmer, V. Wirz, A. Clifton, and M. Lehning. Persistence in intra-annual snow depth distribution: 1. Measurements and topographic control. *Water Resour. Res.*, 47(9), 2011.

D. S. Schmidt, R. Schmidt, and J. Dent. Electrostatic force in blowing snow. *Boundary-Layer Meteorol.*, 93(1):29–45, 1999.

R. Schmidt. Threshold wind-speeds and elastic impact in snow transport. *J. Glaciol.*, 26:453–467, 1980.

R. Schmidt. Properties of blowing snow. *Rev. Geophys.*, 20(1):39–44, 1982a.

R. Schmidt. Vertical profiles of wind speed, snow concentration, and humidity in blowing snow. *Boundary-Layer Meteorol.*, 23(2):223–246, 1982b.

E. Schmucki, C. Marty, C. Fierz, and M. Lehning. Evaluation of modelled snow depth and snow water equivalent at three contrasting sites in Switzerland using SNOWPACK simulations driven by different meteorological data input. *Cold. Reg. Sci. Technol.*, 99:27–37, 2014.

D. Scipión, R. Mott, M. Lehning, M. Schneebeli, and A. Berne. Seasonal small-scale spatial variability in alpine snowfall and snow accumulation. *Water Resour. Res.*, 49(3):1446–1457, 2013.

S. Seeger and M. Weiler. Reevaluation of transit time distributions, mean transit times and their relation to catchment topography. *Hydrol. Earth Syst. Sc.*, 18(12):4751–4771, 2014.

Y. Shao. *Physics and Modelling of Wind Erosion*. Atmospheric and Oceanographic Sciences Library. Springer Netherlands, 2008. ISBN 9781402088957.

Y. Shao and A. Li. Numerical modelling of saltation in the atmospheric surface layer. *Boundary-Layer Meteorol.*, 91(2):199–225, 1999.

Y. Shao and M. Raupach. The overshoot and equilibration of saltation. *J. Geophy. Res. Atmos.*, 97(D18): 20559–20564, 1992.

V. Sharma, M. Parlange, and M. Calaf. Perturbations to the spatial and temporal characteristics of the diurnally-varying atmospheric boundary layer due to an extensive wind farm. *Boundary-Layer Meteorol.*, pages 1–28, 2016.

S. Simoni, S. Padoan, D. Nadeau, M. Diebold, A. Porporato, G. Barrenetxea, F. Ingelrest, M. Vetterli, and M. Parlange. Hydrologic response of an alpine watershed: Application of a meteorological wireless sensor network to understand streamflow generation. *Water Resour. Res.*, 47(10), 2011.

L. J. Slater, M. B. Singer, and J. W. Kirchner. Hydrologic versus geomorphic drivers of trends in flood hazard. *Geophys. Res. Lett.*, 42(2):370–376, 2015. doi: 10.1002/2014GL062482.

R. S. Smith, R. D. Moore, M. Weiler, and G. Jost. Spatial controls on groundwater response dynamics in a snowmelt-dominated montane catchment. *Hydrol. Earth Syst. Sc.*, 18(5):1835–1856, 2014. URL http://www.hydrol-earth-syst-sci.net/18/1835/2014/.

C. G. Sommer, M. Lehning, and R. Mott. Snow in a very steep rock face: Accumulation and redistribution during and after a snowfall event. *Front. Earth Sci.*, 3:73, 2015.

K. Stahl, R. Moore, J. Shea, D. Hutchinson, and A. Cannon. Coupled modelling of glacier and streamflow response to future climate scenarios. *Water Resour. Res.*, 44(2):W02422, 2008.

W. Steinkogler, J. Gaume, L. H, B. Sovilla, and M. Lehning. Granulation of snow: from tumbler experiments to discrete element simulations. *J. Geophys. Res.*, 120(6):1107–1126, 2015.

I. Stewart, D. Cayan, and M. Dettinger. Changes toward earlier streamflow timing across western North America. *J. Climate*, 18(8):1136–1155, 2005.

A. Story, R. Moore, and J. Macdonald. Stream temperatures in two shaded reaches below cutblocks and logging roads: downstream cooling linked to subsurface hydrology. *Can. J. For. Res.*, 33(8):1383–1396, 2003.

F. Stössel, M. Guala, C. Fierz, C. Manes, and M. Lehning. Micrometeorological and morphological observations of surface hoar dynamics on a mountain snow cover. *Water Resour. Res.*, 46(4), 2010.

R. B. Stull. *An introduction to boundary layer meteorology*, volume 13. Springer Science & Business Media, 2012.

G. Sugihara and R. M. May. Applications of fractals in ecology. *Trends Ecol. Evol.*, 5(3):79–86, 1990.

K. Sugiura and N. Maeno. Wind-tunnel measurements of restitution coefficients and ejection number of snow particles in drifting snow: determination of splash functions. *Boundary-Layer Meteorol.*, 95 (1):123–143, 2000.

K. Sugiura, K. Nishimura, and N. Maeno. Velocity and angle distributions of drifting snow particles near the loose snow surface. In *Proceedings of the NIPR Symposium on Polar Meteorology and Glaciology*, pages 108–116. National Institute of Polar Research, 1997.

Swiss Federal Office for Statistic. *Geostat - Version 1997, Swiss spatial land use statistics data-base.* Bern, Switzerland, 2001.

SwissTopo. DHM25- the digital height model of Switzerland, Wabern, 2005.

L. Taesam, S. Juyoung, P. Taewoong, and L. Dongryul. Basin rotation method for analyzing the directional influence of moving storms on basin response. *Stoch. Environ. Res. Risk Assess.*, 29, 2015.

D. Tarboton. A new method for the determination of flow directions and upslope areas in grid digital elevation models. *Water Resour. Res.*, 33(2):309–319, 1997.

N. J. Tate, P. M. Atkinson, et al. *Modelling scale in geographical information science.* John Wiley & Sons Chichester, 2001.

D. Thomson. Criteria for the selection of stochastic models of particle trajectories in turbulent flows. *J. Fluid Mech.*, 180:529–556, 1987.

E. Todini. Hydrological catchment modelling: past, present and future. *Hydrol. Earth Syst. Sc.*, 11(1): 468–482, 2007.

E. Trujillo and N. P. Molotch. Snowpack regimes of the Western United States. *Water Resour. Res.*, 50(7): 5611–5623, 2014.

E. Trujillo, J. A. Ramírez, and K. J. Elder. Scaling properties and spatial organization of snow depth fields in sub-alpine forest and alpine tundra. *Hydrol. Proc.*, 23(11):1575–1590, 2009.

Y.-H. Tseng, C. Meneveau, and M. B. Parlange. Modeling flow around bluff bodies and predicting urban dispersion using large eddy simulation. *Environ. Sci. Technol.*, 40(8):2653–2662, 2006.

L. Verlet. Computer “experiments" on classical fluids. I. thermodynamical properties of Lennard-Jones molecules. *Phys. Rev.*, 159(1):98, 1967.

I. Vinkovic, C. Aguirre, M. Ayrault, and S. Simoëns. Large-eddy simulation of the dispersion of solid particles in a turbulent boundary layer. *Boundary-layer Meteorol.*, 121(2):283–311, 2006.

B. Walter, S. Horender, C. Voegeli, and M. Lehning. Experimental assessment of Owen's second hypothesis on surface shear stress induced by a fluid during sediment saltation. *Geophys. Res. Lett.*, 41(17): 6298–6305, 2014.

J. V. Ward and K. Tockner. Biodiversity: towards a unifying theme for river ecology. *Freshwater Biol.*, 46 (6):807–819, 2001.

J. Weil, P. Sullivan, and C. Moeng. The use of large-eddy simulations in Lagrangian particle dispersion models. *J. Atmos. Sci.*, 61(23):2877–2887, 2004.

J. Weiss. Fracture and fragmentation of ice: a fractal analysis of scale invariance. *Eng. Fract. Mech.*, 68 (17):1975–2012, 2001.

Q. Weng. Quantifying uncertainty of digital elevation models derived from topographic maps. In *Advances in spatial data handling*, pages 403–418. Springer, 2002.

B. Werner. A steady-state model of wind-blown sand transport. *J. Geol.*, pages 1–17, 1990.

B. T. Werner. *A physical model of wind-blown sand transport*. PhD thesis, California Institute of technology, Pasadena, 1987.

N. Wever, C. Fierz, C. Mitterer, H. Hirashima, and M. Lehning. Solving Richards Equation for snow improves snowpack meltwater runoff estimations in detailed multi-layer snowpack model. *Cryosphere*, 8(1):257–274, 2014.

B. Willetts. Aeolian and fluvial grain transport. *Phil. Trans. R. Soc. A*, pages 2497–2514, 1998.

B. Willetts and M. Rice. Inter-saltation collisions. In *Proc. Int. Workshop on Physics of Blown Sand (Aarhus, Denmark)*, volume 1, pages 83–100, 1985.

B. Willetts and M. Rice. Collisions in aeolian saltation. *Acta Mech.*, 63(1-4):255–265, 1986.

B. Willetts and M. Rice. Collisions of quartz grains with a sand bed: the influence of incident angle. *Earth Surf. Process. Landf.*, 14(8):719–730, 1989.

J. D. Wilson. Trajectory models for heavy particles in atmospheric turbulence: comparison with observations. *J. Appl. Meteorol.*, 39(11):1894–1912, 2000.

V. Wirz, M. Schirmer, S. Gruber, and M. Lehning. Spatio-temporal measurements and analysis of snow depth in a rock face. *Cryosphere*, 5(4):893–905, 2011.

W. J. Wiscombe and S. G. Warren. A model for the spectral albedo of snow. I: Pure snow. *J. Atmos. Sci.*, 37(12):2712–2733, 1980.

C. P. Woods, M. T. Stoelinga, and J. D. Locatelli. Size spectra of snow particles measured in wintertime precipitation in the Pacific Northwest. *J. Atmos. Sci.*, 65(1):189–205, 2008.

M. Xing and C. He. 3D ejection behavior of different sized particles in the grain-bed collision process. *Geomorphology*, 187:94–100, 2013.

X. Yang, J. A. Pyle, and R. A. Cox. Sea salt aerosol production and bromine release: Role of snow on sea ice. *Geophys. Res. Lett.*, 35(16), 2008.

G. Zängl. The temperature dependence of small-scale orographic precipitation enhancement. *Q. J. R. Meteorol. Soc.*, 134(634):1167–1181, 2008.

M. Zappa, M. Pos, U. Strasser, P. Warmerdam, and G. L. Seasonal water balance of an Alpine catchment as evaluated by different methods for spatially distributed snowmelt modelling. *Nord. Hydrol.*, 34(3): 179–202, 2003.

C. G. Zwaaftink, M. Diebold, S. Horender, J. Overney, G. Lieberherr, M. Parlange, and M. Lehning. Modelling small-scale drifting snow with a Lagrangian stochastic model based on large-eddy simulations. *Boundary-Layer Meteorol.*, 153(1):117–139, 2014.

Francesco Comola

Personal Data

Place and Date of Birth: Padova, Italy | 18 October 1987.
Address: Ch. de la Roche 20, 1020 Renens, Switzerland.
Phone: +41 76 803 09 56.
email: francesco.comola@gmail.com

Work Experience

Since Dec 2012	Doctoral school in civil and environmental engineering, EPFL, Lausanne, Switzerland. Advisor: Prof. Michael Lehning. (a) Streamflow and stream temperature dynamics in alpine catchment. (b) Erosion and fragmentation of sediments in Aeolian saltation. (c) Large Eddy Simulations of wind-blown sediments over complex terrains.
May - Nov 2012	Trainee at M3E Mathematical Methods and Models for Engineering, Padova, Italy. Coupling of an Efficient Global Optimization algorithm to a Finite Elements geomechanical model to resolve the reservoir uncertainties of the Tengiz oil field, Kazakhstan.
Jun - Aug 2009	Trainee at PROTECNO s.r.l., Padova, Italy. Physical model set-up, experimental testing and data analysis within the MOSE project for the Venetian Lagoon.

Education

Mar 2013	Postgraduate course in Ethics and corporate social responsibility, **Ca' Foscari University**, Venice. Thesis: Plan for a sustainable development of Venice | Advisor: Prof. Gioacchino D'Angelo.
Jul 2012	Master of Science in Civil Engineering. 110/110 *with honors*, **University of Padova**, Italy. Thesis: Damage pattern and progression of breakwater roundheads under multidirectional waves | Advisor: Prof. Piero Ruol.
Nov 2009	Bachelor of Science in Civil Engineering. 110/110 *with honors*, **University of Padova**, Italy. Thesis: Physical model study of wave-induced resonance in offshore structures | Advisor: Prof. Attilio Adami.

Scholarships and grants

Feb - Jul 2011	Erasmus Scholarship for supporting a student exchange at Aalborg University, Denmark. | Advisors: Prof. Thomas Lykke Andersen and Prof. Hans F. Burcharth.
Apr - Jul 2016	Ph.D. mobility scholarship granted by the Doctoral school in Civil and Environmental Engineering of EPFL for supporting a visit to the University of California, Los Angeles. | Advisor: Prof. Jasper Kok.
2015	Grant for production project at the CSCS supercomputing center, Lugano - Switzerland. | Title: Study of land-atmosphere interaction over Antarctic snow-ice formations by large eddy simulation.

Lecturing experience

Teaching assistant	Snow physics and hydrology ENV-525. Physics and chemistry of the atmosphere ENV-320.

First author publications

Published

F. Comola et al., Damage pattern and damage progression on breakwater roundheads under multidirectional waves, *Coastal Engineering*, 83, 24-35, 2014.

F. Comola et al., Thermodynamics in the hydrologic response: Travel time formulation and application to Alpine catchments, *Water Resources Research*, 51 (3), 1671-1687, 2015.

F. Comola et al., Scale-dependent effects of solar radiation patterns on the snow-dominated hydrologic response, *Geophysical Research Letters*, 42 (10), 3895-3902, 2015.

F. Comola et al., Efficient global optimization of reservoir geomechanical parameters based on synthetic aperture radar-derived ground displacements, *Geophysics*, 81 (3), M23-M33, 2016.

F. Comola and M. Lehning, Energy- and momentum-conserving model of splash entrainment in sand and snow saltation, *Geophysical Research Letters*, 44.

Under review

F. Comola et al., Fragmentation of wind-blown snow crystals, *Geophysical Research Letters*.

Conference presentations and invited seminars

Conferences

European Geosciences Union Meeting, Vienna, 2013 and 2014.
American Geophysical Union Meeting, San Francisco, 2014 and 2015.
International Union of Geodesy and Geophysics, Prague, 2015.
American Physical Society - Division of Fluid Dynamics, Boston, 2015.
American Meteorological Society - Boundary Layers and Turbulence, Salt Lake City, 2016
Davos Atmosphere and Cryosphere Assembly, Davos, 2013.
Swiss Geoscience Meeting, Fribourg, 2014.

Seminars

Lanzhou University, Lanzhou, Cina.
Title: 3-D simulations of snow transport, erosion and deposition using Large Eddy Simulation coupled with a Lagrangian Stochastic Model.
Chaired by Prof. Huang Ning

Princeton University, Princeton, New Jersey.
Title: Physics and modelling of wind-blown sand and snow.
Chaired by Prof. Elie Bou-Zeid

École Polytechnique Fédérale de Lausanne, Switzerland.
Title: Physics and modelling of wind-blown sand and snow.
Chaired by Prof. Micheal Lehning

Languages

Italian	Mothertongue.
English	Professional working proficiency.
French	Fluent.
German, Chinese	Basic knowledge.

Skills

C++, Fortran, Shell, MATLAB, Office, LaTeX, Python, Paraview, AutoCAD, ArcGIS.